INAUGURAL-DISSERTATION

zur

Erlangung der Doktorwürde

der

Naturwissenschaftlich-Mathematischen Gesamtfakultät

der

Ruprecht-Karls-Universität

Heidelberg

vorgelegt von

M.Sc. **Ilaria Marchetti**

aus Pisa, Italien

Tag der mündlichen Prüfung:

19. April, 2013

CHARACTERISATION OF WATER PENETRATION INTO POLYCRYSTALLINE UO_2

Gutachter:

Prof. Dr. **Thomas Fanghänel**
Prof. Dr. **Petra Panak**

CHARACTERISATION OF WATER PENETRATION INTO POLYCRYSTALLINE UO_2

Keywords: Uranium dioxide, SIMFUEL, secondary ion mass spectrometry, depth profile, corrosion, leaching, chemical diffusion, grain boundary diffusion, lattice diffusion, oxygen diffusion, geological disposal, spent fuel

In the event of exposure of spent nuclear fuel to groundwater in a final repository, the preferential dissolution of grain boundaries rather than matrix dissolution would cause a rapid increase of the surface area exposed to groundwater, with effects on the mobilisation of radionuclides and on the overall mechanical stability of the spent fuel pellet. In this respect, a research project has been launched at the Institute for Transuranium Elements (ITU, Karlsruhe, Germany), with the goal of gaining understanding of the mechanisms of the penetration of water into polycrystalline UO_2 under conditions relevant for final disposal in a geological repository.

As a first approach to this issue, the study has been initially focused on natural UO_2 with well defined grain size and morphology. The experiments have then been extended to SIMFUEL, an inactive analogue of UO_2 fuel containing elements simulating a spent fuel, to assess potential effects associated to the presence of fission products. The experiments consisted of static leaching tests on UO_2 fuel pellets using ^{18}O-labelled water. Unlike most of the diffusion studies on UO_2, the experiments in this study were conducted at low temperature (≈ 25°C and 60°C), in order to reproduce the temperature range expected in the geological disposal scenario temperatures. To ensure sufficient contact time between the solid phase and the solution for penetration to be detectable experiments lasted 3-9 months. Experiments were carried out initially in oxidising conditions (in air or in N_2 glovebox) and thereafter under 10 bar H_2 atmosphere, in order to approach conditions more similar to the anoxic and reducing environment expected in the final repository. Pre- and post-corrosion surface characterisation was performed by means of scanning electron microscopy (SEM), atomic force microscopy (AFM) and X-ray photoelectron spectrometry (XPS), while solution analysis was performed by inductively coupled plasma mass spectrometry (ICP-MS). The penetration of water was assessed by depth profiling of the tracer ^{18}O using Secondary Ion Mass Spectrometry (SIMS) microscopy. Well-known analytical models were used to fit of the profiles and determine the relevant diffusion coefficients.

For the first time in this study, the chemical diffusion coefficient of oxygen in different UO_{2+x} phases was experimentally determined at temperatures below 100°C. The good agreement with extrapolated literature data obtained from high-temperature diffusion experiments verifies the viability of the SIMS depth profiling method for the determination of diffusion coefficients, even with a diffusion length of tens of nm. The study has also reported for the first time evidence of the presence of oxygen/water grain-boundary diffusivity in polycrystalline UO_2 and an estimate of the diffusion coefficient at 25°C is here presented. The study has also shown that the possibility to observe grain boundary diffusion by SIMS depth profiling might depend to a large degree on the grade of surface oxidation of UO_2. In general, all these experimental findings have given an important starting point for the study of water penetration in the spent fuel.

Charakterisierung der Penetration von Wassermolekülen in polykristallines UO_2

Stichwörter: Urandioxid; SIMFUEL; Sekundärionen-Massenspektrometrie; Tiefenprofil; Korrosion; Auslaugen; chemische Diffusion; Korngrenzendiffusion; Kristallgitter Diffusion; Sauerstoff-Diffusion; Endlagerung; abgebrannte Brennelemente

Falls abgebrannter Kernbrennstoff bei der Endlagerung in Kontakt mit Grundwasser kommen würde, würde die bevorzugte Auflösung des Materials an Korngrenzen, und weniger die Auflösung der Matrix selbst, zu einem schnellen Anstieg der Expositionsfläche führen. Dies hätte einen Einfluss auf die Mobilisierung von Radionukliden, und auf die mechanische Stabilität der bestrahlten Kernstofftabletten insgesamt. Unter diesem Gesichtspunkt wurde am Institut für Transurane (ITU, Karlsruhe, Deutschland) eine Studie ins Leben gerufen, mit dem Ziel, die Mechanismen des Eindringens von Wassermolekülen in polykristallines UO_2 unter Endlager-relevanten Bedingungen zu untersuchen.

Als erste Herangehensweise an diese Problematik wurde ursprünglich das Hauptaugenmerk auf natürliches UO_2 mit einer gut definierten Korngröße und Morphologie gelegt. Um mögliche Effekte, die durch die Anwesenheit von Spaltprodukten entstehen könnten, zu untersuchen, wurden die Experimente auf SIMFUEL, eine inaktive Variante von UO_2, die zusätzliche Elemente erhält, die abgebrannte Kernbrennstoffe simulieren, ausgeweitet. Diese Experimente bestanden aus statischen Auslaugtests von UO_2-Brennstofftabletten mit ^{18}O-markiertem Wasser. Anders als die meisten Diffusionsstudien an UO_2 wurde eine niedrige Temperatur (~25°C und 60°C) während der aktuellen Versuche verwendet, um den Temperaturbereich abzudecken, der in einem geologischen Endlager zu erwarten ist. Die Experimente dauerten zwischen 3 und 9 Monate, um eine ausreichende Kontaktzeit zwischen der Festphase und der Lösung für eine messbare Eindringung zu gewährleisten. Anfangs wurden die Versuche unter oxidierenden Bedingungen (unter Luft oder in einem N_2-Handschuhkasten) durchgeführt. Anschließend wurde zu H_2-Atmosphäre (10 bar) gewechselt, um sich jenen anoxischen und reduzierenden Bedingungen anzunähern, wie sie in einem Endlager zu erwarten sind. Die Oberflächen wurden vor und nach den Auslaugtests mittels Rasterelektronenmikroskopie, Rasterkraftmikroskopie, sowie der Röntgenphotoelektronen-spektrometrie charakterisiert, während Lösungen mit der induktiv gekoppelten Plasma-Massenspektrometrie (ICP-MS) analysiert wurden. Die Erstellung eines ^{18}O-Tiefenprofils mittels Sekundärionenmassenspektrometrie (SIMS) erlaubte die Bestimmung der Eindringtiefe des Wassers. Für das Angleichen der Profile und die Bestimmung der relevanten Diffusionskoeffizienten kamen namhafte analytische Modelle zum Einsatz.

Im Rahmen dieser Studie konnte zum ersten Mal der chemische Diffusionskoeffizient von Sauerstoffatomen in verschiedenen UO_{2+x}-Phasen bei Temperaturen unter 100°C experimentell bestimmt werden. Die gute Übereinstimmung der Ergebnisse mit extrapolierten Literaturdaten aus Hochtemperatur-Diffusionsexperimenten zeigt, dass die Erstellung von Tiefenprofilen mittels SIMS für die Bestimmung von Diffusionskoeffizienten geeignet ist, selbst wenn nur geringe Eindringtiefen von wenigen 10 nm vorliegen. Auch konnte erstmalig gezeigt werden, dass in polykristallinem UO_2 eine Diffusion von Sauerstoff/Wasser an Korngrenzen stattfindet. Der Diffusionskoeffizient bei 25°C wurde ermittelt. Die Studie zeigt außerdem, dass die Möglichkeit, Korngrenzendiffusion mittels der Erstellung von SIMS-Tiefenprofilen festzustellen, zum großen Teil vom Oxidationsgrad des UO_2 abhängt. Insgesamt bilden die Ergebnisse dieser Studie einen wichtigen Ausgangspunkt für weitere Studien zur Penetration von Wassermolekülen in abgebrannten Brennelementen.

Acknowledgements

First and foremost I wish to express my deepest gratitude to Prof. Dr. Thomas Fanghänel for accepting the scientific guidance of my doctoral thesis. I am deeply grateful for the trust that was put in me, for the amazing opportunity that I was given and for all the support and help that I received during these years.

I would like to thank Dr. Paul Carbol and Dr. Fabio Belloni who have shared the direct supervision of my work at ITU, for their relentless support. Thank you for the many interesting discussions, for the help in and outside the laboratory, but above all thank you for your patience and kindness and for believing in me.

I gratefully acknowledge the European Commission for funding my research fellowship at the Institute for Transuranium Elements (Karlsruhe, Germany) and I am especially grateful to Dr. Jean-Paul Glatz, Head of the Nuclear Chemistry Unit, for the faith in my work and the many chances he contributed to offer me. I wish to express my gratitude also to Dr. Thomas Gouder and Dr. Gunnar Buckau for helping me put my work in the wider perspective of Nuclear Waste Disposal and to Dr. Birgit Christiansen, coordinator of the Research Fellows at ITU, for her encouragement.

The original ideas for this research project came from Dr. Virginia Oversby, whom I gratefully acknowledge. I also wish to thank Prof. Kastriot Spahiu and Dr. Lena Zetterström Evins from the Swedish Nuclear Fuel and Waste Management Co. (SKB) for their interest in my work.

I would not have managed to carry out this study had it not been for the contribution of many colleagues and collaborators. I would like to thank especially Dr. Jérôme Paillier for the generous assistance and the lengthy discussions and Jérôme Himbert for the infallible experimental support and for sharing with me the many challenges and satisfactions of the SIMS laboratory. I would like to acknowledge Dr. Philipp Pöml and Dr. Clive Walker for the kind support in revising my publications. To Dr. Thierry Wiss and Helmut Thiele I am extremely grateful for the SEM-EDX analysis and to Markus Ernstberger for the aid in the sample preparation. For the ICP-MS analysis, I thank especially Dr. Laura Aldave de las Heras and Miguel Sandow, Stefaan Van Winckel and Mariangela Cardinale. I gratefully acknowledge Dr. Rachel Eloirdi for the XRD analysis; Elke Bonhert and Dr. Frank Heberling at the Institute for Nuclear Waste (KIT-INE) for the AFM characterisation and Dr. Alice Seibert for the XPS analysis and for many interesting discussions. For the kind assistance in the use and maintenance of the SIMS and for always being available to help me, I would like to express my deepest gratitude to Magnus Hedberg and Rachid Hasnaoui. I wish to thank Dr. Detlef Wegen, Dr. Michael Krachler and Dr. Maria Wallenius for the many interesting suggestions. My special thanks also go to Dr. Vincenzo Rondinella for always finding time to discuss my results and my doubts, but also so much more.

For making my daily life a good deal more fun and easier during these years, I should thank many other people as well, at ITU and outside. Among them: Irmi, Rikard, Matthias, Raphael, Rosa, Carmen, Helena, Zeynep, Steffi, Mike, Ondrej, Björn, Patric and Remi. I thank then Nicole and Neli for always listening to me and for being my friends far longer than they have been my colleagues. To Donata and Jouni, my neighbours, I can only offer my eternal gratitude for offering me so much help, cat-sitting and nice evenings together.

Finally, I would like to thank my family that, even from far away, has always supported me with love and well-wishing, but above all for having given me the chance to embark in this wonderfully scary journey across Europe. And for accompanying me in this, for enduring my fear and my despair as well as for sharing my successes and satisfactions, for being my soul mate and my best friend, my last grateful thought goes to my husband, Daniel.

TABLE OF CONTENTS

1 Introduction

"The Italian navigator has landed in the New World". With this evocatively encoded message, on December 2nd 1942, the U.S. National Defence Research Committee received information about the accomplishment of the first controlled nuclear fission chain reaction, carried out by the group of scientists guided by Enrico Fermi. That day the Atomic Age began, leading to the creation of the atomic bomb and nuclear power plants: two of the most powerful and most controversial achievements of the twentieth century. Furthermore, that day, also the first "radioactive waste" ever was produced by mankind.

Nevertheless, nuclear power is the first human technology which, from its start, considered the issue of waste disposal as a development parameter. A first international consensus on radioactive waste disposal was reached already in 1955, a decade before fission energy became a practical proposition, at the conference arranged by the United Nations on the peaceful uses of atomic energy. It was then concluded, at the session on radioactive by-products of uranium fission, that the concept of "dilution and dispersal" then in use, had to be systematically substituted by the concept of "concentrate and confine". Even though, at first, disposal of the waste was not considered as urgent as the need to confine the handling steps - from uranium fission to the separation of radioactive waste from the spent fuel - it was no later than 1965 that a first guidebook on underground disposal was published, by the International Atomic Energy Agency.

However, the safety of nuclear waste disposal is possibly the most repeated argument against nuclear energy in the world. After the fast growth of the atomic energy business during the oil crisis of the seventies, a general movement against nuclear power has arisen and grown since the eighties, insisting principally on the need to assess the risks for the public and therefore to ensure that the spent nuclear fuel remains isolated from the biosphere for a sufficiently long time scale.

The average annual global disposal rate for all waste classes combined is approximately 2.8 million m^3 per year, primarily low level or very low level waste, managed in a variety of storage and disposal facilities [1]. While storage and disposal of low level radioactive waste is a well established practice worldwide, disposal of spent nuclear fuel and high level waste remains to be implemented.

There are two main management strategies for spent nuclear fuel. One consists in reprocessing the fuel so to recover the uranium and plutonium content and recycle it to produce new fuel (so-called mixed oxide fuel, MOX). Today reprocessing plants are in operation in France, India, Russian Federation and in the United Kingdom [1]. The waste from reprocessing is solidified and disposed of for a length of time until it can be considered to have radio-toxicity comparable to natural uranium, from which the fuel has originated. The second strategy is the so-called “once through concept”, that means that the spent fuel is not recycled. Instead the waste is to be stored in a final deep repository after ≈ 30-40 years of initial cooling in a temporary storage. In the once through cycle, uranium and plutonium are less efficiently used but the

complications associated with reprocessing, e.g. radioactive fuel, complicated processes due to high active material, are avoided.

The total amount of spent fuel that has been discharged globally is approximately 320 000 tonnes of heavy metal (t HM). Of this amount, about 95 000 t HM have already been reprocessed, and about 225 000 t HM are stored in spent fuel storage pools at reactors or in away-from-reactor storage facilities. Total global reprocessing capacity is about 5000 t HM per year [2].

Geological disposal is internationally recognized as the best option for the final management of high-level and long-lived radioactive waste [3], but no repository has yet been implemented. Licensing of geological disposal represents itself a unique challenge intimately connected with the lack of public acceptance, although some European countries like France, Sweden and Finland are well advanced in the process. The need to provide safety demonstrations over a very large time scales ($>10^5$ years) is still the major scientific challenge: overall knowledge of all the physical and chemical processes involved and of the parameters necessary to describe them is needed. Also the uncertainties associated with such evaluations must be clear in order to obtain reliable models.

Besides, scenarios like earthquakes or ice-age or shifts of rocks should be taken into account, as they could result in accidental exposure of fuel to groundwater. The potential dissolution of the fuel and the resulting migration of radio-nuclides in the biosphere need to be assessed.

This is the frame in which the work here presented took place. The aim has been to model the mechanisms of water penetration in UO_2, as a first step towards the study of spent fuel. Different experimental parameters were considered in order to isolate the different agents that might be playing a role in this complex physico-chemical process, keeping however in sight what might be expected as typical deep repository conditions. The results will hopefully improve the safety assessment of spent fuel repositories.

2 Background

2.1 Nuclear Fuel Cycle

A nuclear reactor is a system in which the fission of a fissile atom by means of neutrons takes place like a chain reaction: the heavy nucleus splits into two or more lighter nuclei, releasing kinetic energy, gamma radiation and free neutrons, that may later be absorbed by other fissile atoms and trigger further fission events, which on their turn will release more neutrons, and so on. The heat produced by the fission is then used to produce steam to drive turbines, like in any other thermal power plant.

Fissile nuclei, like ^{235}U, ^{239}Pu, and ^{241}Pu, have a high cross-section for thermal neutrons, *i.e.* neutrons with a kinetic energy of about 0.025 eV. Fertile nuclei, like ^{238}U or ^{232}Th, have a higher cross-section for neutron capture, through which, typically after β-decay, they can be converted into a fissile nucleus. The use of a moderator is necessary to slow down or "thermalise" the neutrons produced, in order to increase the fission cross-section and sustain the chain reaction.

The most common commercial reactors are the so-called light water reactors that use water both as a moderator and as a coolant, *i.e.* to absorb the heat generated by the fission. Nowadays the standard reactor design is the pressurised water reactor (PWR), which employs a cooling system that is physically separated from the water that will be boiled to produce pressurised steam for the turbines. Another very common design instead is the boiling water reactor (BWR) in which the water for the steam turbines is boiled directly by the reactor core. The fuel used by these reactor types, which together account for almost 90% of the operating ones is uranium enriched up to typically 3.5-5 at.% ^{235}U.

Not all fuel cycles are based on enriched uranium (Table 2.1-1). Heavy water reactors and graphite-moderated reactors can even use natural uranium as these moderators have much lower neutron capture cross sections than light water.

Table 2.1-1: The most common commercial nuclear reactors in the world.

Reactor*	*PWR*	*BWR*	*GCR*	*PHWR*	*LWGR*	*FBR*
Fuel	Enriched UO_2 / MOX	Enriched UO_2 / MOX	Enriched UO_2 / Natural UO_2	Natural UO_2	Enriched UO_2 / MOX	MOX / Enriched UO_2
Coolant	H_2O	H_2O	CO_2	D_2O	H_2O	Na
Steam generation	indirect	direct	indirect	indirect	direct	indirect
Moderator	H_2O	H_2O	graphite	D_2O	graphite	none
Number in operation**	266	92	14	46	15	1

*See page 122 for the list of abbreviations.
**as of 01.05.10; Source: World Nuclear Association.

Mixed oxides (MOX) fuels contain more than one oxide of fissile material, usually consisting of plutonium blended with natural uranium, reprocessed uranium, or

depleted uranium. These fuels are produced via nuclear reprocessing, recovering the plutonium from spent nuclear fuel and reducing at the same time the volume of high-level nuclear waste and its radio-toxicity. These fuels are used in thermal reactors together with low-enriched uranium, accounting for up to 30% of the total fuel.

A less common alternative to thermal reactors is based on the use of fast neutrons, which do not have a neutron moderator, and use less-moderating coolants: these systems have the potential to produce less transuranic waste because all actinides are fissionable with fast neutrons but they are more difficult to build and more expensive to operate. They would require the fuel to be more highly enriched in fissile material (about 20% or more) but fast breeder reactors (FBR) work mostly with MOX fuels and are capable of producing more fissile material than they consume during the fission chain reaction (by converting fertile ^{238}U to ^{239}Pu, or ^{232}Th to ^{233}U).

In general, the oxide form of uranium is preferred to the metallic element for fuel production. The reason for this is that UO_2 is temperature resistant and unlike metallic uranium does not undergo phase transformations at the temperatures reached in the reactor (to be expected considerably above 1000°C). Another reason is that ceramic oxides better resists to radiation damage, even though their heat conductivity is poor and limits the dimension of the fuel pellets.

All this considered, uranium, and more specifically UO_2, is the main component of the fuel and of the nuclear waste and therefore the main subject of the nuclear fuel cycle [4]. The nuclear fuel cycle starts with the recovery of the uranium containing minerals and ends with the final storage of the nuclear fuel that was used in the reactor. Each phase of this cycle – not ultimately the different reactor designs – has an influence on the chemical composition and physical structure of the material and eventually on the disposal behaviour of the spent fuel.

2.1.1 From the ore to the reactor

Uranium is a slightly radioactive metal that occurs throughout the Earth's crust and appears in at least 60 different minerals. It is about 500 times more abundant than gold and about as common as tin, arsenic or boron. It is present in most rocks and soils as well as in many rivers and in sea water. It is, for example, found in concentration of ≈ 4 µg/g in granitic rock bodies, which were formed by slow cooling of magma ≈ 10^9 years ago and represent up to 60% of the Earth's crust. It is found in higher concentrations in younger rocks: the most important uranium mineral is uraninite, or pitchblende, in which uranium concentration is 50-90% [5].

Most of the radioactivity associated with uranium in nature is in fact due to other minerals derived from it by radioactive decay processes, and which are left behind in mining and milling. The process used for the extraction of uranium varies from place to place, as the composition of the ore is different. In general, after the mining and crushing, the ore is dissolved in sulphuric acid and the dissolved uranium is separated by resins or solvent extraction. The final product is the so-called yellow cake, ammonium diuranate containing 65-70% of uranium. This is afterwards purified

to give U_3O_8 with purity above 99.98% and treated thermally in presence of hydrogen to obtain UO_2 [5].

For the ^{235}U enrichment step, UO_2 is dissolved in hydrofluoric acid and exposed to fluorine gas. The resulting relatively volatile UF_6 can be used as feed for the two possible enrichment processes used for large-scale production: gas diffusion through porous membranes and centrifugation. Both processes use the 1% mass difference between the two uranium isotopes, ^{235}U and ^{238}U, to separate them and the fact that fluorine consists of only one isotope, ^{19}F.

The enriched UF_6 is then converted back into oxide via hydrolysis, precipitation and reduction. The precipitate is pressed into "green pellets", which have 50% of the theoretical density of UO_2, and then sintered at 1700°C until a nearly stoichiometric material is obtained ($UO_{2.05}$).

The sintered pellets typically have a density of 95% because of 5% closed-pore porosity. The density of the fuel is a very important feature for the behaviour in the reactor: if it is too high, the production of fission gases in the reactor will cause a swelling of the material and potentially deformation and failure of the cladding; if it is too low, irradiation will lead to the shrinking of the pellet, causing reduced heat transfer of the material and the temperatures reached in the centre of the pellet will be too high [5].

Most commercial fuel pellets are made in the shape of cylinder of ≈ 8-10 mm of diameter and 9-15 mm of height. A fuel rod consists of many of these pellets stacked up into cladding pins, metallic tubes of zircaloy or stainless steel that have the function of protecting the fuel from corrosion and the coolant circulating the reactor from radioactive contamination. For most reactors the cladding is a tube of 1 cm of diameter made of Zircaloy-2, a zirconium-based alloy containing 1.3-1.6% tin and 0.23-0.32% chromium, nickel and iron). Empty spaces, including a narrow annular gap between the fuel pellets and the surrounding cladding, as well as the space at the ends of the fuel rods, are first evacuated from the presence of moisture and then, prior to sealing, pressurised with helium gas to improve heat transfer. During reactor operation, the gap closes as the fuel expands slightly during irradiation. The type of fuel rod assembly used depends on reactor design but typical fuel assemblies are 4 m long and can weigh as much as 500 kg, with hundreds of fuel rods bundled together [4].

2.1.2 In-reactor behaviour

In a typical LWR, the fuel is exposed to a thermal neutron flux (≈ 0.025 eV) [4] that causes two principal types of nuclear reactions: fission of ^{235}U and neutron capture of ^{238}U (followed by β-decay).

The most common nuclear fission process is binary fission, which produces two charged asymmetrical fission products with maximally probable charged product at 95±15 and 135±15 atomic mass units. A large number of fission products are so created, with masses ranging between 70 and 160 u [6]. Ternary fission, where three

fission products are formed instead of two, can lead to the formation of lighter elements, like He, but is less probable.

Neutron capture instead results in the production of heavier actinides, e.g. neptunium, plutonium, americium and curium. The α-decay of these elements leads to the production and accumulation of α-particles, so helium gas is formed both in the fuel and in the reactor material [7].

The final composition of the fuel depends on the initial fuel type, chemical composition, the level of enrichment of ^{235}U, the neutron energy spectrum, and the fuel utilisation, or "burn-up". The burn-up can be expressed both as the fraction of fuel atoms that underwent fission in percent and as the actual energy released per mass of initial fuel in gigawatt-days/metric ton of heavy metal (GWd/tHM), or similar units. As a rule of thumb, a burn-up of 40 GWd/tHM results in the conversion of 4% of the uranium to approximately 3% fission products and 1% transuranium elements. A typical burn-up is in the range of 35 to 45 GWd/tHM, but it is likely that higher burn-up will be attained in the future [4].

The fission products travel into the fuel matrix discharging energy and displacing other atoms from their initial positions, leading to the formation of defects in the crystalline structure of the fuel. These defects can be thermally annealed in the parts of the fuel where temperature is above 700°C but in the more external and cooler parts of the rod the damage caused to the structure is permanent and increases with the working life of the fuel. Together with this, temperature and neutron flux gradient cause cracks and diffusion of gaseous fission products create bubbles. Other secondary phases represented by small metallic particles and perovskite-type crystals are precipitated or segregated along the cracks and the grain boundaries. At high burn-up (above 60 GWd/tHM) a more radical re-structuring of the matrix occurs, which is referred to as "rim structure" as it is principally visible at the periphery of the fuel. In this case, a sub-grain microstructure is formed, with typical grain size 0.2-0.3 μm, and at the same time, volatile fission products accumulate in pores of 1-2 μm of diameter. The thickness of this rim structure is correlated to the burn-up itself [8].

The fission products and the heavier actinides have been classified in four groups by Kleykamp [9, 10], according to their chemical state in the fuel.

Group I - volatile and gaseous fission products: Kr, Xe, Br, I, (He);
The noble gases Kr and Xe (and the less abundant He) are insoluble in UO_2 and are dynamically distributed between a fission-induced solution within the oxide lattice and closed bubbles that can be both intra- and intergranular. The other volatile fission products, the halogens Br and I have been found to diffuse two orders of magnitude faster than Xe, and therefore tend to be released in the fuel clad gap, where, unlike the noble gases, can be chemically reactive with the other species present (for example with the material of the cladding).

Group II - metallic precipitates: Mo, Tc, Ru, Rh, Pd, Ag, Cd, In, Sn, Sb, Te;
Among these elements, great importance is given to the formation of alloys between Mo, Tc, Ru, Rh and Pd, whose composition is dominated by Mo and Ru: these are the so-called ε-particles or "white inclusions", precipitated mostly at the grain-

boundaries. Pd, nevertheless, tends to form also intermetallic compounds and ingots with Ag, Cd, In, Sn, Sb, Te that can be found in the gap and in the central void of the FBR fuel pins.

Group III - oxide precipitates: Rb, Cs, Ba, Zr, Nb, Mo, Te;
A number of other fission products belonging to this group precipitate in the form of a complex oxide, which is referred to as the "grey phase." The composition of the grey phase precipitates will vary with fuel composition and reactor history, but in general it has the structure of perovskite ($CaTiO_3$) and has as main constituents Ba, Sr and Cs as substitute for Ca and Zr, Mo, U, Pu and rare earths as substitute for Ti. The most commonly reported precipitates are perovskites of the type $[Ba_{1-x-y}Sr_xCs_y](U, Pu, Ln, Zr, Mo)O_3$. The grey phase accumulates at the grain boundaries of the colder parts of the fuel. There are continuous transitions between the second and third group due to similar oxygen potential of some fission product oxides and the fuel. This is the case of molybdenum: as the oxygen potential increases with the fuel burn-up, the amount of oxidised molybdenum increases while the Mo fraction in the metallic precipitates decreases [10].

Group IV - oxides dissolved in the fuel matrix: Sr, Zr, Nb, Y, La, Ce, Pr, Nd, Pm, Sm, Eu (and actinides).
The elements belonging to this group form solid solution with the UO_2 matrixes.
Also between the third and the fourth group there is a continuous transition due to the burn-up dependent distribution coefficients of the respective cations in both of the oxide phases [9]. Rare earths in oxide form are largely soluble in UO_2 but at higher burn-up small fractions of these elements can be also found in the perovskite-type oxides just mentioned [10].

The chemical state of the fission products and their distribution within the fuel is particularly important for the assessment of the fuel performance and also for the prediction of the dissolution and mobilisation of these elements in case the spent fuel becomes in contact with water.
The volatile products of the first group are expected to dissolve quickly in case of contact with groundwater and thanks to their mobility they are located in the parts of the fuel immediately accessible to water. The metallic precipitates of the second group are also expected to dissolve in groundwater. Nevertheless, they are located mostly at the grain boundaries and most of the grain boundaries are not immediately accessible to water. Therefore, their dissolution will be controlled to a significant degree by the corrosion/dissolution of the fuel matrix [11]. This is also the expected behaviour of the grey phase oxide of the third group, which are distributed in the entire fuel but tend to accumulate at the grain boundaries of the colder parts of the fuel: they are assumed to dissolve in water but their release is mainly controlled by the oxidation and dissolution of the fuel matrix. The oxide dissolved in the fuel matrix (fourth group), which represent roughly 30% [12] of the fission products, are then the least likely to dissolve in groundwater. In reality, due to the reduced mobility of the non-soluble ones belonging to the other three groups, up to 95% of all the fission products are actually located in the UO_2 lattice and can be released only upon dissolution of the matrix itself [13].

2.1.3 Back-end

The so-called back-end of the fuel cycle is constituted by all the operations necessary for the management of the nuclear fuel once it has been extracted from the reactor. Initially, the spent nuclear fuel is stored ad interim in water pools that act both as a coolant and as a shield for the residual radioactivity. These pools can be located at the reactor sites or in common facilities located elsewhere. After at least one year of cooling the material is in some cases moved to dry cask storage, which is designed also as an interim solution. In most cases spent fuel is stored in the pools for a period of up to tens of years, depending on the capacity of the site.

Two different management strategies are used for spent nuclear fuel. In one the fuel is reprocessed to extract usable material (uranium and plutonium) for new fuel. In the other, spent fuel is simply considered a waste and is stored pending disposal. As a result, the two main kinds of nuclear waste forms considered for deep geological repository in Europe are vitrified high level waste (HLW) and spent fuel itself (SF), in the case that it is considered a waste form (Table 2.1-2) [14].

Table 2.1-2: Characteristics of some of the geological disposal projects in the world.

Country	*Location name*	*Waste*	*Geology*	*Depth (m)*	*Status*
Belgium		HLW	Boom Clay	225	Under discussion
Canada		SF	Argillaceous rock	500-1000	Under discussion
Finland	Olkiluoto	SF	Granite	400	Licence application 2012
France	Meuse/ Haute-Marne	HLW	Argillaceous rock	500	Siting
Germany	Gorleben	HLW / SF	Salt dome		on hold
Sweden	Forsmark	SF	Granite	450	License application 2011
Switzerland	Zürcher Weinland	HLW / SF	Opalinus Clay	650	Siting
UK	Cumbria/Norfolk	HLW / SF	Crystalline rock/limestone		Under discussion
USA	Yucca Mountain	SF	Volcanic tuff	300	Cancelled

In fact, the spent fuel matrix itself – constituted for a 95% of uranium dioxide – can offer a suitable barrier against the widespread of radionuclides in the environment, keeping them trapped in its structure as long as the chemical environment of the

repository can ensure that the solubility of UO_2 is low. The definition of the kind of waste determines the first parameter for the choice of the suitable disposal approach, the so-called “source term”. France, Russia, Japan, India and China reprocess most of their spent fuel, while the USA, Canada, Finland and Sweden have currently opted for direct disposal.

Nature itself has suggested how bedrock formation can be considered suitable for final storage. In fact, the study of the Oklo natural nuclear reactor, in Gabon, that was active 1.7 billion years ago for thousands of years, has shown that uranium and the fission products were transported no more than a few meters away from the zone of sustained fission and were deposited in the surrounding rocks [15]. However, other natural environments have been suggested and investigated by different countries according to their own special needs and natural availabilities, like clay and salt formations [16]. The characterisation of the geological strata and water circulation is included in what is often referred to as “far field studies”. The term “near field” instead involves the study of the interactions between the waste forms and the additional man-made barriers that separate them from the geological ones: first the engineered canisters for their containment, then a so-called buffer or additional barrier represented by the filling of the cavity.

Steel canisters are often used, especially for vitrified HLW. Copper has been identified as a suitable canister material for the direct disposal of spent fuel due to its resistance to corrosion and natural abundance in the earth's crust. The Swedish Nuclear Fuel and Waste Management Company (SKB) has developed the KBS-3 concept which is globally the closest to implementation, where steel-reinforced copper canisters are used instead (Figure 2.1-1) [17].

A schematics of the KBS-3 concept is represented in Figure 2.1-2, showing also additional barriers. The gap between the canister and the bedrock is filled by a buffer. Bentonite clay is chosen for this purpose, ensuring flexibility against crust movements and an absorbing media against water penetration.

The safety of a geological disposal has to be assessed over very long time scale: 10^5 years. This is the time needed for the radioactivity of the spent fuel to decrease to the same level as that of the uranium ore from which the fuel was originally fabricated. Complex predictions need to be made. Prediction of the chemical environment will depend on many aspects. For example, the kind of radiation field expected to be emitted from the spent fuel will depend on the time after which failure of the canister can be expected.

Figure 2.1-1: Various parts of the canister: steel cylindrical structures, with cavities for the allocation of fuel assemblies, and the copper outer body (at the SKB Canister Laboratory in Oskarshamn, Sweden).

It has been estimated that in 10^5 years only a few millimetres of the 5 centimetres thick outer copper body will be completely corroded [18], despite other studies consider the expected lifetime of copper container much shorter [19]. The gamma radiation field at the surface of the fuel will decay to insignificant levels after a few hundred years while alpha and, to some extent, beta radiation fields will remain significant for more than 10^5 years [20]. Therefore, it is alpha activity that is most likely to determine the chemical products of radiolysis of water, which in turns determines the oxidising potential of the environment. In fact, the atmosphere can be considered oxygen-free as any oxygen introduced during repository construction and operation prior to its sealing will be rapidly consumed [11].

Finally, the composition of groundwater will participate in determining the dissolution process. All these aspects will be discussed in detail in the following paragraphs.

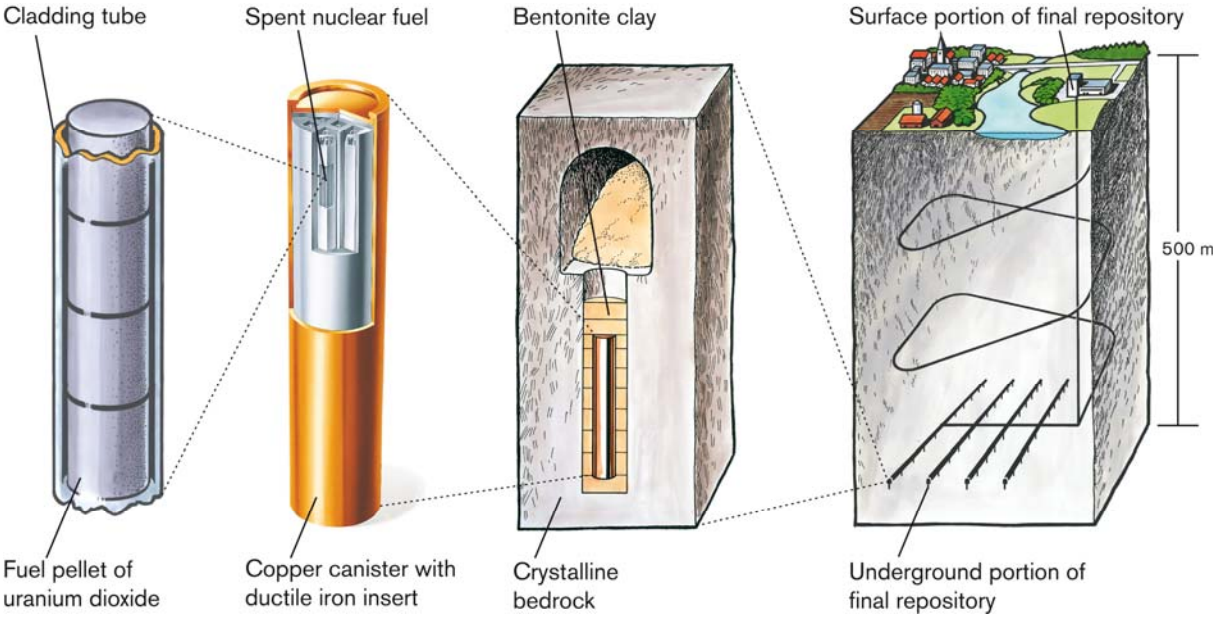

Figure 2.1-2: The KBS-3 concept: schematics of the geological disposal for spent nuclear fuel planned to be constructed in Forsmark, Sweden (source: SKB; illustrator: Jan Rojmar).

2.2 Fuel Corrosion

As introduced earlier (Paragraph 2.1.2), the release of most of the radionuclides contained within the solid-state matrix of the spent fuel will be governed by the dissolution of the fuel matrix itself. In this sense, the mechanisms for water penetration in spent nuclear fuel need to be assessed.

In the following paragraphs, the oxidative dissolution of UO_2 in the chemical environment expected for geological disposal is discussed. For this reason, a brief summary of the chemical and physical properties of UO_2 is given with particular focus on oxygen diffusion as a fundamental aspect governing the mechanism of UO_2 dry and wet oxidation, which in turns is the key step towards dissolution.

2.2.1 Uranium Dioxide

UO_2 is a ceramic material, thus it has a high melting point, T_m = 3151 K. UO_2 is a semiconductor, as its band gap is comparable to these of silicon and gallium arsenide and its intrinsic conductivity at room temperature is about the same as of single crystal silicon.

Crystalline UO_2 has the structure of the same kind of fluorite, CaF_2 (Figure 2.2-1a), in which the cations have a face-centred cubic arrangement with the anions occupying both types of tetrahedral sites.

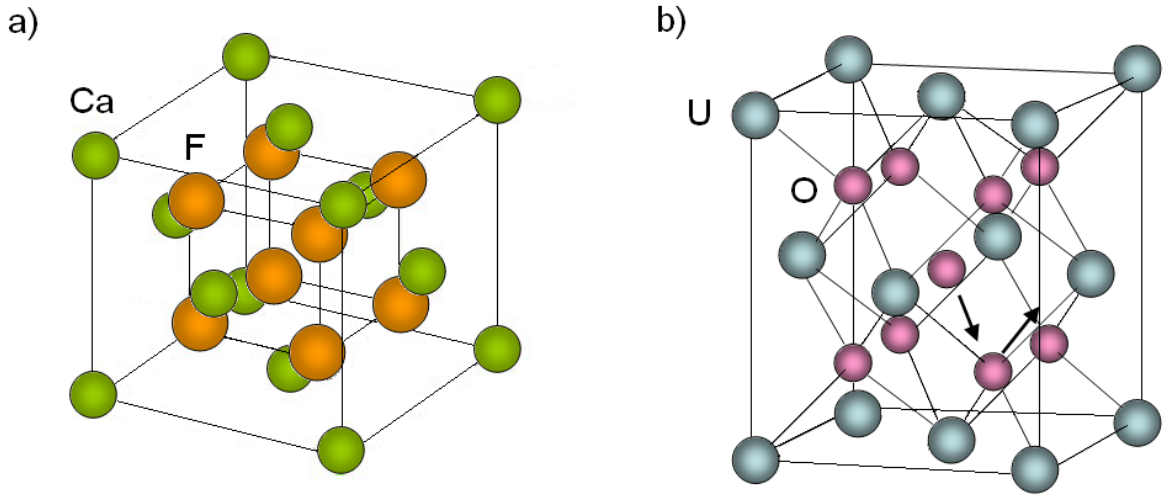

Figure 2.2-1: Crystalline structure of UO_2: a) the CaF_2 structure; b) schematic representation of oxygen interstitial diffusion in UO_2. The interstitial oxygen atom located initially at the centre of the cube migrates to the tetrahedral site and the tetrahedral oxygen to the neighbouring octahedral interstitial site (black arrows).

The fluorite structure is typical for AX_2 compounds where A is a sufficiently large cation that forces the anions apart and into a less than close-packed arrangement. The oxides ZrO_2, HfO_2, CeO_2, ThO_2, PuO_2 all possess the fluorite structure. The fluorite structure has large (½;½;½) octahedral interstices that are unoccupied for the

stoichiometric compositions and are potential sites for impurity atoms as well as for oxygen intrusion. Hyper-stoichiometric oxides, commonly indicated as UO_{2+x}, are in fact characterised by the presence of excess oxygen atoms sitting in the interstitial positions and representing a point defect of the lattice.

Lattice defects and stoichiometry

All deviations from the stoichiometric composition are directly related to the presence of point defects, *i.e.* a disruption of the regular pattern of a crystal that occurs at or around a single lattice point. The so-called line or plane defects are in fact constituted by an arrangement of point defects, which are essentially of two kinds: vacancies and interstitial.

Vacancies, or Schottky defects, are lattice sites which would be occupied in a perfect crystal, but are vacant. If a neighbouring atom moves to occupy the vacant site, the vacancy moves in the opposite direction. Interstitial defects are instead atoms that occupy a site in the crystal structure not usually occupied by any atom. They are generally high-energy configurations (except for small atoms in certain cases, like hydrogen in palladium). If an atom leaves a normal site to create a vacancy and goes to occupy instead a nearby interstitial position, a Frenkel defect (or Frenkel pair) is created (see Figure 2.2-1b).

In stoichiometric crystals, complementary defects are present, and their number depends on the thermodynamics; for this reason they are referred to as thermal defects [21, 22]. In semiconductors like UO_2, a deviation from stoichiometry is accompanied by a large increase in the concentration of the point defects, because the electrical neutrality is conserved through the formation of point defects and charge compensating electronic defects. Non-stoichiometric oxides may – depending on the oxide, temperature and activities of the components – have an excess or deficit of metal or oxygen. For this reason, in $UO_{2\pm x}$ additional defects are created and their number depends on x. In UO_2, as in many transition metals compounds, thermal defects dominate over structural ones (induced by non-stoichiometry) for temperatures above one half of their melting point [23].

Because of the fluorite-type structure, in the case of UO_2 the predominating defects are oxygen interstitials, or complex defects based on these. At any rate, the introduction of excess oxygen is accompanied by the formation of vacancies in the normal oxygen sites, while the uranium sublattice is not disturbed [24, 25]. In UO_2 the point defects considered for diffusion are oxygen and uranium Frenkel pairs and the so-called Schottky trio, which is a neutral trivacancy given by the combination of two oxygen vacancies and one uranium vacancy. Thus, the alteration process for which some of the uranium atoms change their oxidation state from +4 to +5 or +6 proceeds through oxygen incorporation and diffusion into the matrix via vacancies and interstitials. Typically, interstitial diffusion is faster than vacancy diffusion.

UO_2 has a very wide single-phase range of non-stoichiometry, with O/U ratios from 1.65 to 2.66 [26]. While hypo-stoichiometric UO_{2-x} exists only at high temperature, formation of UO_{2+x} is difficult to avoid even at room temperature, as in presence of air UO_2 is not considered thermodynamically stable [27]. The U-O system contains a

series of higher oxides as well, notably U_4O_9, U_3O_7, U_3O_8 and UO_3. Some of these occur in several crystallographic modifications showing various degrees of non-stoichiometry.

The single-phase fluorite-type structure is retained up to x = 0.25, *i.e.* U_4O_9. For x = 0.33, *i.e.* U_3O_7, the structure assumes a squared geometry (but very close to the cubic structure). U_3O_8, for which x = 0.67, has instead an orthorhombic structure [28]. The structural evolution is coherent with the evolution of the density, which linearly increases from 10.96 g/cm^3 of $UO_{2.00}$ to 11.20 g/cm^3 of U_3O_7 and then abruptly decreases to 8.34 g/cm^3 of U_3O_8 when the crystallographic structure changes so much that the increase of the ratio O/U no longer causes a volume contraction [27].

2.2.2 Oxidation of UO_2 in air

The oxidation of UO_2 in air at temperatures below 400°C has been generally described as a two-step reaction, with two successive rate-limiting mechanisms [29-31]:

$UO_2 \rightarrow U_4O_9/U_3O_7 \rightarrow U_3O_8$

1) Oxidation of UO_2 to U_3O_7
This step is controlled by the diffusion of oxygen through the more oxidised layer which is formed on the surface. The rate determining step appears to be a surface/interface reaction involving the incorporation of oxygen ions into stable interstitial clusters in the host UO_2 matrix at the UO_2/U_3O_7 interface. The diffusion of oxygen interstitials beyond this interface into the bulk UO_2, to form a UO_{2+x} phase was not observed [31]. The phase U_4O_9 is prevalent in spent fuel while general consensus on oxidation of unirradiated UO_2 powders is that the phase U_3O_7 is formed instead [30].

2) Formation of the swelling oxide U_3O_8
This step follows a nucleation and growth mechanism. According to some reports, formation of U_3O_8 is not actually encountered below 531K, but this could be rather due to a slow kinetics [30]. In fact, Tempest *et al*. [31] reported that U_3O_8 was not observed initially at grain boundaries during the incubation period, but nucleated at micro-cracks after the onset of inter- and intra-granular cracking created by the growth of the U_3O_7 layer. Tempest *et al*. [31] also report that oxygen penetration had reached ≈ 30 µm after 1255 h at 503 K due to faster diffusion along grain boundaries. Schematics of the reaction mechanism proposed by Tempest *et al*. [31] are shown in Figure 2.2-2.

The first step of this oxidation process has been modelled on the basis of measurements of the diffusion coefficient of oxygen in UO_{2+x} that, as it will be discussed later on, did not distinguish between the different oxidised phases, giving an estimate of the activation energy for oxidation in the range 75-125 kJ.

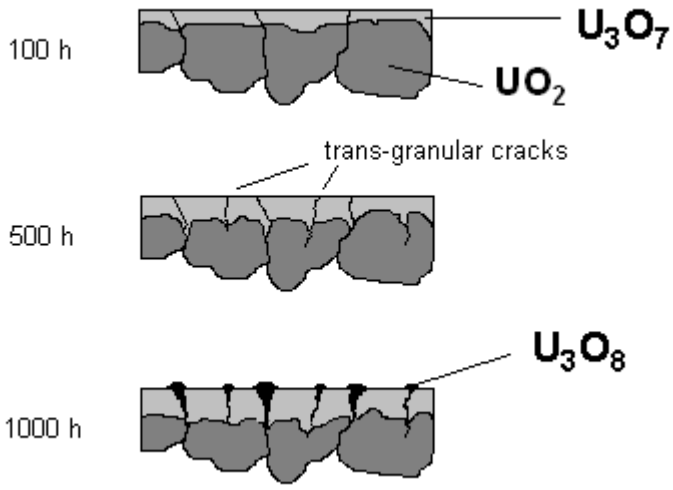

Figure 2.2-2: Schematics of oxidation of UO_2 at 230°C in air: scheme produced according to Tempest *et al*. [31].

More recent experimental findings indicate a different mechanism, where both reactions occur simultaneously [28]:

$UO_2 \rightarrow U_4O_9$

$U_4O_9 \rightarrow U_3O_7$

And two different activation energies (and diffusion coefficients) could be calculated for the two phases. The process of oxidation can then be described in this way:

Stage 1- Incorporation of oxygen results in the formation of U_4O_9

U_4O_9 has shown to be characterised by a crystalline superstructure represented by oxygen "cuboctahedra", which is a way to stabilize oxygen interstitials as lattice defects in UO_{2+x}, at least at temperatures below 300°C.

This stage can be described as a sequence of elementary steps:

- Adsorption of the O_2 molecule;
- Dissociation on the surface;
- Incorporation of the oxygen atom in UO_2;
- Point defect diffusion;
- Formation of cuboctahedra;

The slowest elementary step that limits the kinetics of this stage is normally considered the oxygen diffusion; considering that cuboctahedra are large structures not likely to diffuse, the point defect involved in the diffusion process is more likely to be oxygen vacancies.

Stage 2- formation of U_3O_7 on the surface

Due to oxygen diffusion, in the U_4O_9 layer on top of UO_2 an oxygen concentration gradient is developed. When a concentration threshold has been reached, the cuboctahedra can start interact with each others and their dynamic rearrangement creates U_3O_7 on the surface. As a result, the kinetics of U_3O_7 oxidation is slower than the U_4O_9 oxidation: the diffusion of oxygen point defects become slower in U_3O_7.

Stage 3 – formation of U_3O_8
In order to achieve this step, it is then clear than both sufficient oxygen concentration and incubation time are needed.

2.2.3 Oxidation of UO_2 in water

It has been recognized that oxidation in air and in water follow different mechanisms. The activation energy for oxidation of UO_2 in water in the temperature range 90-200°C is significantly lower (20-40 kJ/mol) than the activation energy for oxidation in air (104 kJ/mol) [32].

The oxidation of UO_2 in water may proceed to the stage $UO_3 \cdot xH_2O$ (with x=0.8 for example, according to Aronson [33]) while in air, as discussed in the previous paragraph, it is expected to proceed to U_3O_8. In fact, U_3O_8 is not encountered in nature because the presence of water in the environment would lead to the formation of shoepite ($UO_3 \cdot 2H_2O$) or ianthinite ($U(UO_2)_5(OH)_{14} \cdot 3H_2O$), also due to radiolysis of water and in absence of other cations [34].

Nevertheless, it was shown that corrosion of UO_2 in contact with air-containing water proceeds via the formation of UO_{2+x} and U_3O_7 [35-37]. Matzke [38] showed that leaching of single-crystal UO_2 in water at temperatures up to 200°C, for a time period of less than 500 h, produced a water-free layer of U_3O_7. The inward growth of this layer was controlled by diffusion of oxygen through it and the thickness would depend on experimental conditions such as temperature, pH and contact time (100-500 nm for experiments in alkaline solutions lasting ≈ 24h at ≈ 200°C). Between the layer and the UO_2 bulk there was a thin (≈ 5 nm) distorted transition layer that likely coincided with a U_4O_9 phase and whose thickness did not seem to vary.

Torrero *et al.* [39] showed that during leaching at room temperature, in non-complexing aqueous solutions surface stoichiometry was independent of the oxygen partial pressure rather than on the pH; at alkaline pH the surface stoichiometry was shown to be $UO_{2.25}$.

However, whether the oxidised surface phase is U_4O_9 or U_3O_7, UO_2 samples leached in water at room temperature, the initial steps for the oxidation may be quite similar to the oxidation of UO_2 in air. Oxidation in water is expected to follow the first steps of the process described in the previous paragraph: diffusion of oxygen, formation of oxygen interstitials cluster defects like cuboctahedra and consequent development and migration of oxygen vacancies towards the surface [32].

Skomurski *et al*. [40] have found that the discrepancy in activation energy values derived from experimental data versus those calculated using theory and involving experimental data suggest that O diffusion may not progress via an interstitial hopping mechanism for all values of x in UO_{2+x}. Gupta *et al*. [41] also conclude that both vacancies and interstitials contribute almost equally to diffusion.

The presence of vacancies causes the reactivity of the surface towards water molecules. Senanayake [42] reports that annealed stoichiometric surfaces do not dissociate water molecules, while O-defected UO_{2-x} surfaces dissociatively adsorb water molecules in order to restore the UO_2 structure, with consequent hydrogen evolution.

In order to evaluate quantitative correlation between rates of oxidation in air and reaction rates for UO_2 in water, it is important to derive a diffusion coefficient for oxygen at room temperature. This is complicated by the fact that studies are typically carried out at temperatures above 200°C, as discussed more extensively in Paragraph 2.2.5.

2.2.4 Fuel Oxidation

The oxidation mechanism of spent fuel matrix and UO_2 pellets are quite different. The rate of oxidation is much higher in irradiated fuel than in non-irradiated materials: irradiated LWR fuel has parabolic kinetics similar to that of the oxidation of UO_2 powder with particle size equal to the grain diameter. This means that spent fuel is characterised by rapid grain boundary oxidation, due to the fact that closely packed fission gas bubbles along grain boundaries creates pathways for penetration of oxygen [43].

The overall rate of oxidation of spent fuel is therefore given by a combination of matrix and grain boundary oxidation [44]: initially the oxidation rate is low because only the geometric surface area is available for oxidation, but it increases until all grain boundaries are oxidised, when the total grain surface area becomes accessible to oxidation.

The oxidation of UO_2 affects the mechanical stability of the fuel: formation of U_3O_8 in a defected fuel rod can lead to splitting of the material and detachment of grains due to the 36% volume increase consequent to oxidation of UO_2. The formation of the intermediate U_3O_7 is considered to have less of an impact on fuel integrity, but the kinetics of this formation strongly affects the following oxidation step, as already discussed for non-irradiated UO_2 [31].

In the oxidation of spent fuel, the phase U_4O_9 is encountered preferentially than U_3O_7 but with stoichiometry as high as $\approx UO_{2.4}$. A possible explanation is that the presence of fission products stabilizes the U_4O_9-type cubic structure [45]. In fact, the same behaviour has been observed for SIMFUEL, where stable isotopes representing the fission products and actinides are added to a natural UO_2 polycrystalline matrix [38].

Spent fuel oxidation at temperatures above 100-300°C seems to occur slightly faster than UO_2 oxidation but with a higher activation energy than that of UO_2 (134 kJ instead of 104 kJ), meaning that with decreasing temperature the rate of the two processes become almost identical. Considering the high concentration of defects, it is not likely that oxidation rate of spent fuel will be lower than that of UO_2 so that activation energy should not be used for extrapolations at room temperature [32].

Thomas *et al*. [46] reported that on exposure to low temperature air, typical PWR spent fuel initially oxidises by forming U_4O_9 along UO_2 grain boundaries beginning simultaneously from the UO_2 grain corners without indication of enhancement at the fragment surfaces. The U_4O_9/UO_2 interface advances then into the grains with an average rate of 4.7 nm per hour, as measured at 195°C.

2.2.5 Oxygen diffusion in UO_2

A key aspect for oxidation of UO_2 in air and in water is oxygen diffusion. For this reason, oxygen diffusion in UO_2 has been extensively studied. A number of measurements of oxygen diffusion coefficients have been published, mostly as a result of high-temperature experiments.

In this section, a brief introduction on the diffusion phenomena in solids, and the terms involved in describing it, is given. The available data for UO_2 are also presented, together with the problem of the large uncertainty arising from their extrapolation to the expected temperature in a final repository (20-90°C)[47].

Fickian diffusion

Diffusion is the transport of atoms through the matter. In general terms, diffusion of mass is dependent on differences in concentration, temperature and pressure. In condensed matter, thermo-diffusion and baro-diffusion are usually negligible compared to concentration-dependent diffusion. Adolf Fick [48] was the first to give a model for diffusion based on random mobility of particles and determined by a transport of mass from regions of high concentration to regions of low concentration, with an equilibrium state of uniform concentration.

Fick's laws are frequently used to describe diffusive processes in fluids as well as in solids. Diffusion phenomena that cannot be described applying these laws are defined as non-fickian. This is, for example, the case of diffusion in polymer or resin, where a sharp front separates a dry region from a swollen region. Fick's first law relates the diffusive flux to the concentration under the assumption of steady state. It postulates that the diffusive flux, *J*, goes from regions of high concentration to regions of low concentration, with a magnitude that is proportional to the concentration gradient in the spatial derivative. The constant of proportionality is known as the diffusion coefficient, *D*. The diffusion coefficient is proportional to the squared velocity of the diffusing particles, which depends on the temperature, the viscosity of the fluid and the size of the particles, according to the Stokes-Einstein relation [49].

In two or more dimensions, Fick's first law can be written as:

$$J = -D\nabla\xi \qquad \textbf{2.2.5-1}$$

where ∇ is the del operator and $\xi(x,y,t)$ is the concentration. From Fick's first law and the principle of mass conservation, Fick's second law can be derived, relating the concentration change as a function of time to the change in flux with respect to position, hence predicting how diffusion causes the concentration to change with time, *t*.

In two or more dimensions, Fick's second law is:

$$\frac{\partial \xi}{\partial t} = D\nabla^2 \xi \qquad \textbf{2.2.5-2}$$

Where ∇^2 is the Laplacian operator.

The typical solution given by Cranck [49] can be used to describe a simple case of diffusion with time in one dimension, where the concentration is defined as *c(x,t)*. Considering diffusion along the x-axis from a starting point located at position x = 0, where the concentration is maintained at a value c(0), the concentration *c(x,t)* can be expressed as:

$$c(x,t) = c(0)erfc\left(\frac{x}{2\sqrt{Dt}}\right) \qquad \textbf{2.2.5-3}$$

where *erfc* is the complementary error function. The quantity $2\sqrt{Dt} = \lambda$ represents the diffusion length and provides a measure of how far the concentration front has propagated in the x-direction by diffusion within the time *t*.

Self-diffusion and chemical diffusion

Different terms are used to distinguish between the different kinds of diffusion phenomena occurring in solids. The term *interdiffusion* is used for diffusion of an impurity within a different compound; diffusion of atom through their own lattice is described instead with the terms *self-diffusion* or *chemical diffusion*. Self-diffusion describes the random-walk, or Brownian movement, of atoms through their own lattice. In this case, the sample is assumed to be chemically homogeneous: there is no gradient within the crystal. Self-diffusion coefficient of the species *i* is indicated as D_i *. The chemical diffusion coefficient is, according to IUPAC recommendations [50], the diffusion coefficient of a species in presence of a concentration gradient and it is normally indicated as $\tilde{D}_i$.

In a concentration gradient, the migrating atoms are subject to a driving force which is proportional to the gradient of the chemical potential. Darken [51] has shown that the chemical diffusion coefficient of a species in a binary system can be written as:

$$\tilde{D}_1 \equiv D_1 = (N_2 D_1^* + N_1 D_2^*)\frac{d\ln a_1}{d\ln N_1} \qquad \textbf{2.2.5-4}$$

where N_i is the atomic fraction of species i=1,2; D_i^* is the self-diffusion coefficient of species i=1,2 and a_1 is the activity of species 1. The formula is general, independent of the mechanism of any particular diffusion process and expresses the relationship between the chemical and self-diffusion coefficient of the same species.

Effect of stoichiometry

When studying diffusion in solids, one must take into account material properties that can affect the mobility of a species within a lattice. Diffusion in metals and non-metals, for example, will differ significantly, due to the different mobility of the electrons. In ionic solids, where the rule of charge neutrality applies, electrons can be considered as non-interacting particles [23]. Oxides with semiconductor properties, like UO_2, have similar diffusion characteristics that place them in an intermediate position between metals and ionic crystals.

As mentioned, lattice defects have a major promoting effect on the diffusion within the crystal and, in turn, the deviation from stoichiometry in $UO_{2\pm x}$ determines an increase of the number of defects [23]. In UO_{2+x} the concentration of oxygen interstitial defects corresponds roughly to the value of x, since these chemically induced defects are greater than the thermally induced ones. Due to this increase in the number of defects, diffusion in hyperstoichiometric UO_{2+x} will then be characterised by a larger coefficient [23].

Oxygen self-diffusion

For UO_2, self-diffusion of oxygen was extensively studied since the 1950's, mostly through high-temperature experiments (500-2500°C). In order to be applied to the modelling of the nuclear waste disposal issues, diffusion coefficients need to be extrapolated to temperatures several hundreds degree lower.

Most of the published data seem to agree that the self-diffusion coefficient of oxygen in UO_2 can be expressed according to the Arrhenius-type law (Belle [52] and references therein):

$$D^*\left[m^2/s\right] = 1.15 \cdot 10^{-4} \cdot \exp\left(\frac{-237000 \pm 4000}{RT}\right)$$

where R is the gas universal constant (8.314 J/(K·mol)) and T is the temperature in K[i]. Even though the agreement at high temperature is considered to be good, the extrapolation to lower temperature results in a large uncertainty due to the exponential dependence on temperature.

Furthermore, the strong dependence of the diffusion coefficient on the stoichiometry, makes it difficult to perform a reliable extrapolation to room-temperature. To describe the dependence of oxygen self-diffusion coefficient on temperature and

[i] In all formulas reported in the present work the gas universal constant R is expressed in J/(K·mol) and the temperature T in K, unless it is specified otherwise.

stoichiometry, Breitung [53] derived a simple model based on the dynamical theory according to which the self-diffusion coefficient of oxygen can be expressed in terms of the total number of Frenkel defects (oxygen vacancies and interstitials) and the migration enthalpies involved in the movement of vacancies and interstitials.

Using the values of *D** measured at temperatures T>600°C [52, 54-56] and considering how, at high temperatures in hyperstoichiometric oxides the main Frenkel defect is represented by oxygen interstitials, Breitung [53] calculated the semi-empirical relation:

$$D^{*}_{(x\geq 0)}\left[m^2/s\right] = 6.65\cdot 10^{-7}\cdot\left[x+\left(x^2+1.12\cdot 10^{4}\cdot\exp\left(\frac{-158590}{T}\right)\right)^{1/2}\right]\cdot\exp\left(\frac{-11980}{T}\right)$$

valid for UO_{2+x} and for temperatures at which interstitial diffusion mechanism dominates over vacancy diffusion. The corresponding curves are shown in Figure 2.2-3.

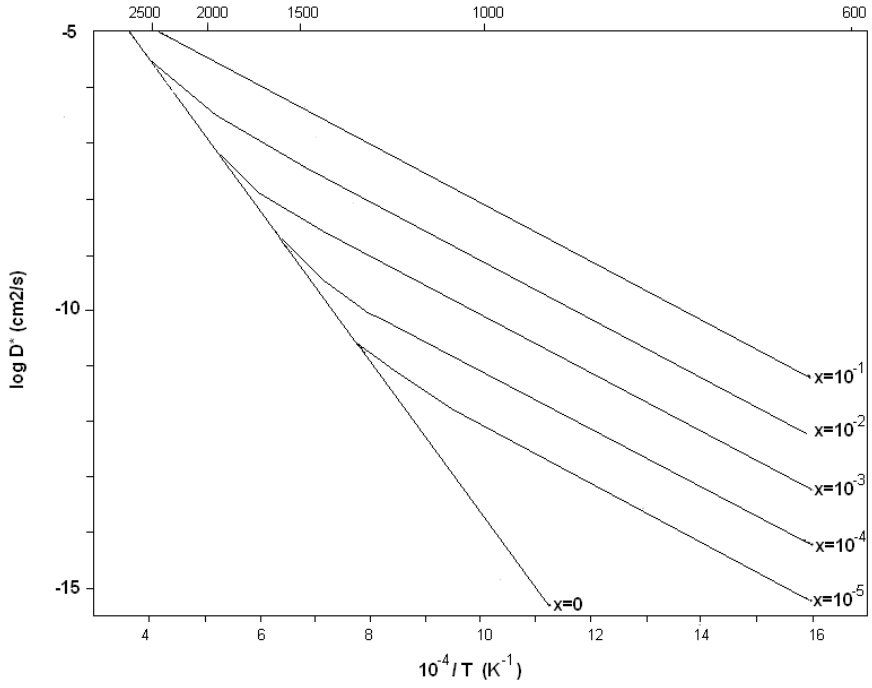

Figure 2.2-3: Calculated self-diffusion coefficients for oxygen in UO_{2+x} according to x: graph reproduced from Breitung [53]; the experimental data used to derive such curves come from (among others) Auskern and Belle [55], Marin and Contamin [54] Dornelas and Lacombe [56], Roberts *et al.*[52].

Studies of self-diffusion coefficient at lower temperature were carried out more recently by Fayek *et al.* [57, 58] to assess the oxygen exchange between uraninite minerals and meteoric water in the Athabasca deposits. These experiments are among the few self-diffusion studies carried out at lower temperature and focussing on naturally occurring uraninite minerals. These natural minerals differ from commercially available UO_2 as they contain impurities, such as SiO_2, CaO, PbO, FeO

and ThO_2, in quantities ranging from 7 to 18%, depending on the origin. These impurities influence the crystalline structure of UO_2 and control to a certain degree the oxidation process of doped UO_2 [45].

Nonetheless, from the experimental data of Fayek *et al*. [57] acquired between 400 and 600°C on a uraninite sample of average stoichiometry $UO_{2.005}$, oxygen self-diffusion coefficient was found to be expressed by the Arrhenius law:

$$D^*_{UO_{2.005}}\left[m^2/s\right] = 1.90 \cdot 10^{-9} \exp\left(\frac{-123382}{RT}\right) \qquad (400<T<600°C)$$

Experiments carried out by Fayek and Kyser [58] between 100 and 300°C on a different uraninite sample (with crystalline structure consistent with U_4O_9 structure but probably higher stoichiometry) provided this expression for the self-diffusion coefficient:

$$D^*_{UO_{2.25-2.67}}\left[m^2/s\right] = 3.1 \cdot 10^{-14} \exp\left(\frac{-63981}{RT}\right) \qquad (100<T<300°C)$$

Finally, from experiments carried out between 100 - 300°C on fine grained (5 - 5 µm) synthetic so-called UO_3 powder this expression was obtained:

$$D^*_{UO_3}\left[m^2/s\right] = 1.3 \cdot 10^{-19} \exp\left(\frac{-21197}{RT}\right) \qquad (100<T<300°C)$$

Despite the differences in composition and keeping in mind that the different grain size of the materials might have influenced their reactivity (decreasing the grain size generally increases the rate of oxidation), it is possible to see (Figure 2.2-4) that the activation energy decreases with the increasing degree of oxidation of the material. According to Fayek and Kyser [58], this can be explained by the differences between the U(VI)-O bond and the U(IV)-O bond. The change in slope of the data between 300 and 400°C is instead taken by Fayek *et al*. [57] as an indication that at temperatures below 400°C interstitial diffusion dominates over vacancy diffusion, since most studies suggest that vacancy migration begins to significantly contribute to oxygen diffusion only at temperatures above 400°C [53, 59]. Nevertheless, this is still a disputed aspect, since it is actually not determined which mechanism controls diffusion at low temperatures. Also, it appears that in comparing both studies, Fayek *et al*. [57] consider both uraninite sample investigated as nearly stoichiometric, while in the first publication [58] the uraninite sample was reported as hyper-stoichiometric. Therefore, the two uraninite curve might not be directly comparable.

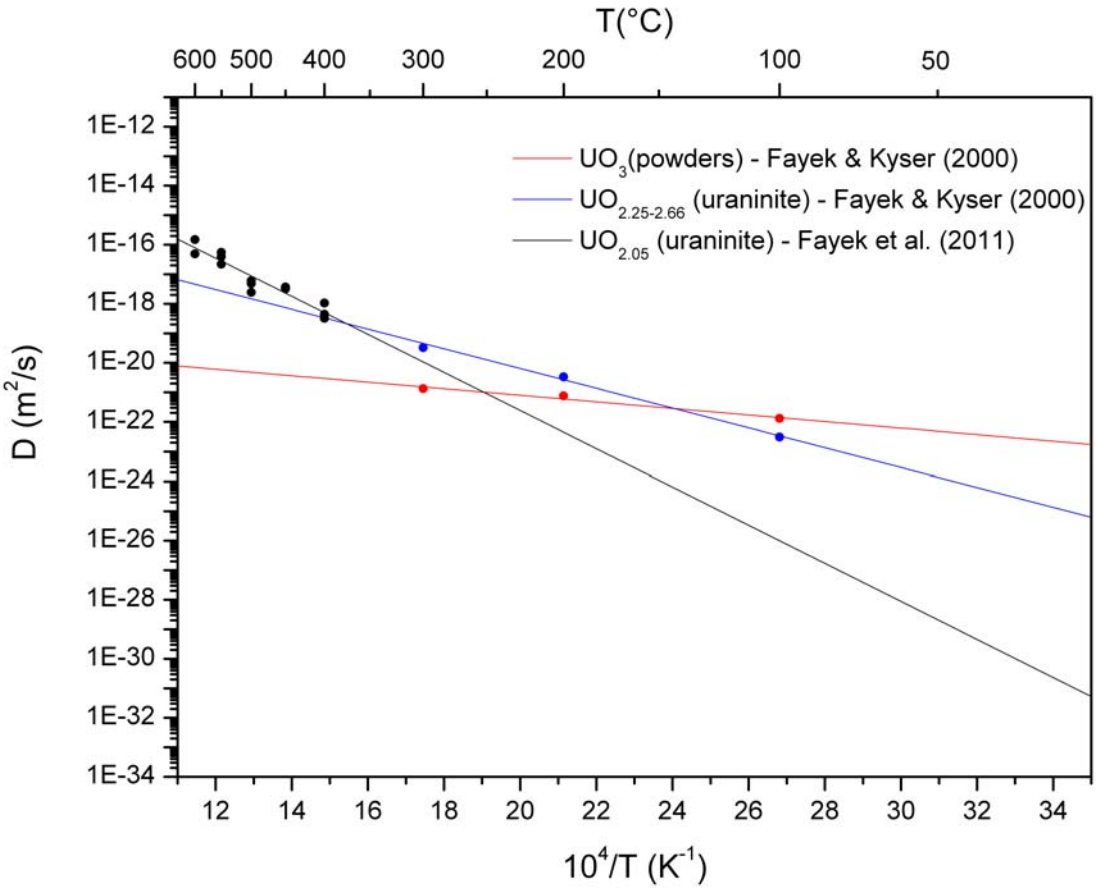

Figure 2.2-4: Oxygen self-diffusion coefficients in UO_2 samples at low temperature: experimental data and fitted curves from Fayek and Kyser [58] and Fayek *et al.* [57].

Oxygen chemical diffusion

The chemical diffusion coefficient can be calculated from the measured oxygen self-diffusion coefficient in UO_{2+x}. Starting from the aforementioned general relation given by Darken [51] (2.2.5-4) applied to the case of UO_2, the chemical diffusion coefficient of oxygen, $\tilde{D}_O$, can be expressed as:

$$\tilde{D}_O = (N_U D_O^* + N_O D_U^*)\frac{d\ln a_O}{d\ln N_O} \qquad \textbf{2.2.5-5}$$

where N_U and N_O are the atomic fraction of U and O, respectively, D_U^* and D_O^* are the self-diffusion coefficients of U and O, respectively, and a_O is the activity of oxygen.

Breitung [53] considers that the self-diffusion of uranium can be neglected, as $D_U^* >> D_O^*$ and that $\ln a_O = \frac{\Delta\overline{G}_{O_2}}{2RT}$. Since $N_U = \frac{1}{3+x}$ and $N_O = \frac{2+x}{3+x}$, it is possible to calculate $dN_O = \frac{dx}{(3+x)^2}$ and therefore:

$$\tilde{D}_O = D_O^*\left(\frac{2+x}{2RT}\right)\left(\frac{d(\Delta G_{O_2})}{dx}\right) \qquad \textbf{2.2.5-6}$$

This relation is similar to the relation previously developed by Lay [60] for UO_{2+x}, but is valid for both hyper and hypo-stoichiometric $UO_{2\pm x}$ [53]. It shows that under a chemical potential the diffusion coefficient is equal to the self-diffusion coefficient D^* multiplied by a thermodynamic factor which contains the change of the oxygen potential with stoichiometry.

The thermodynamic factor can be calculated using models describing the change of oxygen partial pressure as a function of temperature and oxide composition. According to these models, developed using measured $\Delta\overline{G}_{O_2}$ values, for temperatures in the range of 500-2500°C the thermodynamic factor is nearly independent of T. This means that chemical diffusion can be considered to have roughly the same activation energy as self diffusion. The thermodynamic factor determines that $\tilde{D}_O$ can be several orders of magnitude larger than D_O^*. Thus, chemical potential enhances the oxygen diffusion drastically.

Nevertheless, the thermodynamic factor decreases with increasing x, meaning that at larger deviations from stoichiometry the difference between chemical and self-diffusion coefficients becomes less important. Chemical diffusion coefficient, as a consequence, is much less dependent on stoichiometry than the self-diffusion coefficient [53]. For x<0.01, the chemical diffusion coefficient is actually independent of x. For x>0.01, $\tilde{D}_O$ increases slightly with x, up to a factor 3 between x=0.01 and x = 0.16. Nevertheless, for x ≈ 0.25-0.33 the impact of the increase of the ratio O/U seems to cause a decrease of the diffusion coefficient [61].

For chemical diffusion coefficients, there are not as many experimental data published in the literature (some of these are shown in Figure 2.2-5). The comparison between them is complicated by the fact that some datasets are acquired at high-temperature (T>500°C), like those of Lay [53, 60], and others in the range 100-300°C (Aronson *et al*. [29], Walker *et al*. [62]). A further complication, as suggested by Grambow [32], is represented by the fact that different stoichiometries are involved in the different experiments. As a matter of fact, the high temperature experiments were carried out on $UO_{2.16}$ while at lower temperature the stoichiometry taken into account was generally U_3O_7 (with x = 2.30 - 2.36).

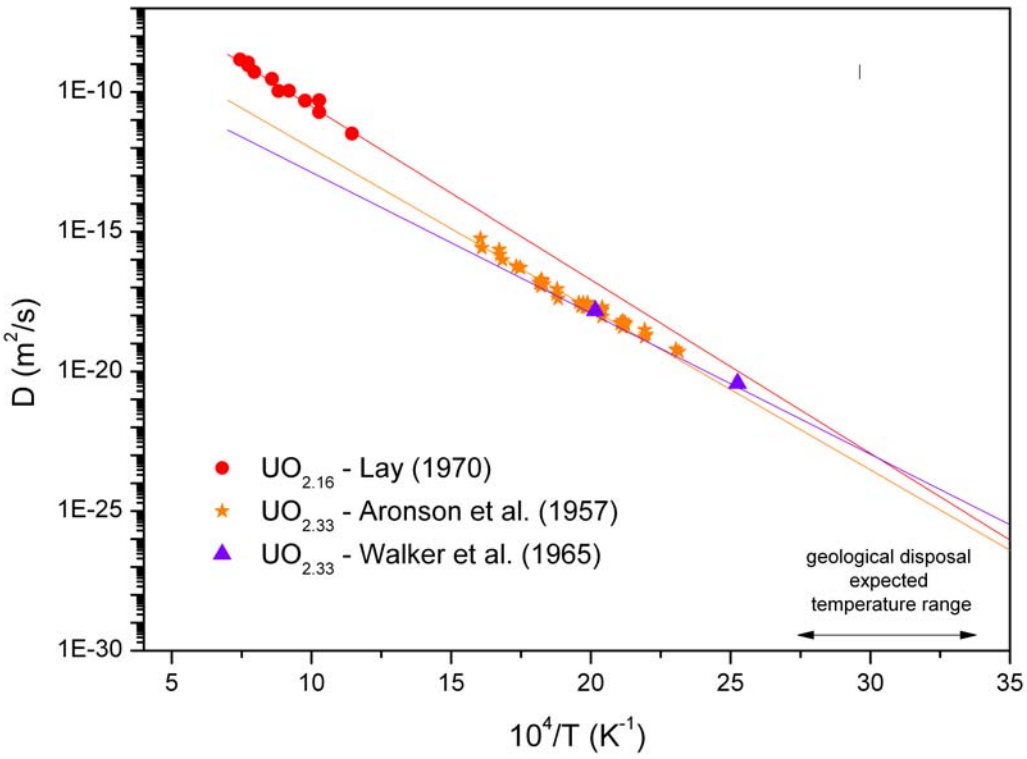

Figure 2.2-5: Oxygen chemical diffusion coefficients in UO_{2+x}: experimental data and fits from Lay [60], Aronson *et al.* [29] and Walker *et al.* [62].

Grambow [32] predicted that the chemical diffusion coefficient of oxygen in UO_2 at 25°C should be in the range 10^{-23} - 10^{-25} m^2/s. The upper limit was estimated from the extrapolation of high-temperature data and the lower limit from the low-temperature ones Figure 2.2-5.

Poulesquen *et al*. [30] suggested the use of two different oxygen diffusion coefficients for the phases U_4O_9 (x = 0.22 - 0.25) and U_3O_7 (x = 0.32 - 0.33), at temperatures below 300°C.

$$\tilde{D}_{U_4O_9}\left[m^2/s\right] = 1.36 \cdot 10^{-9} \exp\left(\frac{-57000}{RT}\right)$$

$$\tilde{D}_{U_3O_7}\left[m^2/s\right] = 1.16 \cdot 10^{-3} \exp\left(\frac{-123000}{RT}\right)$$

The two Arrhenius-type equations for the oxygen diffusion coefficients were obtained by fitting published experimental weight-gain curves (evolution of the O/U ratio as a function of time for different temperatures) recorded during oxidation of UO_2 powders according to a grain oxidation model in which only the two phases U_4O_9 and U_3O_7

were considered. Despite the simplification of the model (that did not include for example the formation of U_3O_8) the oxygen diffusion coefficients provided a good fit of the experimental data and were used to calculate the Arrhenius-type equations (Figure 2.2-6).

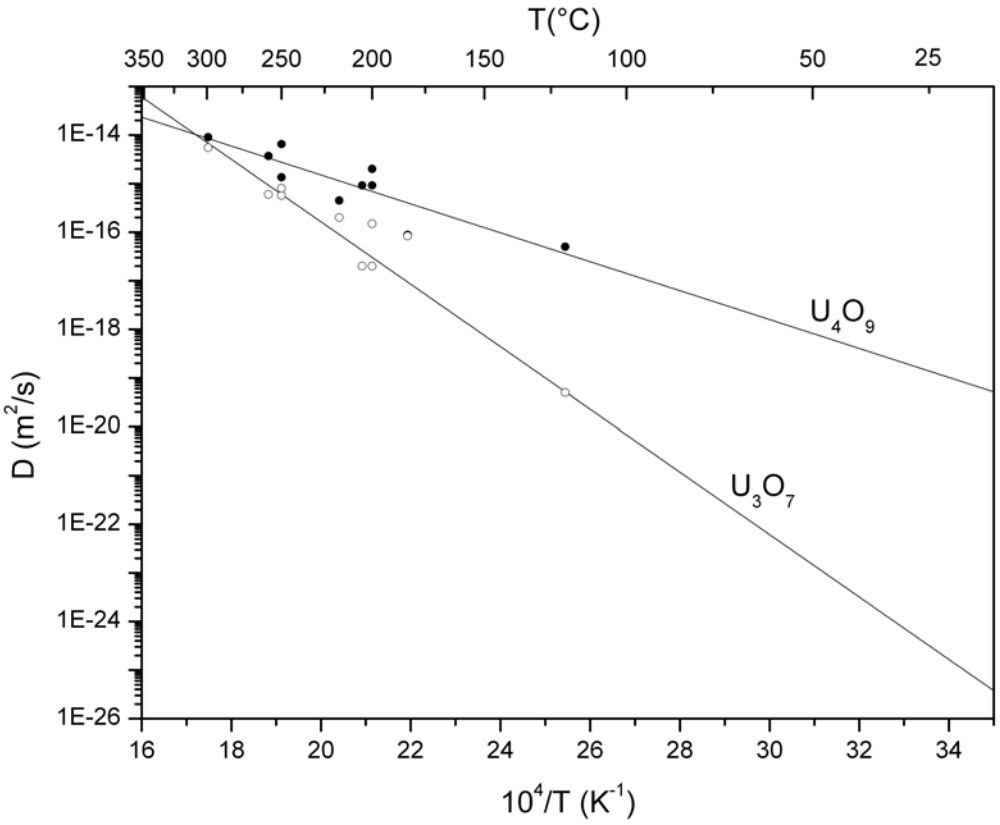

Figure 2.2-6: Oxygen diffusion coefficients in U_4O_9 and U_3O_7: Arrhenius-law fit from Poulesquen *et al.* [30] and extrapolation to temperatures relevant for the geological disposal).

The two activation energies calculated in this way for U_4O_9 (57 kJ/mol) and U_3O_7 (123 kJ/mol) are in good agreement with literature data. As a matter of fact, an average value of 90 KJ/mol can be obtained from the estimates of the activation energy for the formation of U_3O_7 / U_4O_9 from UO_2 powder (95.7 kJ/mol), sintered UO_2 pellets (98.6 kJ/mol) and irradiated fuel (106 kJ/mol) [45]. It is interesting to note how the two curves intersect at T = 573 K (Figure 2.2-6). This could explain why in experiments carried out above this temperature it was not possible to distinguish between the two phases [30].

Grain-boundary diffusion

Vacancies and interstitials are not the only defects which promote diffusion in solids. Grain boundaries, dislocations and free surfaces are also playing an important part and are presumed to behave like high-diffusivity paths in most materials. Preferential diffusion along dislocations has been observed both in metals and in ceramic materials since the early fifties [63]. It is well established that the frequency with which atoms move from different positions within the crystal lattice (mean jump frequency) is higher at dislocations, boundaries and surfaces than it is for the same

atom in internal positions of the lattice [23, 64]. Therefore, the diffusivity is higher in these regions. Another possible reason is that there is a higher concentration of defects in the boundary than in the lattice. It is also possible that the reason lies in a combination of these two effects.

Measurements of diffusion coefficients in grain boundaries are scarce and complicated by the difficulties to assess grain boundary morphology. Very often in diffusion experiments in polycrystalline bodies the measured quantity is in reality an apparent or effective diffusion coefficient containing both lattice and boundary diffusion terms. Measurements of the effective diffusion coefficient, D_{eff}, are obtained from experiments in both polycrystalline and single-crystal materials, by plotting the logarithm of the tracer concentration (often a radioactive isotope of a matrix element) vs. the squared penetration distance.

Studies have shown identical values of D_{eff} in single-crystal and polycrystals at temperatures higher than the 6/10 of the melting point of the material, which for UO_2 would be ≈ 1700°C. The reason is that above this temperature the difference between the jump frequency in the grain boundaries and the one in the lattice is smaller. At lower temperatures, instead, diffusion in polycrystalline materials is found to be consistently faster than in single-crystals [23].

An early idealization of grain boundary diffusion was provided by Fisher [65], who considered the grain boundary to be a thin layer of high-diffusivity material between two grains characterised by low bulk (*i.e.*, lattice) diffusivity. As shown in Figure 2.2-7, the grains on either side are considered regular in shape (semi-infinite parallelepipeds) and large compared with the width of the grain boundary, δ, and with the distance, λ, over which the solute diffuses within the lattice during a certain time, t. Denoting by y the coordinate perpendicular to the grain boundary, and by D_B and D_L the diffusion coefficient along the grain boundary and the grain lattice, respectively, the diffusant concentration, $\xi(x,y,t)$, obeys the differential equation:

$$\frac{\partial \xi}{\partial t} = D_B \frac{\partial^2 \xi}{\partial x^2} + \frac{2D_L}{\delta} \cdot \left.\frac{\partial \xi}{\partial y}\right|_{y=\delta/2} \qquad \textbf{2.2.5-7}$$

in the boundary slab, and Fick´s second law (Equation 2.2.5-2) outside the grain boundary. It should be noted that the system is invariant in the z direction orthogonal to x and y. Therefore the mean value of $\xi(x,y,t)$ over a distance $y = 2L$ centred about the grain boundary, indicated by $c(x,t)$, can be expressed as:

$$c(x,t) \equiv \frac{1}{2L} \int_L^{+L} \xi(x,y,t)\,dy \qquad \textbf{2.2.5-8}$$

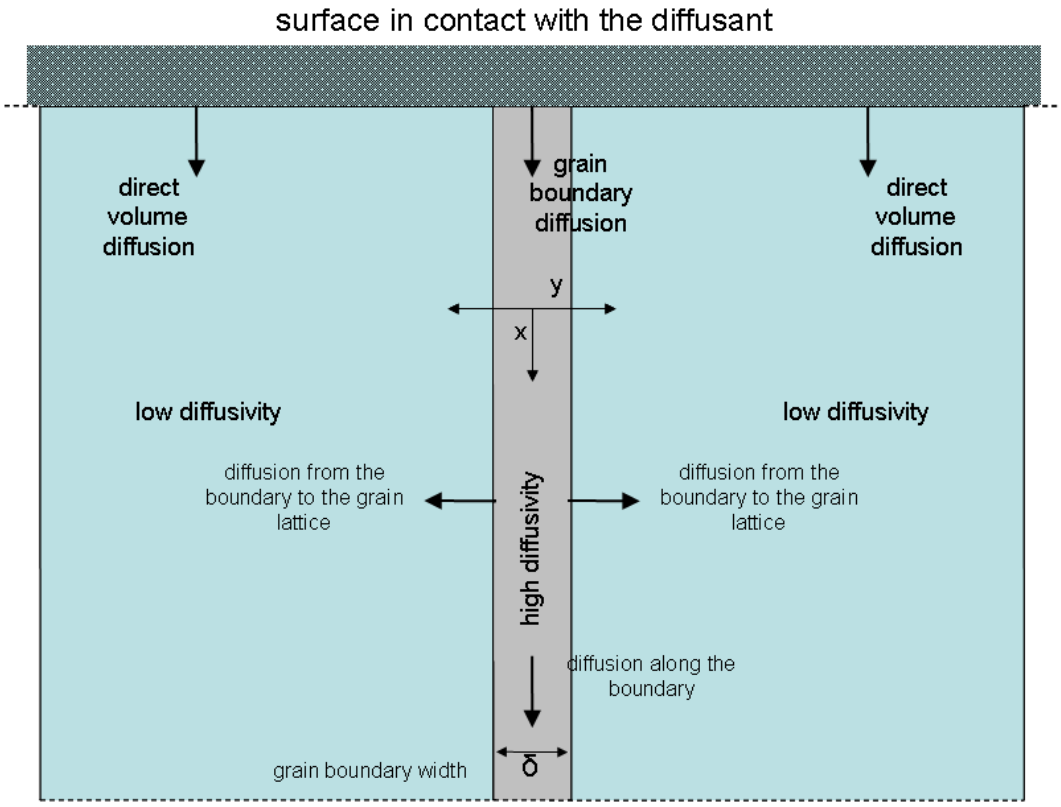

Figure 2.2-7: Fisher's grain boundary diffusion model: schematics and coordinate system for diffusion in a semi-infinite slab of high diffusivity material (of width δ) embedded in a semi-infinite solid, as proposed by Fisher [65].

This can be extended to the infinite limits as in:

$$c(x,t) \approx \frac{1}{2L} \int_{-\infty}^{+\infty} \xi(x,y,t)\,dy \qquad \textbf{2.2.5-9}$$

for values of L of the order of or higher than the lattice diffusion length λ ($\lambda = 2\sqrt{Dt}$). Making use of Equation 2.2.5-9, Fisher´s main finding can be rewritten as:

$$c(x,t) \propto \sqrt{t}\,\exp[\ \alpha_F(t)\,x] \qquad \textbf{2.2.5-10}$$

where $\alpha_F(t)$ is a factor depending on the quantities δ and D_L. This result was derived under the boundary conditions that the diffusant concentration is held constant at the surface of the material and that $\xi(x,y,t)$ is continuous at the grain - grain boundary interface, as well as under a number of approximations [65].

The first exact solution of the coupled differential equations 2.2.5-7 and 2.2.5-2 is due to Whipple [66]. He also assumed the above-mentioned boundary conditions,

and used a Fourier-Laplace transform to obtain a solution in integral form. Furthermore, Whipple showed that an asymptotic approximation for $c(x,t)$ at large penetration depths is given by

$$c(x,t) \sim \exp\left[\alpha_W (t)\, x^{4/3} \right] \qquad \textbf{2.2.5-11}$$

where α_W is a time-dependent factor analogue to α_F .

Levine and MacCallum [67] generalized the Fisher-Whipple model to include diffusion from the specimen surface through the grains and diffusion around the grains through the boundaries. Their numerical analysis indicated that beneath a surface layer where $d\ln c/d\left(x^2\right)$ is constant due to direct lattice diffusion, there is a region where the slope $\alpha_{L-M} \equiv -d\ln c/d\left(x^{6/5}\right)$ is constant, and the quantity δD_B can be obtained from the following equation [23]:

$$\delta D_B = 1.946 \left(\frac{D_L}{t} \right)^{1/2} \alpha_L^{\,5/3}{}_M \qquad \textbf{2.2.5-12}$$

Although Fisher´s and Whipple´s solutions have also been widely used for interpretation of experimental concentration-depth curves, Levine and MacCallum´s approach is regarded as the most appropriate for polycrystalline solids [68].

Grain boundary dimensions

A diffusion coefficient in grain boundaries is usually very difficult to assess because the grain boundary width is generally unknown or very difficult to measure. Therefore only the product δD_B is obtained from typical diffusion measurements. From an experimental point of view, diffusion along a grain boundary appears to be proportional to the grain boundary width, δ, but the diffusion coefficient along the grain boundary, D_B is then difficult to calculate as long as a reliable measurement of δ is obtained.

It has been assumed that the grain-boundary width is of the order of 0.1 nm in metals. Direct observation of grain boundaries by means of field ion emission tips has shown that this estimate is roughly correct. However, the definition of grain boundary itself is actually not straightforward and many authors have rather discussed grain boundary as a wider region, including not only the area of misfit between the crystals but also the space-charge region on either side [64, 69]. For this reason, Mistler and Coble [64] presented a method to calculate the effective grain-boundary width from measurements of D_{eff}, which can be expressed according to relationship proposed by Harrison [63]: $D_{eff} = f(D_B) + (1-f)D_L$. The fractional volume for grain boundary diffusion, f, is the ratio between the volume of the grain boundary and the volume of the grain. Therefore, f is a function of δ, according to specific crystal geometry. The so-obtained calculations by Mistler and Coble [64] show how, in a very pure metal, the effective boundary width δ_{eff} will in all probability include only the region of misfit, while in a ionic material the space-charge layer may extend quite deep into the lattice, in both

pure and impure materials. As a result, in materials with ionic bonding the calculated widths are much larger than the assumed three atomic diameters width, which is an approximation valid for metals. For ceramic materials like UO_2 it has been calculated that a good estimation of the grain boundary width is ≈ 1 nm [70].

Table 2.2-1: Examples of calculated effective grain boundary width for ceramic materials.

ceramic	*Temperature (°C)*	*Grain-boundary diffusion coefficient (m^2/s)*	*Effective grain-boundary width* (nm)*
Al_2O_3	1650	$4.55\ 10^{-14}$	12
	1750	$1.61\ 10^{-13}$	14
	1800	$3.6\ 10^{-13}$	11
	1900	$1.98\ 10^{-12}$	7
NaCl	700	$2.1\ 10^{-12}$	910
MgO	1400	$3.73\ 10^{-11}$	2270
	1450	$2.74\ 10^{-11}$	2850
BeO	1600	$4.21\ 10^{-13}$	30
	1710	$1.81\ 10^{-12}$	14

* Calculations by Mistler and Coble [64].

Grain-boundary diffusivity in UO_2 and spent fuel

In spent fuel, penetration of oxygen into grain boundaries is known to be much faster than into the grain matrix and grain boundary oxidation is also described as a diffusion process [32, 43]. Weight-gain curves obtained by Einziger and Woodley [71, 72] from oxidation of PWR fuel with ≈ 3% burn-up could be used to obtain an estimation of the diffusion coefficient of oxygen in grain boundaries at 200°C, considered within a factor two of uncertainty [32]:

$D_B\,(200°C) = 1.4 \cdot 10^{-13}\ m^2/s$

According to Woodley [43], the activation energy of grain boundary oxidation is similar to that of matrix oxidation, *i.e.* 104 kJ/mol: considering this value, an estimation of the grain boundary diffusion coefficient at 25°C would be:

$D_B\,(25°C) = 2.3 \cdot 10^{-20}\ m^2/s$

Grambow [32] speculates that within the uncertainty of the data the dependence of the calculated diffusion coefficient on the transport mechanism can be neglected. Comparing such values with the oxygen diffusion coefficient in UO_2 matrix at 200°C, it is found that diffusion in the grain boundaries is 4 - 5 orders of magnitude faster than bulk diffusion. Nevertheless, it would take 800 years for oxygen to penetrate in the fuel for a distance equal to a grain diameter (25 μm in the case under analysis). Therefore, grain boundaries oxidation should be an extremely slow process at room temperature and almost impossible to be observed. It is important to consider that Grambow's estimation is highly speculative, since it depends strictly on the activation energy considered for the extrapolation which in turns is a difficult aspect to estimate, as it has been discussed in the previous paragraph.

Most studies of oxygen diffusion in minerals show that grain boundary diffusion is much faster than volume diffusion [73]. Nevertheless, a number of authors have reported that their measured diffusivities in polycrystalline UO_2 are approximately equal to those in a single crystal and that oxygen diffusion in uraninite depends mostly on temperature and stoichiometry rather than on grain boundary diffusion [54, 74].

Fayek *et al*. [57] speculate that the single crystals used in those studies of oxygen diffusion in uraninite were not single crystals or that the methods used to separate volume versus grain boundary diffusion were inadequate. In fact, Fayek *et al*.[57] reported that their experimental findings showed evidence of two diffusion mechanisms: an initial, extremely fast mechanism that overprinted the oxygen isotopic composition of the entire crystals regardless of temperature and may reflect diffusion along sub-grain boundaries and micro-fractures (e.g., fast-path diffusion); and a slower volume-diffusive mechanism in which oxygen may have moved through defect clusters that displace or eject nearest-neighbour oxygen atoms to form two interstitial sites and two partial vacancies, and by vacancy migration.

2.2.6 Oxidative dissolution of UO_2

UO_2 has a very low solubility in water, as in the perfect fluorite structure many bonds have to be broken in order to bring an atom of U into solution. This process is however favoured by the fact that U(IV) atoms are easily coordinated by water molecules. Due to the strong hydrolysis of U(IV), hydroxo complexes are formed in solution. In pure water at pH>5 every U(IV) atom is coordinated by four OH- groups. The dissolution can then be described by the reaction:

$$UO_{2(s)} + 2H_2O \rightarrow U(OH)_{4(aq)}$$

The experimental determination of the solubility of UO_2 is affected by many issues, arising from sorption, removal of fine particles, sensitivity of the analytical method and above all the difficult characterisation of the solid surface and of the degree of crystallinity [75]. The theoretical solubility of crystalline and "amorphous" UO_2 has been calculated for different pHs from thermodynamical data, but the term hydrous or amorphous UO_2 used in the literature do not refer to a unique material, rather to a range of solids with different thermodynamic stability. As a result, the experimental values published over the years have displayed some inconsistency [75]. At pH > 5 solubility is actually insensitive of pH and $U(OH)_4$ is the only species present in solution. At pH=7-9, as expected for groundwater in a repository, the theoretical solubility of the "amorphous" solid is $10^{-8.5}$ M, while for the crystalline solid it has been calculated to be as low as 10^{-15} M [75, 76].

Since the UO_2 solubility is so low, the dissolution rate of spent fuel will then be controlled by the diffusive transport of U away from the fuel, which is a process so slow that the practical fuel dissolution becomes negligible [11]. However, this ideal scenario is complicated by the presence of oxidants. In fact, oxidation is in reality the main route of fuel dissolution, leading to the formation of the significantly more

soluble U(VI) species. The oxidative dissolution process, for which UO_2 is converted into the more soluble UO_2^{2+}, must be considered a corrosion process.

This process will necessarily be determined by the redox potential of the groundwater. If this is more positive than the equilibrium potential for fuel dissolution, *i.e.* the potential of the couple UO_2 /UO_2^{2+}, a corrosion potential will be established.

$UO_2 + Ox \rightarrow UO_2^{(2+)} + Red$

The corrosion potential (E_{corr}) can be defined as the difference between the potential of the two half-reactions and the corrosion rate will be controlled by the kinetics of the slowest one. At pH=8.5, the highest potential $E_{Red/ox}$ at which UO_2 can be considered immune from corrosion is -50mV (SHE) [11].

Groundwater at repository depths is oxygen-free, and any oxygen introduced during repository construction and operation prior to its sealing will be rapidly consumed [11]. Oxidising conditions might however be created at the fuel surface as a result of the fuel's radioactive decay, which leads to water radiolysis. Figure 2.2-8 shows some of the reactions involved in the radiolysis of water. A system of nearly 80 elementary reactions describe the radiolytic process in which all the species (radicals, ions and water molecules) react with each other [77]. The overall result of the radiolysis is the formation of new molecular species: H_2O_2, O_2, and H_2. Even though equimolar amounts of reducing and oxidising species are created, due to the higher activity of the latter, an oxidative environment is expected to result from this process [78].

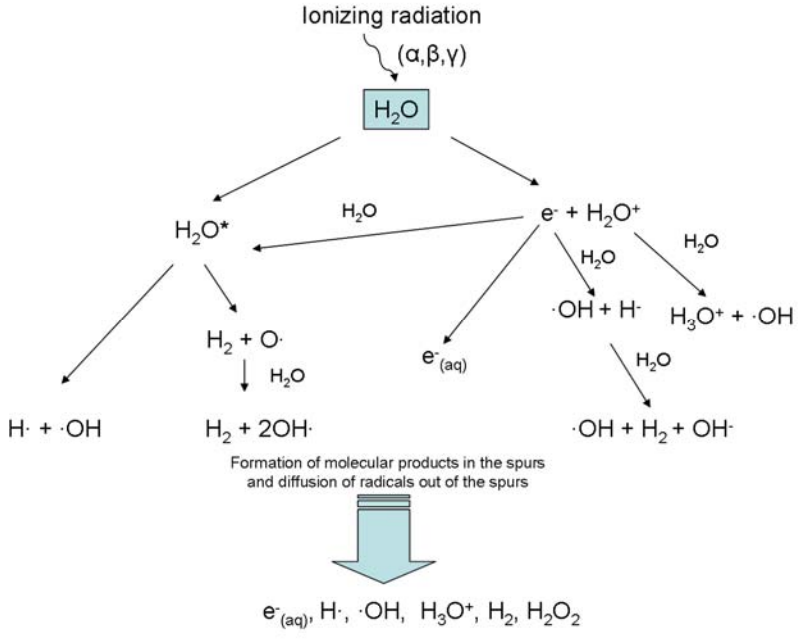

Figure 2.2-8: Radiolysis of water: simplified scheme of the main reactions involved, as proposed by Choppin [6].

Also the type of emitted radiation (α,β,γ) has consequence on the radiolytic process and the kind of species produced. After 300-500 years in the repository, most of the

β(γ)-emitters have decayed and α-radiation will dominate the situation and will remain significant for more than 10^5 yr [79]. At the time when canister failure is most likely to happen, then, α-radiolysis is the main process expected to take place. Due to the larger size of the alpha-particles, this process is characterised by a higher chance of combination reactions between radicals, if compared with β- and γ-radiolysis. For these reasons the main molecular species produced by alpha-radiolysis are H_2O_2 and H_2 [6].

As the radiation fields associated with spent fuel will decrease with time, the radiolytic oxidant concentration will also decrease, with the consequence of a lower $E_{Red/ox}$, which in turns will determine a lower E_{corr}. Also the corrosion rate decreases, as the rate of replenishment of the oxidant concentration.

The presence and amounts of oxidant species is not the only aspect to be considered: other chemical compounds present in groundwater can play a role. If enough oxidants are available near the fuel surface, the solubility of U(VI) phase will be exceeded and a secondary uranium phase will precipitate. The environment expected to prevail in most nuclear waste disposals is near-neutral to alkaline and in the range pH=6-8 the solubility of the corrosion product $UO_3 \cdot 2H_2O$ is at a minimum [75]. This secondary phase is believed to suppress the corrosion of the surface as it functions as an insulator that blocks the access to the active sites, which are the surface atoms in the higher oxidation states, namely U(VI) and U(V). U(V) exists only as an intermediate in the overall oxidative dissolution process, normally leading to a mixed U(V)/U(VI) surface layer [80]. The U(VI) concentration at which the secondary phase starts to form depends on the composition of groundwater. The main groundwater constituents that are known to affect, with pH, the formation of the U(VI)-precipitate are carbonate, calcium and silicate [78].

Of all the potential groundwater species, the one most likely to enhance UO_2 dissolution under the natural pH conditions expected in a repository is carbonate ion, a strong complexing agent for the UO_2^{2+} ion [81].

$$UO_2^{2+} + CO_3^{2-} \rightarrow UO_2CO_{3\,(aq)} \qquad \log K_1 = 9.5 \pm 0.4$$

$$UO_2^{2+} + 2CO_3^{2-} \rightarrow UO_2(CO_3)_2^{2-} \qquad \log \beta_2 = 16.6 \pm 0.3$$

$$UO_2^{2+} + 3CO_3^{2-} \rightarrow UO_2(CO_3)_3^{4-} \qquad \log \beta_3 = 21.6 \pm 0.6$$

The transfer of oxidised U species to solution is in this case sufficiently accelerated by complexation with carbonate that the incorporation of O^{2-} into a stable oxidised surface layer does not occur. This prevents the accumulation of corrosion products ($UO_3 \cdot 2H_2O$) which would restrict the diffusion of dissolved UO_2^{2+} away from the surface [11]. At HCO_3^-/CO_3^{2-} total concentrations ≥ 10^{-3} M, as predicted in some groundwater conditions, oxidative dissolution proceeds then 2-3 times faster. At concentrations below 10^{-4} M the influence of carbonates on kinetics becomes negligible. It has been suggested that the presence of HCO_3^- is kinetically involved in the mechanism, by complexing and stabilizing the U(V) sites on the surface, created as an intermediate step towards U(VI) [78, 82]. However, while the presence and

importance of surface U(V) complexes has been proven, little evidence of any specific role played by bicarbonate ions can be found [80, 83].

The influence of carbonate can be categorized as a function of concentration, as reflected in the schematics of Figure 2.2-9 [78]. In the absence of carbonate, corrosion product deposits can accumulate and suppress dissolution (a); at low concentrations (<10^{-3} M) the predominant influence of carbonate seems to be the thermodynamic ability to increase UO_2 solubility and, hence, to prevent the deposition of corrosion product deposits (b); for intermediate concentrations (10^{-3} to 10^{-1} M), carbonate is kinetically involved, via the formation of surface intermediates, in the dissolution process (c); for high concentrations, the presence on the surface of a phase such as UO_2CO_3 begins to limit the rate of dissolution and the reaction becomes much less dependent on carbonate concentration (d). The effect of carbonate also decreases if conditions become less oxidising.

On the other hand, the presence of calcium and silicates has been shown to reduce the corrosion rate of UO_2 [84, 85]. Even though these species do not prevent the surface oxidation, they both interfere with the dissolution of U(VI). Ca^{2+} absorbs onto the surface and blocks the protonation steps involved in the dissolution. SiO_4^{4-} also suppresses the dissolution by creating a nearly insoluble hydrated U(VI) silicate deposit on the surface [11]. The effect of CO_3^- in groundwater will dominate over the effect of Ca^{2+} and SiO_4^{4-} thus, the formation of a silicate precipitate on fuel surface is unlikely in a repository [78].

To describe the UO_2 surface oxidation as a function of the corrosion potential, four cases can be identified [78].

1) -560 mV ≤ E_h ≤ -160 mV (SHE): oxidation of sub-monolayer quantities of surface material occurs, mostly concentrated in grain boundaries.

2) -160 mV ≤ E_h ≤ 140 mV (SHE): oxidation of the UO_2 lattice to UO_{2+x} occurs with both x and the depth of oxidation increasing with potential to a limiting composition of ≈ $UO_{2.33}$ /$UO_{2.4}$ at 140 mV. Dissolution as UO_2^{2+} begins at -60 mV (in neutral to slightly alkaline solution).

3) 140 mV ≤ E_h ≤ 540 mV (SHE): oxidation, dissolution and the accumulation of corrosion product deposits occur. The balance between dissolution and the formation of corrosion product deposits varies with pH and solution composition. For pH ≤ 5, corrosion product deposition no longer occurs, oxidation to $UO_{2.33}$ is prevented, and, hence dissolution accelerated. In non-complexing neutral solutions, corrosion product deposits accumulate and block fuel dissolution. In neutral solutions containing sufficient HCO_3^-/CO_3^{2-} (≥ 10^{-3} M), $UO_{2.33}$ does not form, corrosion product deposits are avoided and dissolution is accelerated. In Ca/Si-containing groundwater the formation of protective corrosion product deposits is reinforced.

4) E_h > 540 mV (SHE): rapid dissolution leads to the development of local acidity causing grain boundary etching and pitting. The dissolution rate increases since corrosion product deposition is prevented.

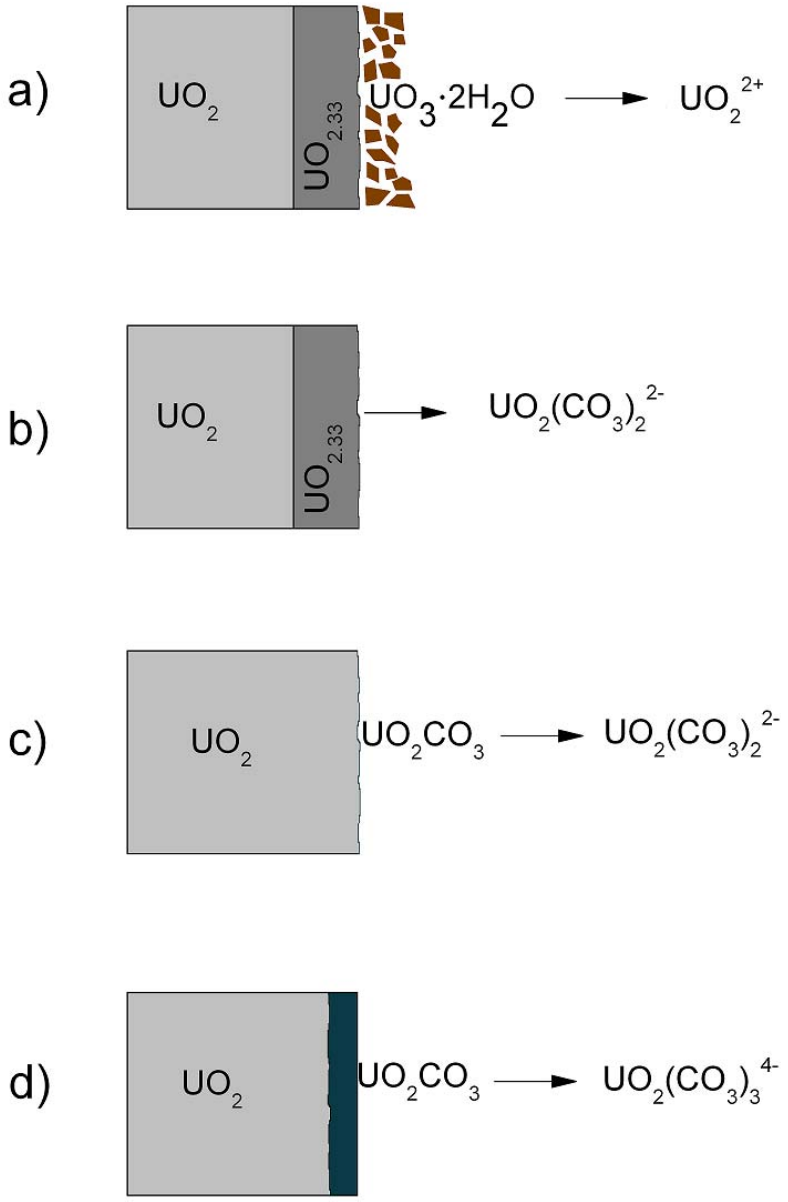

Figure 2.2-9: Influence of carbonate on UO_2 dissolution in four cases: a) no carbonate; b) low carbonate concentration ($<10^{-3}$ M); c) intermediate concentration (between 10^{-3} and 10^{-1} M); d) high carbonate concentration ($>10^{-1}$ M). Scheme according to Shoesmith [78].

Another factor to be taken into account, in case of contact with groundwater, is the corrosion of the canister iron. By the time the canister fails, all the residual oxygen trapped in the repository will have been consumed by bacteria and reducing minerals [86] and, as a consequence, the deep groundwater is anoxic. Under these conditions, the corrosion of the cast iron canister will be an anaerobic process and will proceed through the reaction:

$Fe + 2H_2O \leftrightarrow Fe(OH)_2 + H_2\uparrow$

$3Fe + 4H_2O \leftrightarrow Fe_3O_4 + 4H_2\uparrow$

with the consequence of the production of Fe^{2+}/Fe^{3+} oxides and hydrogen gas [87, 88]. Both Fe^{2+} and H_2 are reducing species and can influence the fuel corrosion behaviour by interacting with the radiolytic oxidants or with the corrosion products. Nevertheless, Fe^{2+} alone does not hinder the oxidation of the fuel surface; it only enters into a competition for the oxidants [89]. On the other hand, dissolved H_2 has been shown to block the oxidative corrosion of UO_2 [90].

Metallic inclusions of Mo, Tc, Pd, Ru and Rh in the fuel, the so-called ε-particles, are known to have a catalytic effect on H_2 reactions, reducing further the dissolution rates of UO_2 [88]. However, the amount of ε-particles at the fuel surface is relatively small and their long-term catalytic effect is questioned due to possible coverage of the fuel surface by re-precipitation of reduced UO_2. Consequently, the reactions of pure UO_2 with oxidants and hydrogen will ultimately govern the release of radionuclides.

Carbol *et al*. [88] proposed a surface-catalysed reaction, taking place in the H_2-UO_2-H_2O system, where molecular hydrogen is able to reduce oxidants originating from α-radiolysis, resulting in the suppression of the UO_2 dissolution. The mechanism suggested begins with the production of a U(IV) - U(V) site by reaction of UO_2 with radical oxidants or H_2O_2, as for Shoesmith [11], and then proceeds with the adsorption of H_2 at the U(V) site, promoting the transfer of an electron to the surface. This process is likely to happen also for the adsorption of O_2, which would be then followed by the inverse electron transfer causing oxidation. Provided that the amount of dissolved H_2 is in large excess, an inverse reaction will always occur before the next oxidant brings the U(V) to U(VI). Since the U(IV) - U(V) sites will disappear if the surface becomes too oxidised, a requirement for the catalytic decomposition of oxidants is that the surface is close to stoichiometric.

3 Experimental

3.1 Materials

3.1.1 Single-crystal UO_2

So-called single-crystal UO_2 samples were obtained from material available at ITU (batch E1047/1941) and belonging to a large batch of depleted UO_2 (0.4 wt. % ^{235}U). This material was the result of an experiment carried out in 1987 at the JRC-Ispra FARO plant, a large test facility in which reactor severe accidents could be simulated by out-of-pile experiments [91]. Quantities up to 200 kg of oxide fuel type melts (up to 3000°C) could be produced in the FARO furnace, possibly mixed with metallic components, and then delivered to a test section containing a water pool, in order to investigate basic phenomenology relevant to the fragmentation and quenching of molten material into the water coolant at different initial pressure and water subcooling. As a result of one of these experiments, roughly 100 kg of molten UO_2 was crystallized in the quenching, producing, in the part of the mass that had a slower cooling, larger portion of mono-crystals.

The fragments produced of the original molten had variable dimensions in the orders of a few centimetres. One of these fragments was cut to produce several 1-2 mm thick slices. After polishing, the presence of mechanical cracks or fractures running throughout the entire sample surface was visible (Figure 3.1-1). The fragment was constituted by a cluster of macrocrystals with different dimensions in the range 0.3-10 mm.

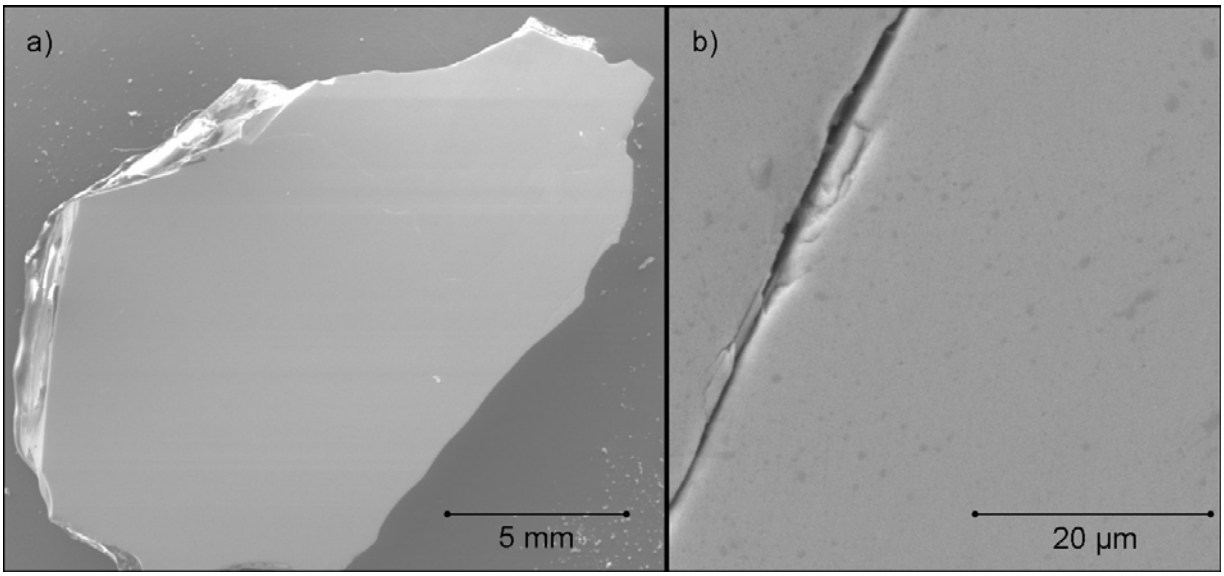

Figure 3.1-1: Single-crystal UO_2 sample: a) overview of a single-crystal UO_2 slice after polishing; b) magnification of the fracture dividing the slice into macro-crystals.

X-ray Diffraction (XRD) confirmed the "monocrystalline" nature of the specimen because only one peak is obviously dominating the diffractogram (Figure 3.1-2). Even after the slice broke into two halves along one of the cracks, independent XRD

measurements over the two fragments showed again the same predominant crystallographic orientation. For this reason, and for the sake of simplicity, in the present work samples obtained from this material are referred to as "single-crystal UO_2".

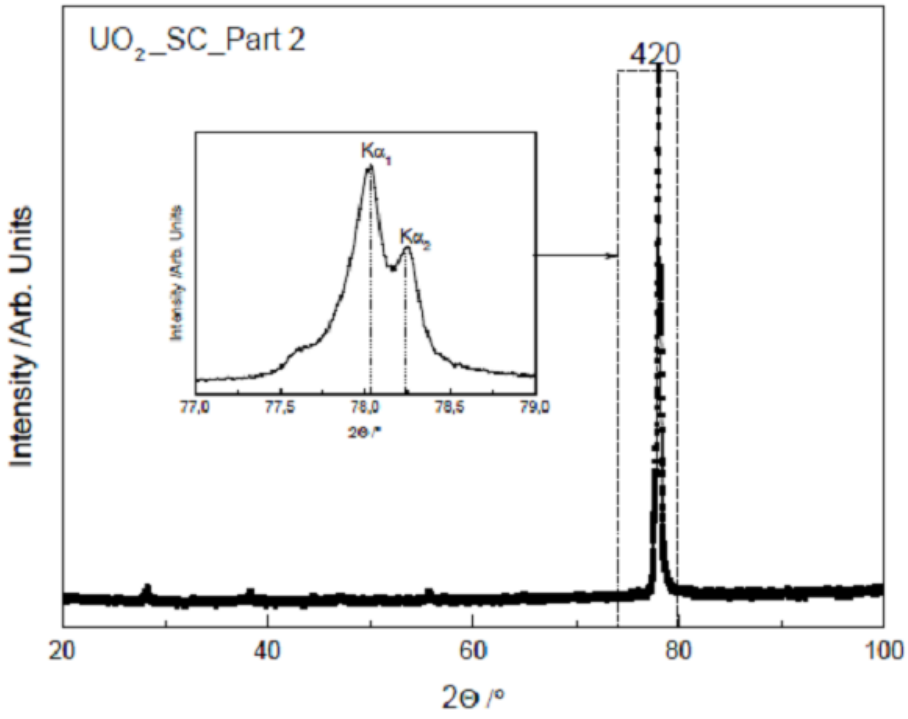

Figure 3.1-2: XRD analysis of so-called single-crystal UO_2 sample: the crystallographic orientation resulting from the cut is homogeneous throughout the complete slice, despite the presence of cracks (X-ray source Cu Kα).

3.1.2 Polycrystalline UO_2

A commercial natural UO_2 pellet (batch E1592/2787, Siemens AG, 0.72 wt% ^{235}U, diameter 8 mm) was cut to obtain slices with parallel faces and with thickness 1 mm. Grain size distribution has been measured on a set of SEM images resulting in a mean value of 9.4 µm. The density of the UO_2 pellets has been measured by Archimedes' method resulting in a value of 96% of the theoretical density [22].

3.1.3 SIMFUEL 8%

SIMFUEL is a chemical analogue of irradiated UO_2. SIMFUEL is a trade name for a product fabricated at the Atomic Energy of Canada Limited (AECL) Research, Chalk River, that was jointly designed in collaboration with ITU, which has been under study since 1962 [92, 93]. SIMFUEL replicates the chemical nature of irradiated fuel, with non-radioactive elements representing fission products and actinides, dry-mixed with

UO_2 powder in amounts equivalent to certain burn-up. A uniformly fine dispersion is achieved on a sub-micrometre scale. Afterwards, the material is compacted, pressed and sintered (2 h at 1700°C in flowing H_2) providing atomic scale mixing and producing a structure similar to that of a fuel that has operated at high temperature. SIMFUEL reproduces and contain three out of four classes of fission products present in spent fuel (as described in Paragraph 2.1.2): dissolved oxides, metallic (Mo-Ru-Pd-Rh) and oxide (perovskite-type) precipitates. The fourth class, represented by the rare gases and volatile fission products is not reproduced. From the morphological point of view, the absence of gas bubbles and the lack of cracks and fission damages make SIMFUEL a simpler matrix than actual spent fuel.

Samples of SIMFUEL were obtained from material available at ITU (batch E1410/2495) and reproducing a burn-up of 8% (≈ 75 GWd/tHM). The same material had been previously characterised [92]. As shown in Table 3.1-1, the concentration of the dissolved oxides reproduces the amount of fission products associated with different burn-up. It is important to notice that the amounts of some elements were increased to substitute for other fission products or actinides: the amount of Ru includes that of Tc, Ce includes that of Np, Sr includes Cs, La includes Am and Cm, Nd includes Pr, Pm, Sm, Eu and Gd; finally, Pu is replaced by U.

Table 3.1-1: SIMFUEL dissolved oxide composition.

Oxide	*Amount (wt%)**		
	3 at.%	*6 at.%*	*8 at.%*
UO_2	97.449	94.866	92.990
ZrO_2	0.336	0.593	0.777
MoO_3	0.356	0.720	0.980
PdO	0.147	0.434	0.652
$BaCO_3$	0.150	0.307	0.433
Y_2O_3	0.040	0.060	0.075
SrO	0.223	0.406	0.531
CeO_2	0.304	0.545	0.717
La_2O_3	0.113	0.254	0.367
RuO_2	0.360	0.754	1.026
Rh_2O_3	0.028	0.034	0.038
Nd_2O_3	0.494	1.027	1.418

*as given by Rondinella et al. [92]

3.2 Sample preparation

3.2.1 Cutting and polishing

All the different UO_2 materials were cut to obtain 1 mm-thick slices with parallel faces. Each slice was cleaned with acetone with the help of a sonic bath. One face was polished in three steps with decreasing grit size (30μm, 15μm, 0.25μm) and finally cleaned with isopropanol.

3.2.2 Annealing

To ensure that the UO_2 samples were perfectly stoichiometric, just before the start of the corrosion experiment, all the different samples were annealed in oven for 6 h at 1700 K, in a gas mix constituted by 96 vol.% Ar and 4 vol.% H_2 in volume, with a flow of 1 L/min.

3.2.3 Thermogravimetry

Thermogravimetry (TG) is based on the continuous recording of the weight change of a solid material, as a function of temperature and time. The sample, typically ranging from 1mg to 1g, is placed on the arm of a recording microbalance, placed in a furnace. The furnace temperature is controlled by a pre-programmed temperature/time profile. The weight of the sample is constantly monitored as it is heated. TG analysis for the determination of the stoichiometry of UO_{2+x} relies on the irreversible oxidation of UO_2 to U_3O_8:

$$6UO_{2+x} + \left(\frac{2}{3}x\right)O_2 \leftrightarrow 6UO_{2,66}$$

The instrument used was Netzsch Simultaneous Thermal Analysis, STA 409 CD-TG-DSC. The sample was placed into a Al_2O_3 crucible in a furnace purged with a mixed flow of air and argon. The initial temperature was 20°C and was raised to 800°C with a heating rate of 5.0°C/min, and then brought back to room temperature with the same rate. The total program duration was then ≈ 7 hours. The crucible used for the analysis underwent the identical treatment without the sample, so that a correction plot was acquired and subtracted from the sample analysis. An example of the thermogravimetric analysis of the UO_2 samples used in this study is shown in Figure 3.2-1.

A correct approach is to fit both plateaus before and after the jump and find their intercepts with the linear regression of the oxidation slope: the difference in ordinates between these two points, as shown in Figure 3.2-1, is the exact weight increase associated to the UO_2 to U_3O_8 phase change.

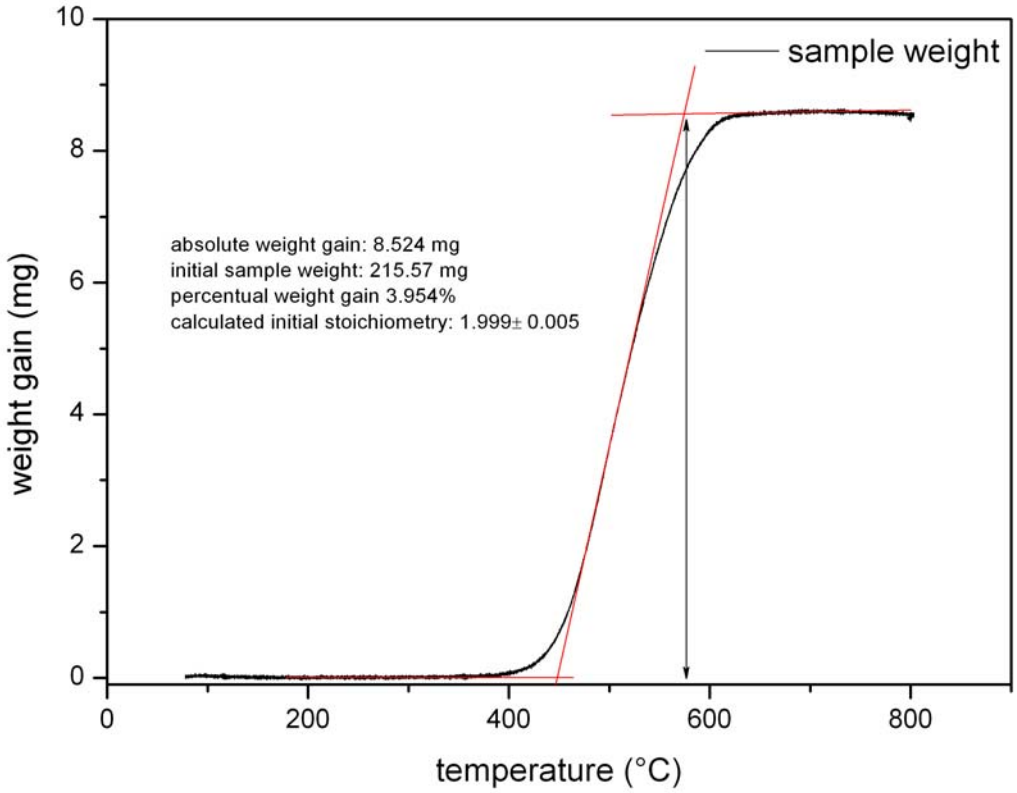

Figure 3.2-1: Thermogravimetry plot: UO_2 undergoes complete oxidation to U_3O_8. The initial stoichiometry is calculated from the resulting weight gain, measured from the difference between the intercepts of the three linear regressions.

From the weight increase ΔW of the sample, assuming no other phenomena affect this change, it is possible to calculate the initial sample ratio O/U using:

$$\frac{\Delta W}{W_i} = \frac{W_f - W_i}{W_i} = \frac{M_{UO_{2,66}} - M_{UO_{2+x}}}{M_{UO_{2+x}}} \qquad \textbf{3.2.3-1}$$

where W_i and W_f are the initial and final weight of the sample and M is the molecular weight of the different species involved in the phase change. Rearranging and substituting the molecular weights, we obtain a formula to calculate x:

$$x = \frac{10.6556 - 270.0277\,\frac{\Delta W}{W_i}}{15.9994\,\frac{\Delta W}{W_i} + 15{,}9994} \qquad \textbf{3.2.3-2}$$

Considering that the uncertainty σw in the weight determination for the thermobalance is 0.01 mg and the imprecision in the crucible correction σb (due to reproducibility of buoyancy effect) can be estimated as ≈ 0.05 mg, the uncertainty on the quantity x can be calculated according to [94]:

$$\sigma x = \frac{17.5433}{\left(\frac{\Delta W}{W_i}+1\right)^2}\frac{1}{W_i}\sqrt{\left(2+2\frac{\Delta W}{W_i}+\left(\frac{\Delta W}{W_i}\right)^2\right)\sigma w^2+\sigma b^2} \qquad \textbf{3.2.3-3}$$

From Eq. 3.2.3-1 it can be observed that the uncertainty increases with decreasing initial weight of the sample.

It is important to point out that this sort of uncertainty on the initial stoichiometry (for our samples a typical value was ± 0.005, as shown in Figure 3.2-1) can be considered sufficiently low for most bulk studies but for surface science applications a more accurate method would be needed.

Also, the sample is unavoidably exposed to air between the different sample preparation phases, which means the surface is likely to be slightly hyper-stoichiometric even though the contribution of surface oxidation is not measurable.

3.3 Corrosion/diffusion experiments

3.3.1 Static UO_2 corrosion in oxidising conditions

Several experiments were carried out in different conditions, as shown in Table 3.3-1.

Table 3.3-1: Corrosion experiments carried out in oxidising conditions for the present study.

Sample	*UO_2 matrix*	*Vial*	*Leachant*	*Temp. (°C)*	*pH*	*Surface Roughness, S_{RMS} (nm)*	*Contact-time (months)*
PC1	Polycrystalline	PE*	$H_2{}^{18}O$ (98 at.%)	≈ 25	7.6	1000	3
PC2						100-500	3
PC3							9
SC1	Single-crystal	Pyrex -glass				40-90	4
SC60				60			4
SF1	SIMFUEL 8%			≈ 25		100-500	6
PC5	Polycrystalline	PE*					3
PCCO3			$H_2{}^{18o}$ (98 at.%) 2mM $NaHCO_3$ + 10mM NaCl		8.1		3
SFCO3	SIMFUEL 8%						3
SCCO3	Single-crystal					40-90	3

*PE: polyethylene.

In general, a static corrosion experiment was carried out using a 1-2 mm-thick slice of UO_2 in a small vial containing a volume of ^{18}O-enriched water of a few millilitres.

Different UO_2 matrices were used for this (see Paragraph 3.1): single-crystal UO_2, polycrystalline UO_2 and SIMFUEL 8%.

All experiments were carried out in ^{18}O-labelled water (Chemotrade, 98 at.% $H_2{}^{18}O$) either pure or added with $NaHCO_3$ and NaCl.

Experiments had duration from 3 to 9 months: after this time, the slice was extracted from the leachate, dried in air and kept in a desiccator or stored in a vacuum chamber until it was analysed.

The experiments were performed in vials made of glass or polyethylene (PE), were generally kept at room temperature. The temperature was monitored on a daily basis. Normal variations due to daily and seasonal fluctuations were noticed, but globally contained within a range of ±3°C (22-28°C).

Only in one case, in order to evaluate the effect of temperature, a static leaching was carried out at 60°C on a single-crystal UO_2 slice. In this case, the vial containing the sample and 20 mL of ^{18}O-labelled water was sealed and placed in a thermo-bath situated in a fume hood. The water bath was regularly replenished and the temperature was ensured constant (60 ± 1°C) for the length of the experiment, during which no loss of solution due to evaporation was noted. Most of the experiments were carried out in a N_2 glovebox, with the exception of the first experiment (PC1) and the 60°C experiment (SC60), both carried out in air. However, the conditions are considered as oxidising since the N_2 atmosphere in the glovebox contains traces of oxygen (≈ 0.32 vol.% O_2).

It is known that moisture accelerates the oxidation process also at the low temperatures considered here [95]. Thus, the pellets were dried once they were removed from the solution and stored in vacuum chambers or atmospheres as dry as possible.

In an initial phase, the experiments were carried out in pure ^{18}O-labelled water. This solution is not to be considered as deionised water; the pH of this solution was measured at room temperature pH=7.6. The total carbonate content of demineralised water at room temperature, just due to atmospheric CO_2 can be estimated as $[CO_3^{2-}]_{tot} \approx 10^{-8}$ M, mostly present in the form HCO_3^- at the pH=7-8.

Considering the typical carbonate concentration of groundwater and the role played by carbonate complexation of U(VI) in the oxidising dissolution of UO_2, corrosion experiments of the three different UO_2 matrices under study were carried out also in ^{18}O-labelled carbonate solutions. In order to simulate the carbonate concentration of groundwater in a geological disposal (despite the large geographical variability), a solution containing 10^{-2} M of NaCl and $2 \cdot 10^{-3}$ M of $NaHCO_3$ was used, as it had been often regarded as a good approximation for similar corrosion studies [79, 88, 96].

3.3.2 Corrosion in reducing atmosphere: experiment in autoclave

To evaluate the effect of reducing conditions on the diffusion of oxygen, further experiments were carried out in an autoclave. The autoclave was specifically designed and manufactured at ITU for corrosion experiment performed at a pressure of 0-10 bar H_2 (Figure 3.3-1).The material of the autoclave is titanium, as stainless steel would alter and complicate the redox system of the solution in touch with it. The autoclave has a volume of 220 cm^3 and it is placed in a N_2-purged glovebox. To allow sampling of solution during the corrosion experiments, the lid of the autoclave presents two openings. The first one only reaches the head space of the autoclave, while a diving tube was connected to the second one allowing solution sampling.

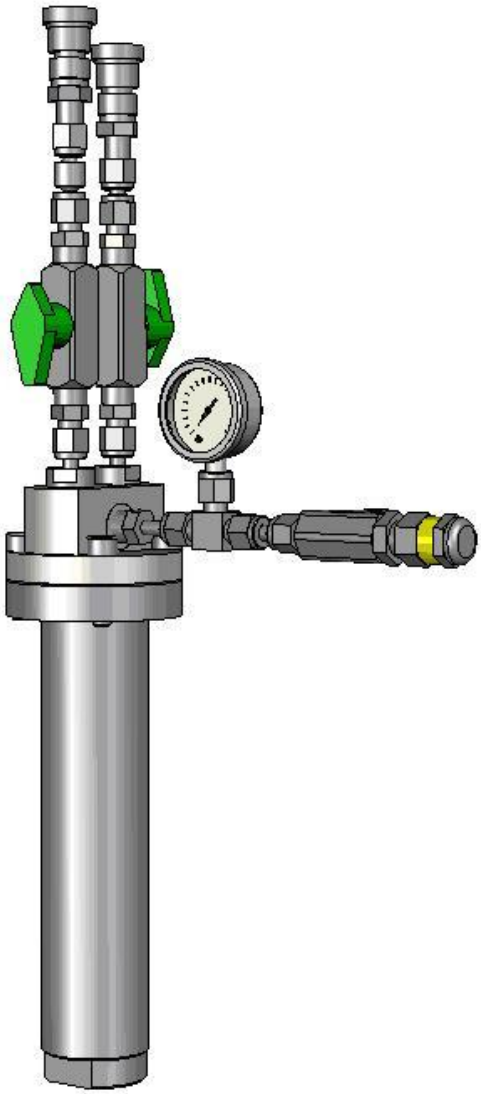

Figure 3.3-1: Titanium autoclave.

In the original design, the diving tube reaches the bottom of the autoclave [79]. A modification was implemented for this study, as parallel corrosion experiments were planned on four different samples at the same time. In order to achieve this, an internal compartmentalisation of the autoclave was needed. Four cylindrical vessels exactly fitting inside the autoclave and locking firmly one on top of the other were designed and manufactured (Figure 3.3-2). The material of choice was PEEK (polyether ether ketone) a thermoplastic resin highly resistant to attack by both organic and aqueous environments. Three of the vessels are identical and can accommodate a volume of max 10 mL. The fourth vessel, which should be placed on top of the others, has thinner walls and can contain up to 20 mL of solution. Sampling during the corrosion experiments is therefore only possible in this top vessel. The diving tube was then substituted with a much shorter PEEK tube that can reach the bottom of this vessel, through one of the apertures in the lid (Figure 3.3-2).

Tests showed that during the operation of bubbling, sampling and pressurization of the autoclave none of the solutions would spill or splash outside each vessel, guaranteeing no cross-contamination between the different experiments.

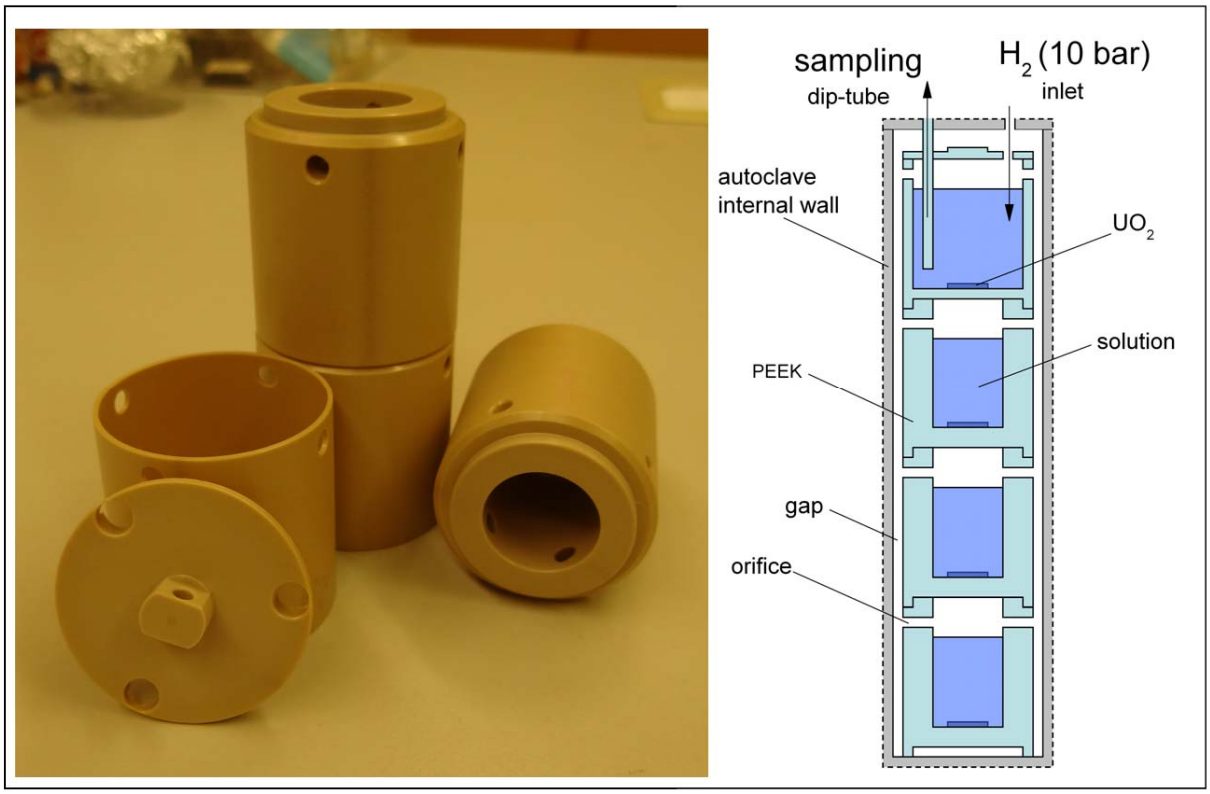

Figure 3.3-2: PEEK vessels for autoclave experiments: the scheme shows how they can be introduced in the autoclave to carry 4 corrosion experiments at the same time.

Four different experiments were then carried out simultaneously in the same autoclave, as summarized in Table 3.3-2. The autoclave was pressurised with 10 bar of H_2 containing 0.003 vol. % CO_2. The composition of the solution was the same in all four vessels: ^{18}O-labelled water H_2 ^{18}O (98 at.%) added with 2mM $NaHCO_3$ and 10mM NaCl, with pH=8.1. The experiment lasted 6 months and was carried out at room temperature (RT= 25 ± 3 °C). Sampling of the solution in the top vessel (PCA) took place three times, roughly every 2 months.

Table 3.3-2: Experiments carried out in autoclave (10 bar H_2/0.003 vol.% CO_2).

Sample	*UO_2 matrix*	*Vial*	*Leachant*	*Temp. (°C)*	*Surface Roughness, S_{RMS} (nm)*	*Contact-time (months)*
PCA	Polycrystalline	PEEK	H_2 ^{18o} (98%) 2mM $NaHCO_3$ 10mM NaCl	≈ 25	100-500	6
PCB						
SCC	Single-crystal				40-90	
SFD	SIMFUEL 8%				100-500	

3.4 Surface Characterisation

3.4.1 SEM

Scanning electron microscopy is a non-destructive surface analysis technique. Images are produced by scanning a sample surface with a high-energy beam of electrons in a raster scan pattern. The electrons interact with the atoms constituting the sample producing signals that contain information, among others, about the sample surface topography and composition.

Some of the types of signals produced by a SEM are secondary electrons, back-scattered electrons (BSE) and X-rays, which are characteristic of the atom from which they originate. The electrons that are scattered towards the sample surface are used for imaging. The backscattered electrons are those that are scattered at an angle larger than 90°: the intensity of this signal increases with increasing atomic number, so the images obtained in this way will show brighter areas where the material is denser, or characterised by “heavier” elements.

When it is coupled to an energy-dispersive X-ray (EDX) or wavelength-dispersive X-ray (WDX) detector, SEM can give even quantitative information about the sample elemental composition, although it is not a straightforward task.

The instrument used in this study is a VEGA TECSCAN equipped with EDX detector.

3.4.2 AFM

Atomic force microscopy (AFM) is a very high-resolution type of scanning probe microscopy, with demonstrated resolution on the order of fractions of a nanometre.
The instrument used for this study is a Veeco - Digital Instruments, Dimension 3100 Scanning Probe microscope in contact mode. Measurements are performed using silicon nitride cantilevers with silicon tips (Veeco, SNL-10). The nominal tip radius is 2 nm.

AFM was used to evaluate surface roughness on single-crystal UO_2 after polishing operation (Paragraph 3.2.1). The root-mean-squared roughness, S_{RMS}, typically ranged from 10 nm to 70 nm (WSxM Scanning Probe Microscopy Software [97]) on areas comparable in size to the SIMS field of analysis.

3.4.3 XPS

X-ray photoelectron spectroscopy (XPS) is used to study the energy levels of atomic core electrons, located at the surface of a solid material. XPS spectra are obtained by irradiating a material with a beam of X-rays while simultaneously measuring the

kinetic energy and number of electrons that escape from a very superficial layer of the sample. The core levels have small chemical shifts depending on the chemical environment of the atom which is ionised, allowing chemical structure to be determined [98].

The instrument used was an Omicron EA125 analyser, using a non-monochromatic Mg Kα radiation. XPS analysis of UO_2 surfaces before and after water contact was performed in order to gain information about surface oxidation and possible secondary phases. The binding energy spectra of U-4f (420-360 eV) and O-1s (540-525 eV) were acquired with similar instrumental settings on different surfaces and compared once the peaks were normalised to the same height. The O-1s peak in XPS spectra is commonly used to obtain structural information concerning the surface of minerals, including the ratios of O^{2-}, OH^-, and H_2O groups. Peaks assigned to O^{2-}, OH^- and H_2O occur at 529.6-530.4, 531.5-532.2 and 532.4-534.2 eV, respectively [99]. Peak deconvolution of the O-1s spectra was performed to isolate the O^{2-} contribution to the O-1s peak. The ratio between this area and the area of the $U4f_{7/2}$ peak was then calculated to obtain an approximation of the O/U ratio determining the surface stoichiometry of the sample.

3.5 Matrix Characterisation

3.5.1 Secondary ion mass spectrometry

Secondary ion mass spectrometry is a versatile analytical tool that provides elemental composition of a solid surface. While a primary ion beam impacts on the sample surface, the secondary ions stemming from the sputtered area of the samples are collected and separated by a mass-analyser. The secondary ions are representative of the elemental composition at the surface of the sample and consist of singly and multiply charged ions (positive and negative), neutral species and clusters of several atoms. Depending on the voltage polarity applied to the sample, either the positive or negative ions can be accelerated into the mass analyser.

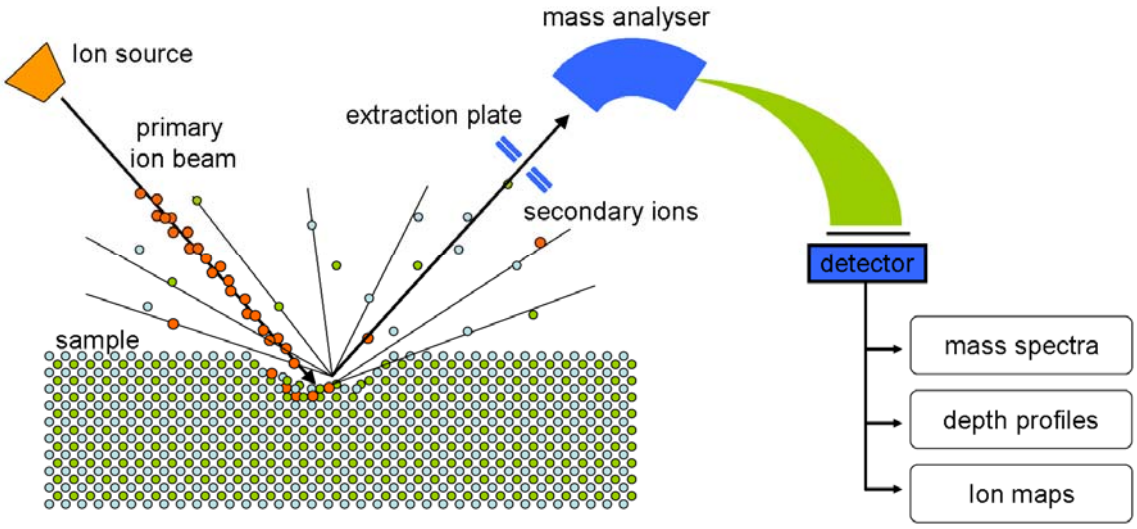

Figure 3.5-1: Schematics of SIMS physical principle and instrument.

The SIMS can be considered a mass-filtered ion microscope, which gives information of elemental, spatial and depth distribution (see Figure 3.5-1). Lateral resolution in SIMS depends on the primary ion beam diameter, which in turns depends on the intensity. At best, a lateral resolution of 0.1 µm can be achieved.

The instrument used for this study is a double focussing magnetic sector CAMECA SIMS-6F (Genevilliers, France). It is equipped with two different micro-focussing ion sources: a thermo-ionizing caesium source and a duoplasmatron source using oxygen gas. The specific application determines which source to use. For the analysis of uranium or electropositive elements the oxygen beam is employed, while for the analysis of oxygen isotopes it is necessary to use the Cs source. Several mechanical slits and apertures and electrostatic lenses are used to control both the primary and the secondary ion beam. These settings determine the analytical parameters such as the primary beam position, intensity and diameter, the size of the area sputtered by the primary beam, the size of the area from which secondary ions are collected and the mass resolution.

If operated in static mode, SIMS can be considered virtually non-destructive as only the most superficial atomic layers of the sample are involved in the production of secondary ions. In dynamic mode, instead, the sample is sputtered away removing sequentially layer by layer and giving information about the deeper composition of a bulk sample. This is the case of the depth-profiling analysis, which is the most relevant SIMS application for diffusion studies (see Figure 3.5-2).

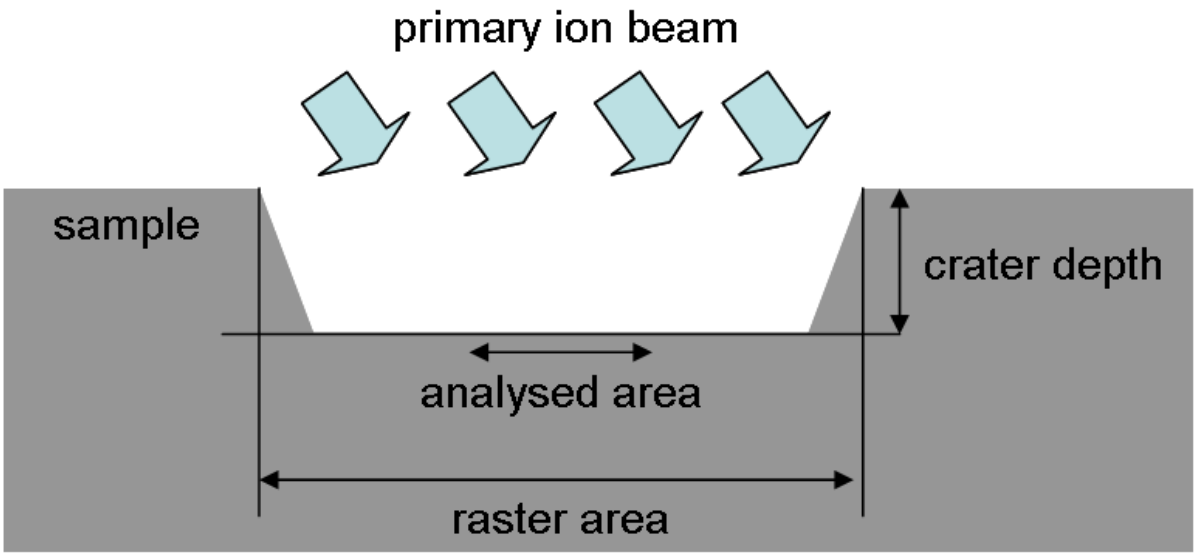

Figure 3.5-2: Sputtered crater resulting from depth profiling. The bottom of the crater is flat but smaller than the raster area (150x150 μm^2). In order to avoid collecting signal from the walls of the crater, the analysed area must be even smaller (Ø 33 µm).

SIMS can be used efficiently for quantification purposes but it is necessary to determine the so-called relative sensitivity factors specific for the element in analysis in the matrix under investigation. In fact, the intensity of the signal acquired for any selected mass does not depend only on the concentration of that specific species in the matrix. On the contrary, it depends also on the analytical conditions and the characteristics of the sputtered sample.

The so-called matrix effects represent a first obstacle, because of the varying efficiency of the SIMS ionization process for different elements in different matrices. Standards with specific elemental composition are used to measure relative sensitivity factors to apply to related matrices under similar analytical conditions.

Another issue is represented from the instrumental mass fractionation (or mass bias) resulting from the mass dispersion of the different isotopes in the secondary beam due to magnetic fields. The degree of the mass bias depends on the beam diameter and on the size of the apertures and slits affecting the secondary ion beam trajectory. If the basic settings of the secondary optics are maintained the mass bias is normally stable over long periods of time [100]. The use of standards to check on the measurement reproducibility over time is then necessary.

The ionisation process in the SIMS instrument forms easily hydride species, *i.e.* the cluster represented by any element or isotope of mass *m*, and hydrogen [101]. The hydride content depends on the sample and the analysis conditions and it is and higher on the surface of the sample. It becomes thus necessary to take into account the isobaric interference represented by this cluster on the signal of a species with mass *m+1*. This is often a very difficult issue as the mass resolution necessary is often well above the limitation of the instrument. For example, a mass resolution of >35000 would be necessary to resolve the interference of ^{235}UH from the signal of ^{236}U. Also, an increase of mass resolution always results in a loss of transmission and, as a consequence, in a lower counting statics and precision.

In the next paragraph, a description of the analysis conditions for the measurements performed in this study is given.

Analytical conditions

For the pre- and post-corrosion characterisation of the solid phase by means of SIMS, ion images and high resolution mass spectra were acquired but the main analytical tool for the study of the diffusion profiles was depth profiling.
As far as the ion maps are concerned, they were acquired with a 10 keV O_2^+ primary beam, with a ≈ 1 nA current (1-5 µm diameter) typically on a 150 x 150 µm^2 area. In the case of SIMFUEL sample, the distribution of several electropositive elements was characterised, in particular Pd, Ba, Sr, Mo and Fe were taken into consideration. Mass spectra were acquired with a 15 keV Cs^+ with intensity ≈ 1 nA and collecting negative secondary ions in the 15-21 u mass range.

Depth profiles were also acquired with a 15 keV Cs^+ primary beam, collecting the negatively charged particles, in particular ^{18}O and ^{16}O. The primary beam was rastered over a 150 x 150 µm^2 area, while the diameter of the analysed area was limited to ≈ 33 µm, so that the secondary ions were collected only from the central part of the crater (Figure 3.5-2).

The primary beam intensity was modulated according to the needed depth resolution for shallow and deep profiles that in this study will be referred to as short and long-range profiles, respectively. The short-range profiles are acquired in the near-surface area (up to a depth of 100 - 500 nm) with a primary intensity of about 2 nA, acquiring each mass for 2.5 s at each cycle. The long-range profiles are acquired instead with a more intense primary beam (with intensities of 20 to 50 nA) probing up to 30 µm depth. The acquisition time for each mass in this case is 10 s.

A typical raw depth profiles is shown in Figure 3.5-3: the intensity of the signal of every collected mass is given in counts per second (cps) and it changes as a function of the sputtering time.

The time scale of a raw depth profile can be converted into a depth scale by means of a calibration of the sputtering rate of the material under investigation. The sputter rate was determined by profilometry (Paragraph 3.5.2), and was used to convert every profile from time to depth scale.

The ^{18}O relative isotopic abundance, *c*, averaged over the surface of the analysed area was calculated according to the relation:

$$c = \frac{I(^{18}O^-)}{I(^{16}O^-)} \qquad \textbf{3.5.1-1}$$

where *I* is the measured secondary ion current, plotted against the sputtering depth.

As the purpose of this study was not to perform absolute measurements of the isotopic ratio, rather to analyse its relative variation over depth induced by diffusion, the use of standards was deemed not necessary. As in the diffusion process a concentration gradient of orders of magnitude occurred, the analytical precision in the absolute measurement of the $^{18}O/^{16}O$ ratio was not crucial in this study. For this reason, the use of standards was deemed not necessary.

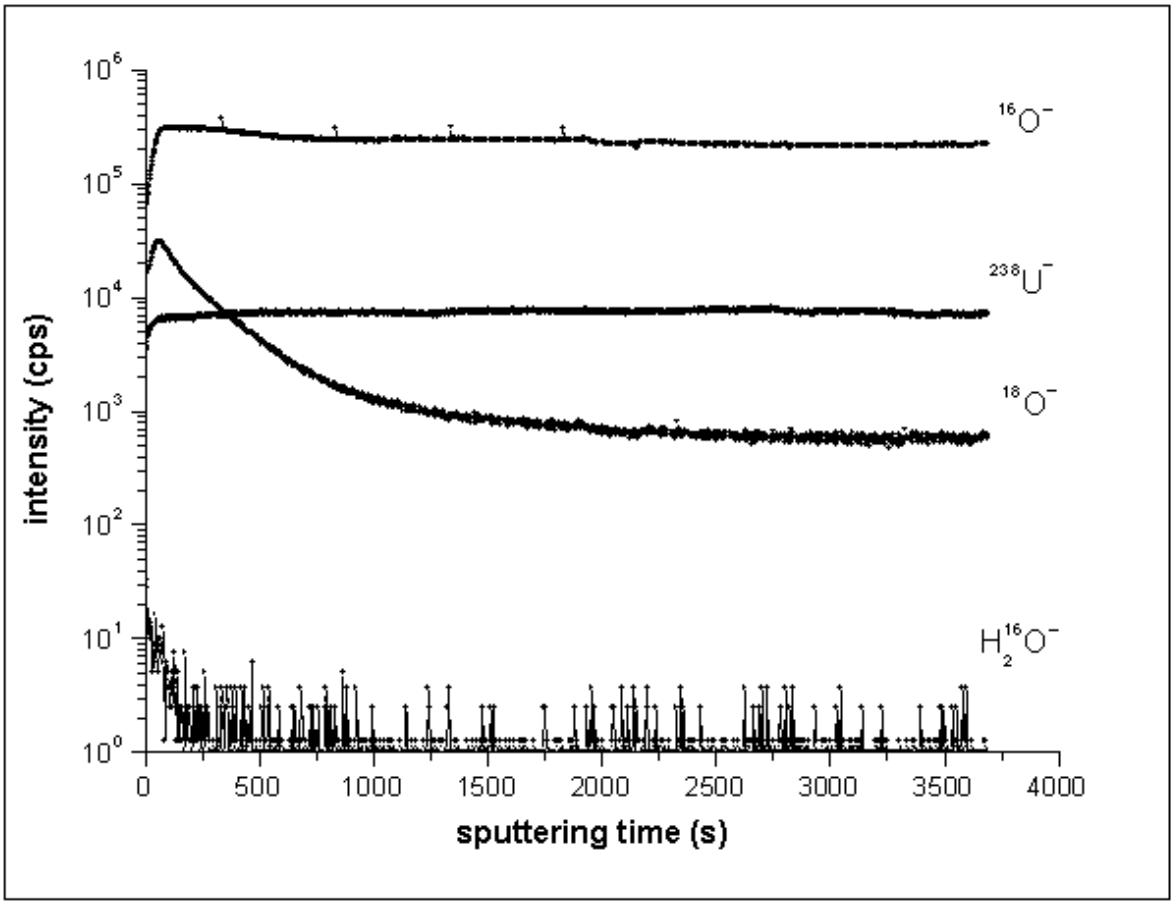

Figure 3.5-3: Raw-data SIMS depth profile: the intensity (in cps) of the signal of the selected species is plotted against the time of the analysis.

Instead, blank samples (that had not been infused with ^{18}O-water) of each UO_2 matrix were analysed together with every leached slice, acting as a reference for the original oxygen isotopic composition of the material. Also, to avoid problems of instrumental mass-fractionation, only measurements taken in identical conditions, in the sense of the mechanical setting of the instrument, were directly compared.

Despite the fact that for the diffusion experiments the samples were immersed in water prior to analysis, the problem of the formation of hydrides resulted of minor impact on the measurement of the $^{18}O/^{16}O$ ratio. In order to resolve the isobaric interference between $^{18}O^-$ (17.999 u), $^{17}OH^-$ (18.007 u) and $H_2{}^{16}O^-$ (18.015 u), the mass resolution M/ΔM of the spectrometer needed to be set at ≈ 2500. As it is shown in Figure 3.5-3, in the measurement conditions applied, no significant signal was detected for the ion $H_2{}^{16}O^-$. As for the signal of $^{17}OH^-$, as the natural abundance of ^{17}O is so low, the interference would normally be negligible. However, this is not the case of the labelled water used in our experiments, which was significantly enriched also in ^{17}O (≈ 1%). Nevertheless, this interfering signal would be following the same distribution of $^{18}OH^-$ which is also included in the $^{18}O^-$ signal. As they can be considered both as tracer for diffusion, the separation of these two signals is not a crucial problem of the analysis. Therefore, even a lower mass resolution could be used for these measurements.

Following a Poisson statistics, the relative error associated to the isotopic ratio *c*, and therefore to each point of a $^{18}O/^{16}O$ profile, can be expressed as:

$$\sigma\% = 100 * \sqrt{\frac{1}{S(^{18}O^-)} + \frac{1}{S(^{16}O^-)}} \qquad \textbf{3.5.1-2}$$

where *S* is the number of counts acquired for each mass (given by the signal intensity / in cps multiplied by the acquisition time) [102]. As the intensity of the ^{16}O signal is typically in the order of 10^5 cps (Figure 3.5-3), the main contribution to the uncertainty of each point comes from the ^{18}O signal intensity. Considering that the minimum ^{18}O signal intensity that can be acquired on UO_2 at the tail of the profile will be in the range of 10^2 cps (corresponding to the 0.2% natural abundance) the uncertainty on the ratio will be in the range of 1-5%.

Average depth profiles were calculated typically from 4-6 profiles acquired in identical conditions on each sample: the uncertainty of each experimental point was then calculated as the standard deviation of the individual measurements. This uncertainty was larger than the uncertainty of the measurement associated to every single profile and it was generally larger for the most superficial points, as different point of the surface of the same samples were often characterised by very different concentration of the diffusion tracer.

3.5.2 Profilometry

Profilometry was used to characterise surface roughness before and after corrosion and before and after SIMS measurements, and to determine the sputtering rate of the material during the depth profiling. Two different instruments were used.

For the analysis of the surface roughness of polycrystalline UO_2 samples and its evolution during corrosion experiments and SIMS sputtering, the instrument used was a MICROSURF 3D from FOGALE nanotech (Nîmes, France).

For the determination of the sputtering rate of the material, different craters were produced and their depth was measured by means of high resolution profilometer, Veeco, Dektak 8000 (Germany). Assuming that the sputter rate is constant during the analysis, the depth of a crater, Λ, is linearly related to the primary beam current density, J (nA μm^{-2}), and to the time of analysis, t_s, according to the equation:

$$\Lambda = J\,K\,t_s \qquad \textbf{3.5.2-1}$$

where the proportionality constant K is the sputtering rate per unit current density. The sputter rate K is measured for a specific analysis but, as it depends primarily on the material and on the primary beam conditions (density, acceleration, impact angle), it can be applied to convert all depth profiles acquired on the same material in similar conditions.

By analogy with Eq. 3.5.2-1, the product between the sampling rate, $K\,I_p$, and the acquisition time, *i.e.* the time during which the signal of a single mass is accumulated at every cycle, can be considered as the nominal depth resolution, associated to each point of the profile. This quantity does not represent the actual depth resolution, which is a very complex aspect of the depth profiling issue, but it can be considered an indication of the minimum depth resolution that can be expected from the analysis. In this sense, the short and long-range profiles acquired for this study are characterised by different nominal depth resolution, as both the primary beam current I_p and the acquisition time are increased when deeper profiles are acquired.

3.5.3 Fit of SIMS depth profiles for diffusion studies

SIMS depth profiling has been suggested for oxygen diffusion studies in UO_2 since the very early stage of the development of the technique [54]. The SIMS depth profiles, in fact, can be considered as diffusion profiles. Thanks to the symmetry and spatial periodicity of the crystalline and polycrystalline materials, the surface-averaged quantity measured by SIMS, $c(x)$, can be considered equivalent to the one-dimension-averaged quantity present in the functional forms that typically describe the different diffusion models.

The SIMS profiles can then be fitted according to the diffusion models that better describe the diffusive process represented in the profile, and a measurement of the diffusion coefficients of the tracer species can then be obtained from the fit. In this study, SIMS depth profiles acquired in the near-surface depth range on both single-crystal and polycrystalline UO_2 have then been fitted according to Fick's second law (equation 2.2.5-3). In particular, Cranck's [49] solution for Fick's second law was used:

$$c(x) = c_\infty + (c_s - c_\infty)\,erfc\left(\frac{x}{2\sqrt{D_L t}}\right) \qquad \textbf{3.5.3-1}$$

where c_∞, the tracer concentration at an infinite distance, is the natural concentration of ^{18}O in UO_2 and c_s is the concentration at the surface, *i.e.*, $c_s = c(0)$. The diffusion coefficient obtained from the fit has been expressed as D_L, to indicate the oxygen chemical diffusion in the UO_2 grains or crystals, *i.e.* "lattice" diffusion.

In a similar manner, deeper profiles acquired on polycrystalline samples were fitted by means of the Levine and MacCallum´s approach [67] for grain-boundary diffusion, as described in Paragraph 2.2.5. This model has been regarded as the most suitable for polycrystalline materials and it has been applied in several similar SIMS studies. In particular, is worth mentioning the work of Nagy and Giletti [103] on oxygen/water diffusion along lamellar boundaries in a macroperthitic feldspar, following hydrothermal exchange with ^{18}O-labelled water at 770 - 970 K, 1 kbar; the work of Fielitz *et al.* [104] on oxygen diffusion in polycrystalline mullite ceramics, following gas/solid exchange in an ^{18}O-enriched atmosphere at 1370 - 1600 K, 200 mbar; as well as the study of Sabioni *et al.* [74] on uranium self-diffusion in polycrystalline UO_2, following annealing in a ^{235}U-enriched UO_2 powder at 1770 - 1970 K. In all these cases, to fit the SIMS profiles acquired on polycrystalline UO_2 the following equation was used:

$$\frac{c(x)-c_\infty}{c_s-c_\infty} = \exp\left(-\alpha x^{6/5}\right) \qquad \textbf{3.5.3-2}$$

In this case, the parameter that can be obtained from the fit is α, which depends on D_L, the grain boundary width δ and the grain-boundary diffusion coefficient D_B, according to equation 2.2.5-12.

As far as the analytical precision is concerned, average depth profiles were calculated typically from 4 - 6 profiles acquired in identical conditions on each sample. The uncertainty of each experimental point was then calculated as the standard deviation of the individual measurements. In the cases in which a profile acquired on a single spot is shown, error bars are not included. This choice was made as the analytical uncertainty given by the statics of the number of counts recorded by the instrument at every point is in general very small (≈ 1 - 5%) and not meaningful from the point of view of the diffusion phenomenon.

The uncertainty of the diffusion coefficients is then resulting by error propagation calculation by the uncertainty given on the parameters obtained from the least-squared fits. Uncertainties that could not be factored in are those affecting the value of the grain-boundary width and most importantly the depth resolution affecting the depth, *x*. Both are difficult to estimate and, as it is possible to consider that their influence affects equally each point of every profile acquired in similar conditions, they are normally not considered for evaluation of SIMS depth profiling for diffusion studies.

3.6 Solution analysis

After the termination of the corrosion experiments, aliquots of the ^{18}O-labelled leaching solutions were analysed by inductively coupled plasma mass spectrometry (ICP-MS) in order to determine the concentration of uranium.

All uranium leachate samples were filtered using Microcon® Ultracell YM-3 (3000 nominal molecular weight limit) and Ultrafree Durapore PVDF 0.1µm centrifugal filter devices (Millipore, Milford, MA). Both unfiltered and filtered samples were analysed.

All ICP-MS measurements were carried out in a double focusing sector field ICP-MS (Element 2, Thermo Finnigan MAT GmbH, Bremen, Germany). Element 2 is equipped with PC^3 Peltier cooler spray chamber, a Fassel torch and a 27 MHz generator. The instrument is placed in a clean room facility class 1000. Instrumental settings are given in Table 3.6-1.

Table 3.6-1: HR-ICP-MS instrument settings

Sample introduction system and instrumental operating conditions	
Nebuliser	0.1 mL/min, self-aspiration mode
Spray chamber	PC^3 Peltier cooler
Sampling cone	Nickel
Skimmer cone	Nickel
Rf Power	1250
Plasma gas flow rate (L/min)	15.5
Auxiliary gas flow rate (L/min)	0.8
Nebuliser gas flow rate (L/min)	1.0-1.2

For the preparation of all solutions, high-purity water (18.2 MΩ cm) from a MiliQ-Element system designed for ultratrace analysis (Millipore, Milford, MA) was used. Nitric acid, suprapur grade from Merck (Darmstadt, Germany), was purified using quartz sub-boiling distillation unit. Both the water purification system and the sub-boiling distillation unit were operated in a clean room. Natural element standards were obtained from CPI international (Amsterdam, The Netherlands) as 1000 µg/mL stock standard solutions and diluted as necessary with 1 % sub-boiled nitric acid.

For calibration purpose, uranium solutions of different concentration (between 0.1 and 2 µg/L) with 1 µg/L Indium as internal standard were prepared and analysed. A calibration curve was then obtained plotting the ratio of the signal intensities $^{238}U/^{115}In$ versus the total U concentration. Linear regression was calculated using Functional Relationship Estimation by Maximum Likelihood (FREML), to estimate best fit linear relationships between two variables where both variables have significant uncertainties.

Optimised measurement parameters for uranium and Indium isotopes are given in Table 3.6-1. Typical sensitivity is $2 \cdot 10^6$ cps per µg/L of uranium.

Table 3.6-2: HR-ICP-MS optimized measurement parameters

Measurement conditions	
Resolution (10 % valley definition)	Low, M/ΔM = 300
Acquisition mode	E-Scan
Magnet settling time (s)	0.300/0.0200
Magnet mass	114.903/208.980
Mass range for ^{238}U (u)	237.653-238.447
Mass range for ^{115}In (u)	114.712-115.095
Search window (%)	100
Integration window (%)	80
Sample time (s)	0.01
Sample per peak	25
Segment duration	0.250
Detection mode	Both
Run & passes	3x20
Dead time correction (ns)	12

4 Results

4.1 SIMS depth profiling on UO_2 matrices

4.1.1 Determination of sputtering rate

Several craters of different depths were produced on a UO_2 sample by impacting a Cs+ primary beam of different intensity for different lengths of time. A 3D representation of the craters is shown in Figure 4.1-1(a). The depth of every crater, Λ, was measured by profilometry and plotted vs. the product of the primary beam current density, J (nA μm^{-2}), and of the time of analysis, t_s.
According to equation 3.5.2-1, from the slope of the straight-line fit of the plot of Λ vs. the product Jt_s, the value of the sputtering rate K was obtained: $K = (3.6 \pm 0.1)\cdot 10^{-1}$ μm^3 nA^{-1} s^{-1}. This value was used to convert the sputter time scale of every SIMS profile acquired on UO_2 to a depth scale.

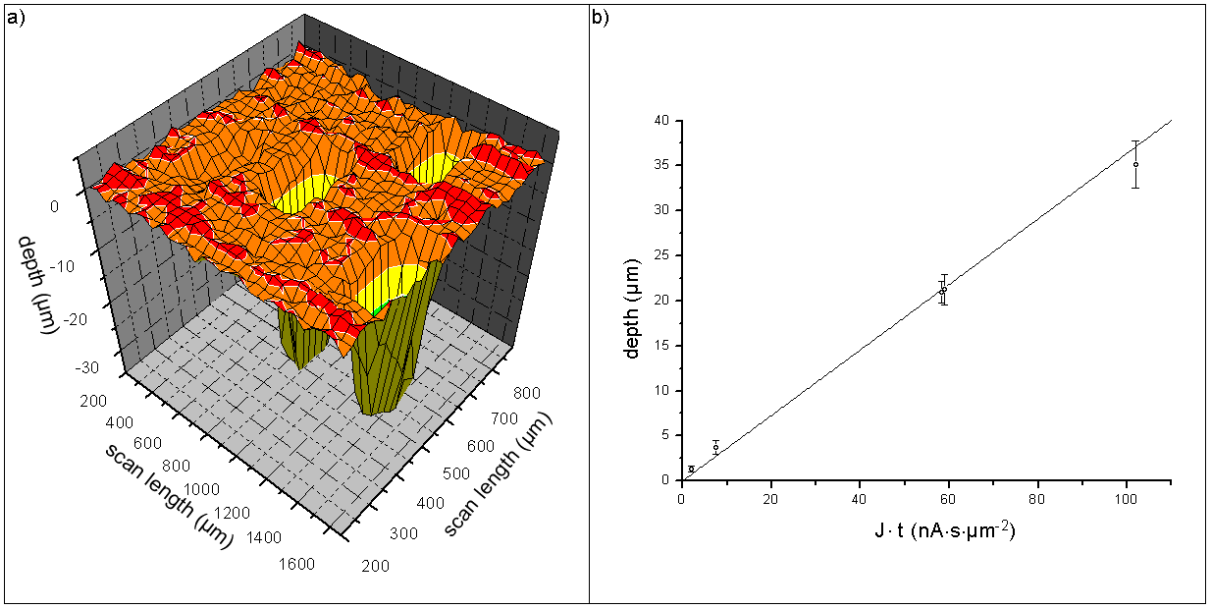

Figure 4.1-1: Calibration of sputtering rate for UO_2. a) 3D surface profilometry and b) sputtering rate calibration on polycrystalline UO_2 following crater excavation with a 15 keV Cs^+ primary ion beam at different intensities and different sputtering times.

The plot and its linear regression are shown in Figure 4.1-1. Attention is drawn to the fact that the two points around $J\ t_s \approx 60$ nA s μm^{-2} (obtained with $J_1 = 1.19\ 10^{-3}$ nA μm^{-2}, $t_{s,1} = 49680$ s and $J_2 = 2.31$ nA μm^{-2}, $t_{s,2} = 25200$ s, respectively) show very good reciprocity of the two different parameters I_p and t_s.

The possible difference in the sputtering rate due to different crystallographic orientation of the grains composing the UO_2 pellet [105], is averaged out thanks to the fact that every measurement involves a statistically significant number of grains,

given the typical raster area (150 x 150 μm^2), the range of crater depths (up to ≈ 30 µm) and the average diameter of the grains (9.4 µm).

4.1.2 Chemical form of the ^{18}O tracer

As discussed in Chapter 3, the measurement of the $^{18}O/^{16}O$ ratio acquired in the SIMS depth profiles was not deemed significantly affected by isobaric interferences represented by $H_2{}^{16}O^-$ (18.015 u) and $^{17}OH^-$ (18.007). In fact, in the condition of analysis used for the depth-profiles acquired in this study, the ion yield of the molecular species H_2O or $H_2{}^{18}O$ is very low. In Figure 4.1-2 a low mass-resolution spectra of the range 14-22 u is shown.

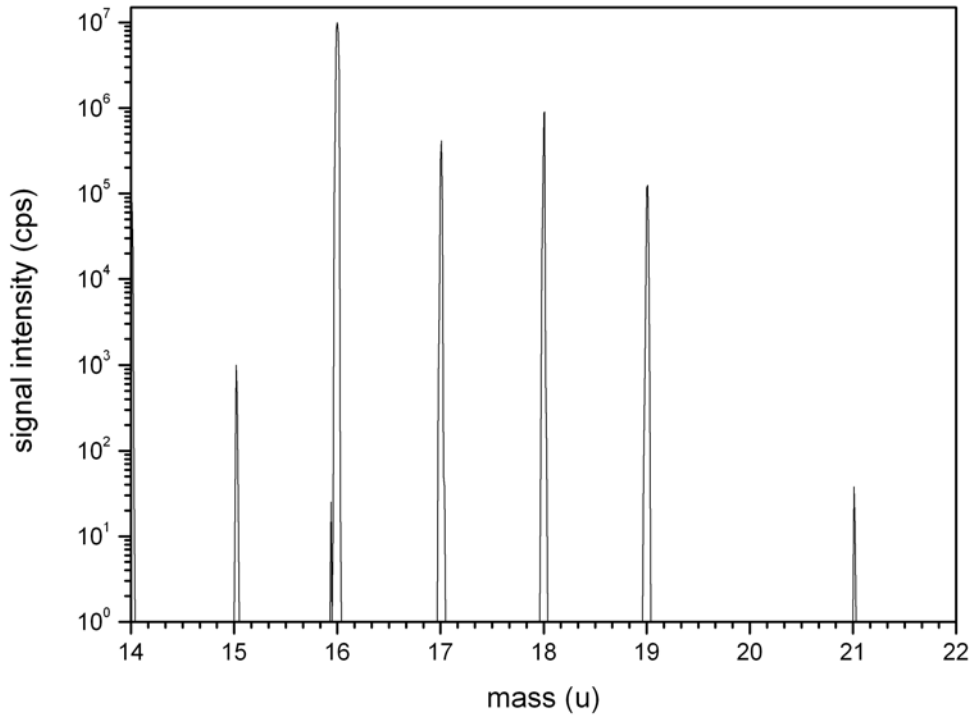

Figure 4.1-2: SIMS low-resolution mass spectra acquired on UO_2 sample after several months leaching in ^{18}O-labelled water (98 at.%). At mass 20, ^{18}O-labelled water signal is not detected.

At mass 20, ^{18}O-labelled water signal is not detected. At mass 18, nevertheless, the signal of ^{18}O is potentially affected by the interference of H_2O. Since the more abundant labelled water molecules are not detected, it is presumable that also natural H_2O does not represent a significant contribution to the signal of the mass 18. At higher resolution, the intensity of each signal is even lower.

This simplifies the analysis on one hand but, on the other hand, as reliable depth profiles cannot be acquired for the mass of $H_2{}^{18}O$, there is no possibility to consider the whole labelled water molecule as a diffusion tracer.

Nevertheless, the signal of the molecular species ^{18}OH can offer some insight. In order to detect this species, an even higher mass-resolution power than necessary to detect ^{18}O is needed. High mass resolution ($M/\Delta M \approx 5000$) depth profiling of a polycrystalline UO_2 that had been leached in ^{18}O-water was acquired, measuring the profiles of the three oxygen isotopes present in the water: ^{18}O (98 at.%), ^{17}O(1 at.%), ^{16}O(1 at.%), and their OH adducts. In Figure 4.1-3 the signal intensities of the detected species are reported against the depth.

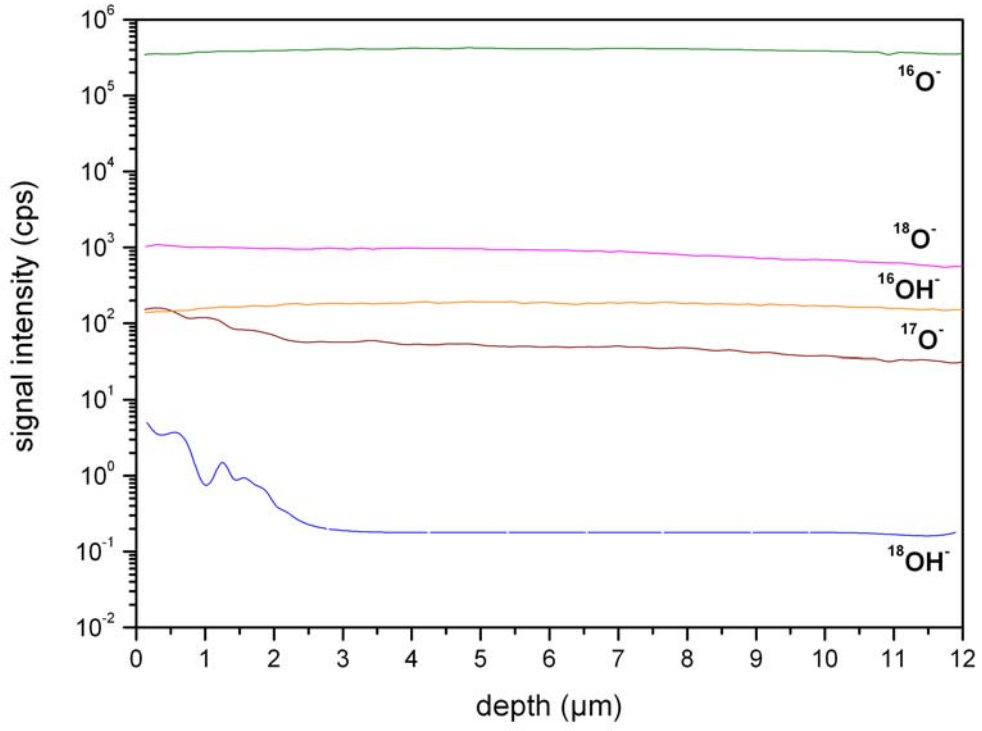

Figure 4.1-3: High mass resolution long-range depth profiles acquired on polycrystalline UO_2 after 9 months leaching in oxidising conditions in ^{18}O-water (PC3). After 2 µm the intensity of the ^{18}OH adduct decreases to its background level.

As discussed in Chapter 3, in SIMS analysis the presence of hydrogen is virtually impossible to eliminate and even if in principle hydrogen is not considered as a main matrix element, the adduct of any element with hydrogen will be detected. This becomes particularly crucial for light isotopes like oxygen [101] and even more in samples that have been completely soaked in water, like in the case of the corrosion experiments, due to an even larger amount of hydrogen available. The ratio between the intensity of the signal of a certain element present in the matrix and the signal of the adduct of this element with hydrogen can be considered constant for that element. When two isotopes are present, this ratio will be the same for both [100].

After 2 µm the intensity of the ^{18}OH adduct decreases to its background level, indicating that ^{18}OH originating from the leaching solution is chemically present in the matrix up to a depth of 2 µm.

To obtain additional information regarding the relative abundance of O^{2-}, OH^- and H_2O, XPS spectra were acquired on polycrystalline UO_2 samples, before and after water contact (Figure 4.1-4).

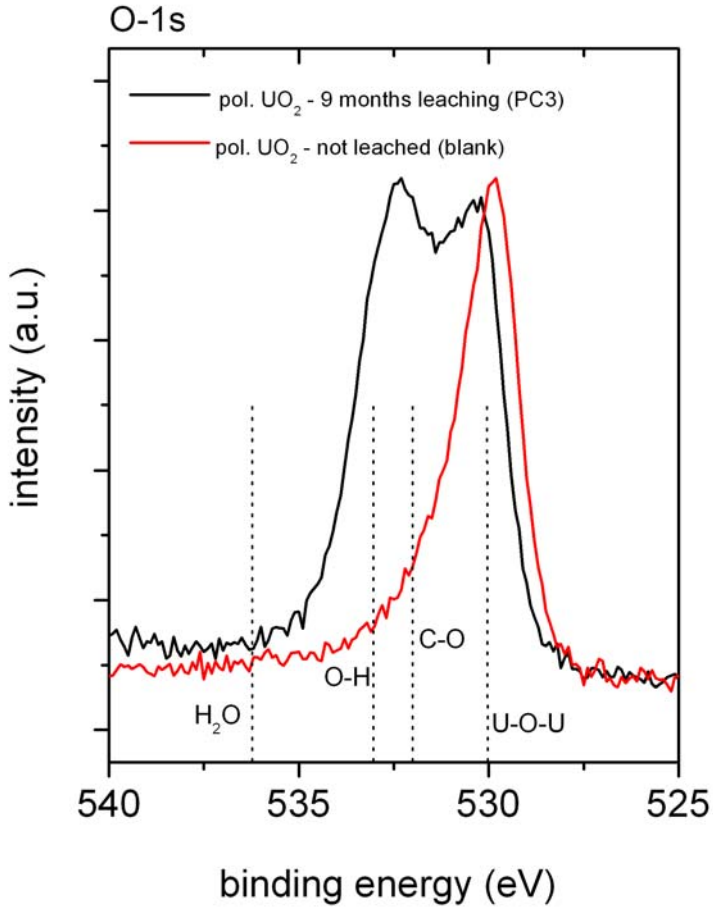

Figure 4.1-4: XPS spectra of polycrystalline UO_2 before and after leaching. A peak compatible with OH^- and not H_2O is visible in the leached sample (PC3).

The O-1s spectra were acquired for different polycrystalline samples in the range 525-540 eV. In fact, for UO_2 in particular, peaks at 529.8, 531.5 and 532.5 eV have been assigned to O^{2-}, OH^- and H_2O, respectively.
Comparing the two normalised spectra acquired for a UO_2 sample that had been exposed for 9 months to water contact (PC3) and a "blank", an identical pellet slice that had not undergone any water contact, it is possible to see that, beside the peak assignable to O^{2-}, a second peak appears. This is compatible with OH-, while no significant peak compatible with H_2O is visible.

4.1.3 Surface roughness

An important prerequisite for SIMS analysis is that the sample surface is flat. For this reason, both single-crystal and polycrystalline UO_2 samples were characterised by SEM and profilometry in order to assess the surface morphology and roughness.

For both kinds of matrices, the main contribution to surface roughness was represented by the porosity of the material (Figure 4.1-5).

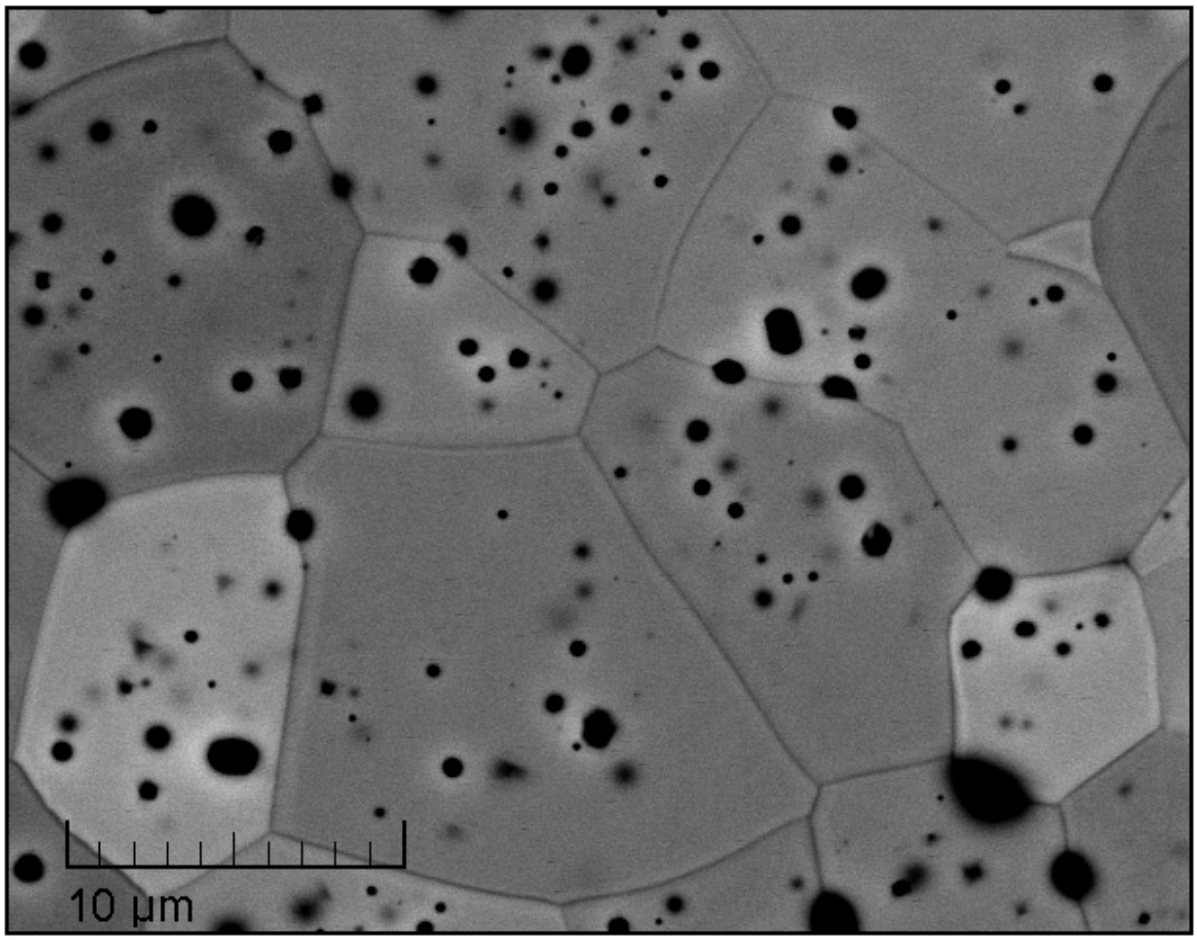

Figure 4.1-5: SEM image of polycrystalline UO_2. Grain boundaries, as well as pores, are clearly visible. The average grain size is ≈ 9 µm.

For single-crystal UO_2 samples, AFM measurements showed that the root-mean-squared roughness, S_{RMS}, typically ranged from 10 nm to 70 nm. The investigated surface areas were comparable in size to the SIMS field of analysis. The roughness factor, *i.e.* rugosity, the ratio between the true and the geometric surface area [106], was calculated to be ≈ 1.02, whereas the average slope of surface profiles was typically found to be <0.1 nm/µm. For polycrystalline UO_2 samples, SEM and profilometry characterisation showed that the surface roughness, S_{RMS}, was in the range 50-100 nm.

BSE images (Figure 4.1-6) revealed pores both before and after the experiments. For both single-crystal and polycrystalline UO_2 samples, the surface roughness remains in the same range after the corrosion experiment has taken place.

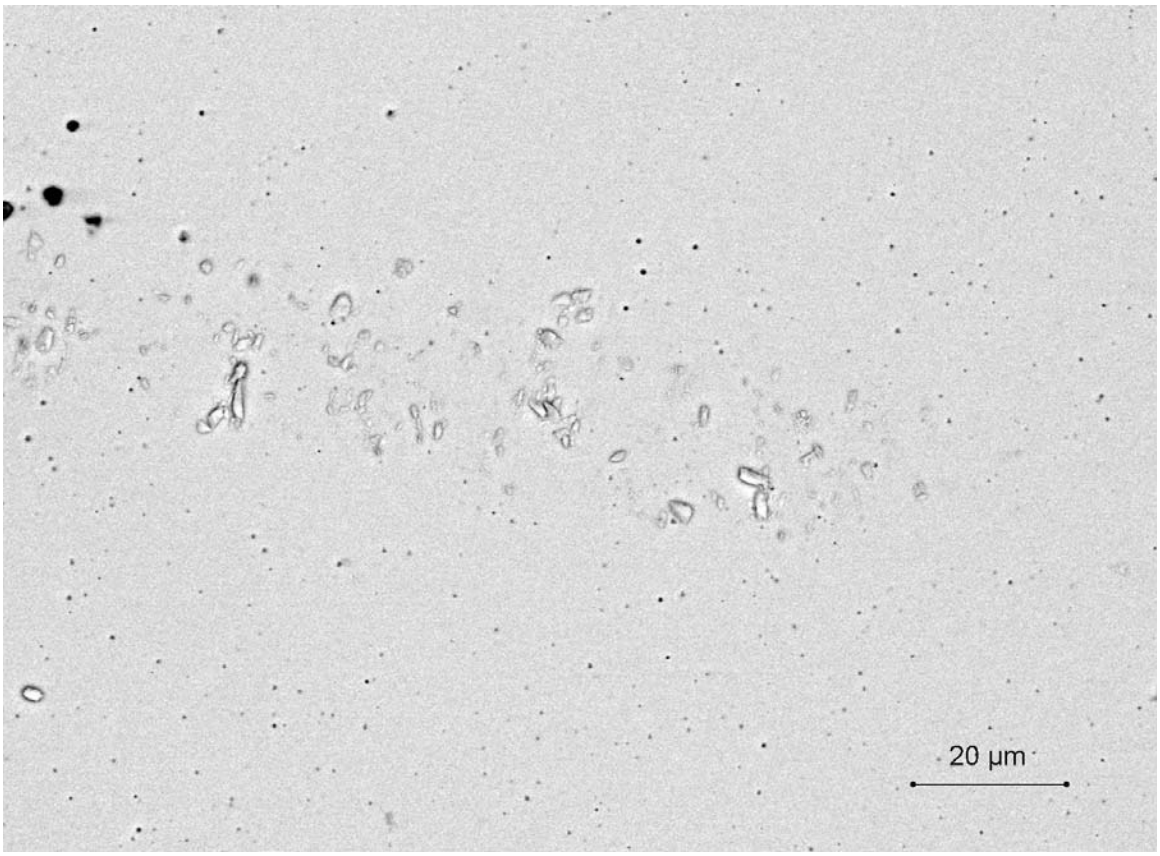

Figure 4.1-6: BSE image of single-crystal UO_2 surface. Pores of roughly 0.5 µm diameter are visible, together with some deposited corrosion products.

4.1.4 Evaluation of depth-resolution

The evaluation of the actual depth resolution for SIMS shallow depth profiling is complex as it depends on a number of factors, such as the surface roughness, the proximity to the edge of the crater and the fact that the bottom of the crater may undergo roughening during the measurement. A physical limitation to the depth resolution is also represented by the fact that the primary ions impacting on the surface produce a cascade of collisions affecting different layers of the sample, and therefore the secondary ions emitted may be originated from a deeper region than the actual sputtered depth. This effect particularly limits the analysis of very thin layers, for which it is necessary to sputter more slowly.

As introduced in Paragraph 3.5.2, the nominal depth resolution of the measurement can be considered given by the sampling rate: for the short-range profiles acquired with a primary beam of 2 nA and an acquisition time of 2.5 s, each point of the profile is associated to a nominal depth resolution of 0.1 nm.

To obtain an indication on the actual depth resolution associated to our depth profiling measurements, it was chosen to perform an experiment with zero contact

time (t = 0). A blank sample was then analysed immediately after being superficially wetted with labelled water. The so-called "zero-time" profile is shown in Figure 4.1-7.

Roughly speaking, for our purposes the width of the zero-time profile (measured, for example, at 10% of the initial value) can be regarded as the upper bound of the actual depth resolution while the nominal depth resolution, given by the sampling rate as discussed previously (Paragraph 3.5.2), can be considered the lower bound. The actual depth resolution for the near-surface profiles can then be estimated to be 2-3 nm.

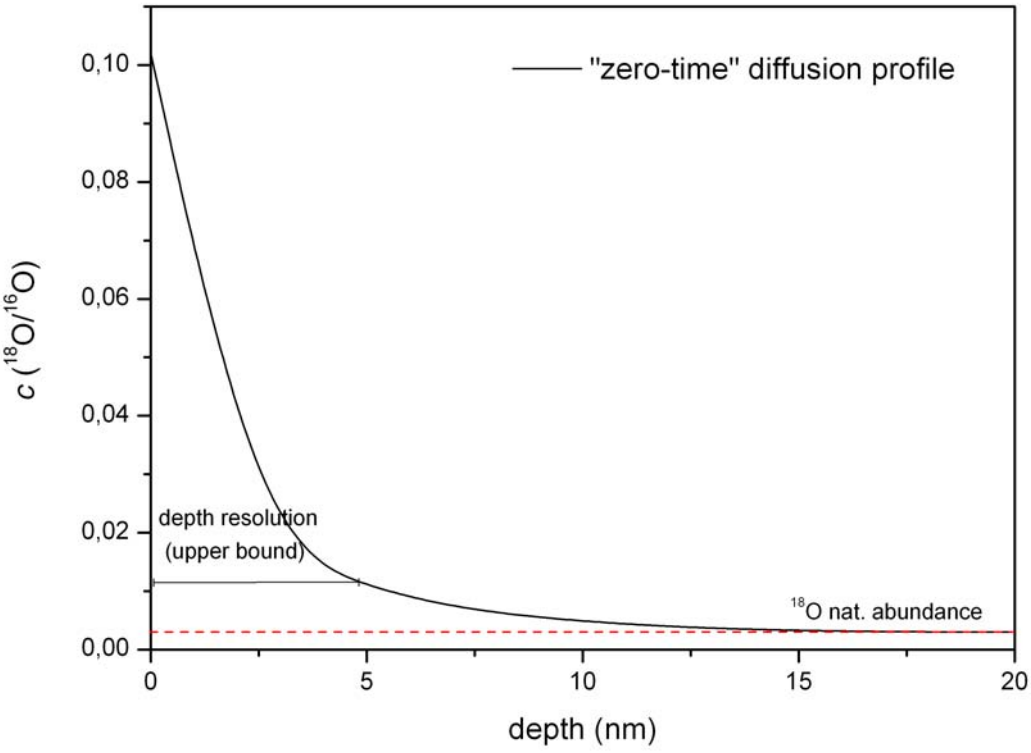

Figure 4.1-7: The zero-time diffusion profile. The depth at which the concentration has reached 10% of the initial value is considered the upper bound of the estimated depth resolution.

4.1.5 Measurement-induced surface roughness

The incidence of the primary ion beam can increase the roughness of the sputtered surface during the SIMS analysis [107]. Therefore, the surface roughness was measured also at the bottom of a SIMS sputtered crater and compared with a non-sputtered surface.

A comparison of the two kinds of surface in the case of single-crystal UO_2 samples, showed similar S_{RMS}, indicating that the primary ion beam does not have a significant roughening effect (see Figure 4.1-8). The two areas of the sample compared in Figure 4.1-8 present mostly isolated scratches originating from the handling of the specimen in and out of sample holders and a quasi-homogeneous porosity.

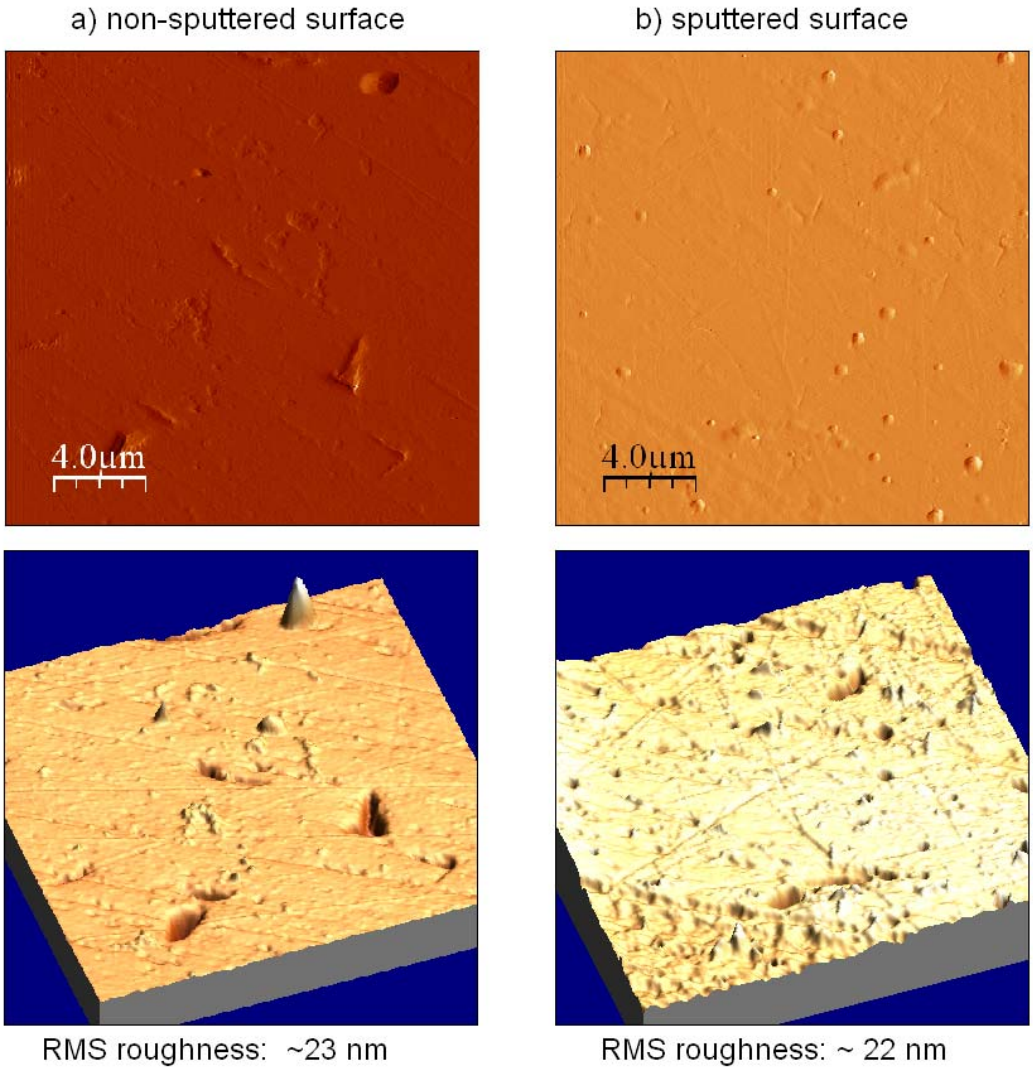

Figure 4.1-8: AFM analysis of the surface of a single-crystal UO_2 slice after 4 months leaching in ^{18}O-water under oxidising conditions (sample SC1): a) the original corroded surface; b) surface at the bottom of a 500 nm deep SIMS crater. The calculated S_{RMS} roughness is similar in both cases. It should be pointed out that these are two different areas of the sample.

For polycrystalline UO_2, instead, the surface roughness is not constant during the analysis. The presence of grains produces a fundamental difference in the sputtering modality. As visible in the in the SIMS UO_2^- ion map of Figure 4.1-9, the different crystallographic orientations of the grains result in different intensities of the matrix signal, which would be otherwise homogeneous. In fact, the signal intensity of a specific mass does not depend only on the concentration of that species but also on the sputtering yield of the material, which in turn depends, among various parameters, on the crystal orientation.

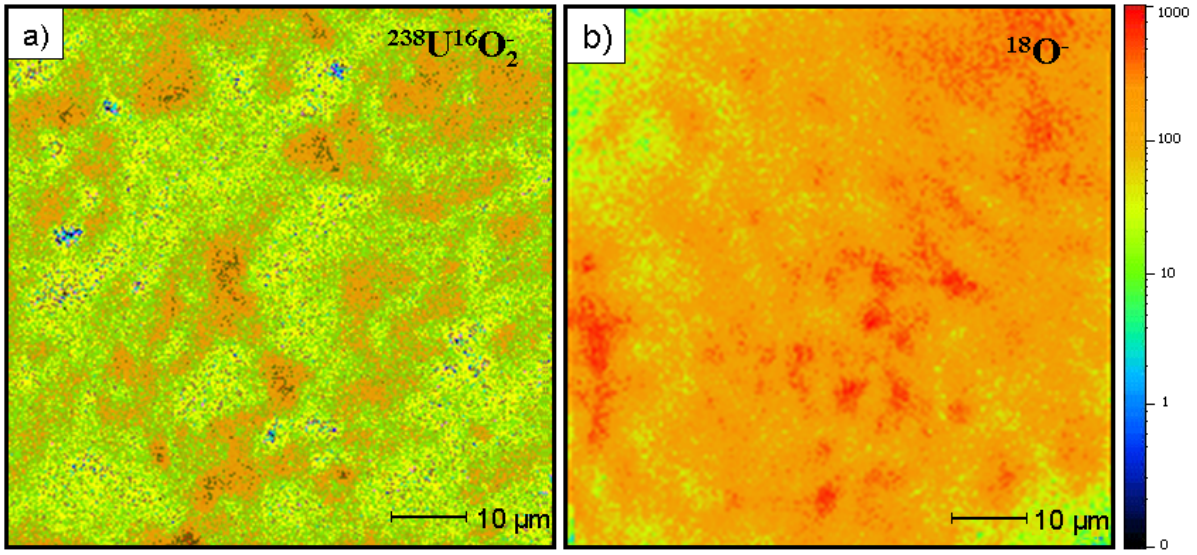

Figure 4.1-9: SIMS ion maps of polycrystalline UO_2 after leaching in ^{18}O-labelled water: a) $^{238}U^{16}O_2$ distribution, showing different intensities corresponding to the different crystallographic orientations of the grains; b) ^{18}O distribution, showing no particular distribution pattern.

This means that the different grains will be sputtered with slightly different rates. As discussed in the previous paragraph, this does not have a consequence on the evaluation of the sputter rate for UO_2, which is averaged out in every measurement thanks to the fact that a statistically significant number of grains is involved [105]. In this sense, actually, the depth scale associated to each SIMS profiles using the sputter-rate determined as discussed previously, should be the more reliable the deeper the crater.

Nevertheless, the slightly different sputtering yield of the different grains has a consequence on the measurement-induced roughening of the surface under sputtering. SEM images (Figure 4.1-10) of the craters shows clearly that the different grains have been sputtered with a different rate. Measurements of roughness inside and outside SIMS craters showed that, unlike the single-crystal case, the roughness of the crater bottom is always larger than the sample surface. The results of the SIMS sputter-induced surface roughness are summarized in Table 4.1-1.

From the values summarised in Table 4.1-1 it is possible to infer that the roughening of the surface, caused by the different crystallographic orientation of the grains, does not increase indefinitely with the depth of the craters. Considering that in every measurement crater a large number of grains with different orientation is sputtered away, it is logical to assume that the measurement-induced roughness reaches a quasi-constant value once a depth equal to or larger than one mean grain diameter (≈ 10 µm) is reached.

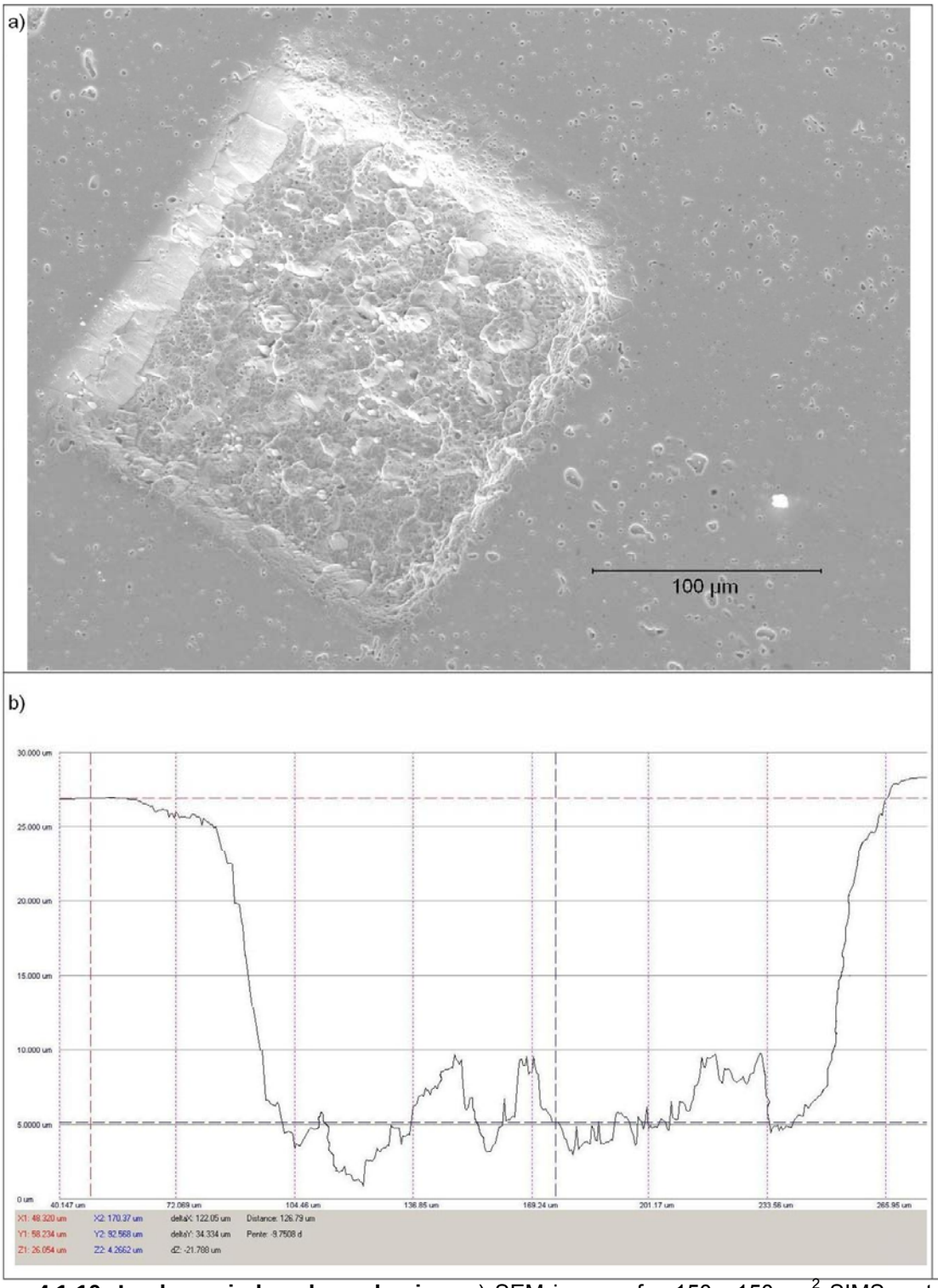

Figure 4.1-10: Ion-beam induced roughening: a) SEM image of a 150 x 150 µm^2 SIMS crater on leached polycrystalline UO_2; b) profilometry of the crater (5 µm depth) shows at the bottom a rougher surface due to different sputter rate of the different grains.

Table 4.1-1: SIMS sputter-induced roughness in polycrystalline UO_2.

	SIMS sputtering	*Crater depth (µm)*	*Roughness, S_{RMS} (µm)*
Surface	--	--	0.05
Short-range profiles	2 nA ≈ 2-3 h	0.5	0.23
		0.8	0.13
Long-range profiles	20 nA ≈ 5-10 h	7.0	3.00
		23	2.00

4.2 Experiments in oxidising conditions

In this section, the results of the experiments carried out in oxidising conditions (air or N_2 glovebox) are presented. The different UO_2 matrices in analysis are considered separately, starting from the simplest case, single-crystal UO_2 slices, then proceeding to polycrystalline materials (natural UO_2 and SIMFUEL 8%). Finally, the experiments carried out in ^{18}O-labelled water containing carbonate are presented, comparing once again the three UO_2 matrices. In every sub-section, the total uranium concentration measured in the leachate by ICP-MS is given in the summary table; SIMS depth profiles are shown for each experiment in terms of the $c = {}^{18}O/{}^{16}O$ isotopic ratio plotted against the converted depth scale, as calculated according to the measured sputtering rate. The fitted curves according to the relevant diffusion model are also displayed, as well as the diffusion coefficients obtained from the fit.

4.2.1 Single-crystal UO_2

Two experiments were carried out on single-crystal UO_2 slices at two different temperatures, as summarized in Table 4.2-1.

Table 4.2-1: Corrosion experiments on single-crystal UO_2 in oxidising conditions.

Sample	*UO_2 matrix*	*Vial*	*Lechant*	*Temp. (°C)*	*Contact-time (months)*	*$[^{238}U]$ (M)*
SC1	Single-crystal	Pyrex-glass	$H_2\,{}^{18}O$ (98 at.%)	≈ 25	4	$(1.60 \pm 0.05)\cdot10^{-8}$
SC60				60		$(3.98 \pm 0.11)\cdot10^{-8}$

As shown in Figure 4.2-1, SIMS depth profiling allows us to recognize the increase in diffusion length resulting from the increased temperature, from room temperature (RT ≈ 25°C) to 60°C, maintaining constant the contact time of the experiment (t = 4 months). In fact, literature data for oxidation of UO_2 show that the oxygen diffusion coefficient in UO_2 follows the temperature with an Arrhenius-type dependence [32].

A qualitative indication of the diffusion length characterising each profile can be obtained from the measurement of the depth at which the $^{18}O/^{16}O$ ratio is 10% of the value at the surface. In this way, it is possible to observe that there is roughly a factor 2 between the two profiles.

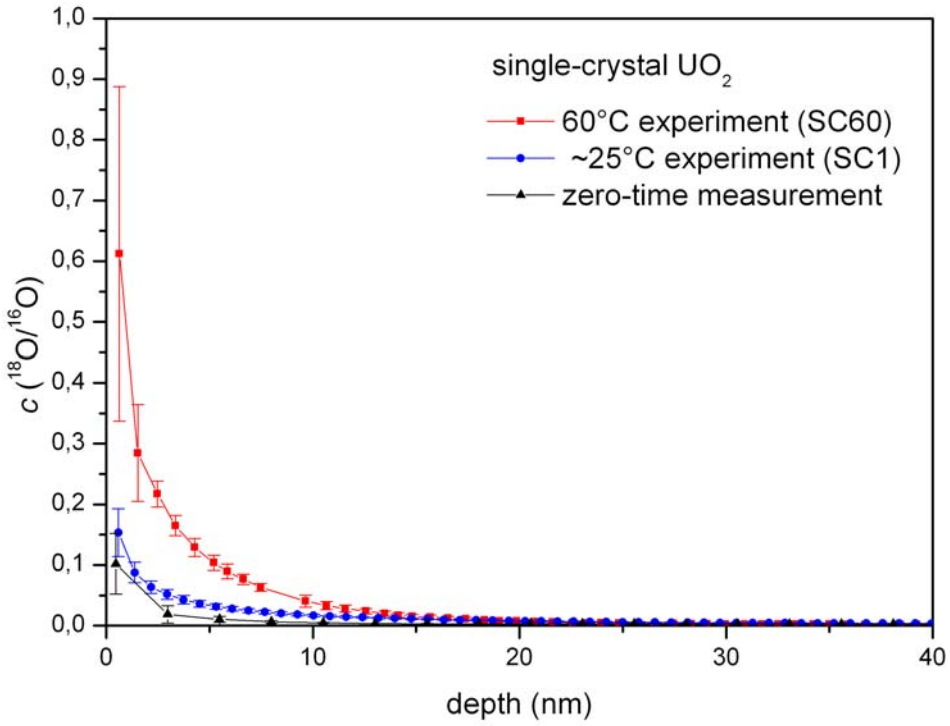

Figure 4.2-1: SIMS depth profiles acquired on UO_2 single crystals. The black curve (triangular points) represents the so-called zero-time experiment as it is acquired immediately after that the surface of the sample has been wetted with ^{18}O-labelled water. The blue curve (circular points) represents the room-temperature experiment while the red curve (squared points) the 60°C experiment. Both experiments lasted 4 months.

It is also possible to note that the zero-time profile is relatively close to the SC1 profile (≈ 25°C), obtained after 4 months contact time.

Fitting the ≈ 25°C profile with the aforementioned solution of Fick's second law (equation 3.5.3-1), the value of diffusion coefficient obtained is $D_L = (5.2 \pm 0.3) \cdot 10^{-23}$ m^2/s. The high uncertainty on the most superficial points forces the fitted curve to rely mainly on the tail of the profile.

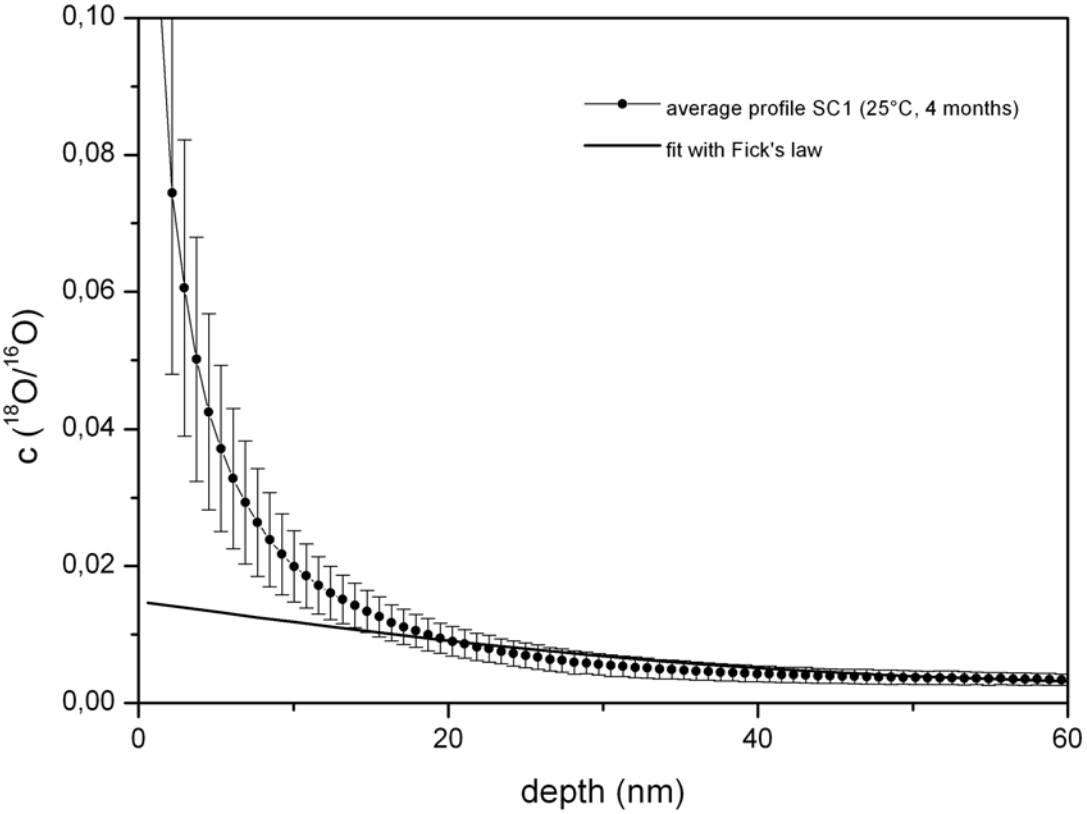

Figure 4.2-2: Average profile acquired on single crystal UO_2 after 4 months in ^{18}O-labelled water at RT. Least-squared fit according to Fick's law (Equation 3.5.3-1).

Fitting the 60°C profile the diffusion coefficient obtained is $D_L = (6.9 \pm 0.7) \cdot 10^{-24}$ m^2/s, which is one order of magnitude lower than what determined at ≈ 25°C. None of the two values appears obviously implausible in comparison with literature data but they are in disagreement with each others, since the temperature dependence implies that at ≈ 25°C D_L should be lower than at 60°C.

This could be attributed to the fact that surface effects and depth resolution problems have a severe impact on shallow profiles. In fact in both cases the most superficial points of the profiles are affected by a large uncertainty and they are ignored by the best fit curves. For the 60°C experiment, though, thanks to a deeper penetration, this superficial part does not cover a large portion of the total diffusion profile, like for the room temperature experiment, and therefore it is statistically more meaningful to rely on the tail of the profile to deduce the diffusion coefficient.

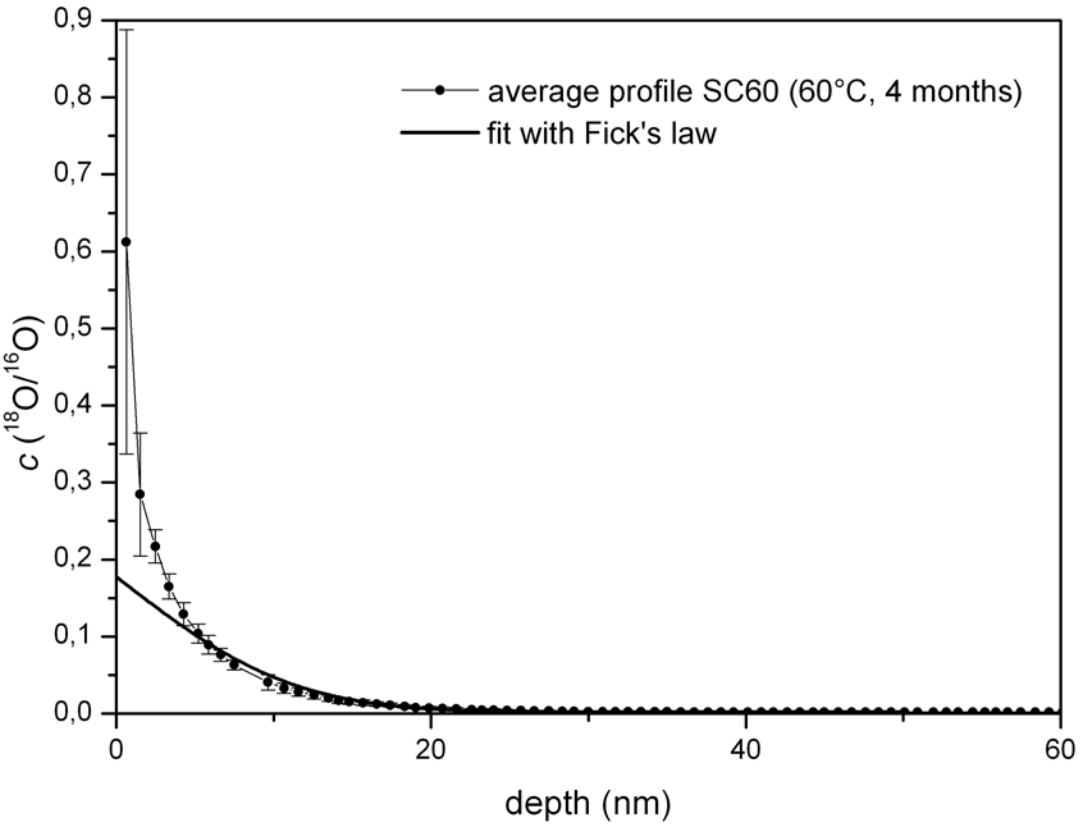

Figure 4.2-3: Average profile acquired on single crystal UO_2 after 4 months in ^{18}O-labelled water at 60°C. Least-square fit according to Fick's law (Equation 3.5.3-1).

This becomes more visible plotting the same average profile according to a different representation. Because of the asymptotic formula $erfc(z) \approx (\pi)^{-1/2} z^{-1} \exp(-z^2)$ for large z (z = x/[2(Dt)$^{1/2}$]), a semi-logarithmic plot of x(c-c$_\infty$) versus x^2 should yield curves approximated by the following equation [108]:

$$\ln[x(c(x)-c_\infty)] \approx \frac{1}{4D_L t} x^2 + \ln\left[(c_s - c_\infty)\frac{2D_L t^{1/2}}{\pi}\right] \qquad \textbf{4.2.1-1}$$

This implies that, for large penetration depths, the slope of the curves in a log (x(c(x)-c$_\infty$)) versus x^2 plot is inversely proportional to $4D_L t$. Such a plot is shown in Figure 4.2-4. Even small differences in the diffusion coefficients (for the same contact times) are easy to see because of the different slopes in this type of plot.

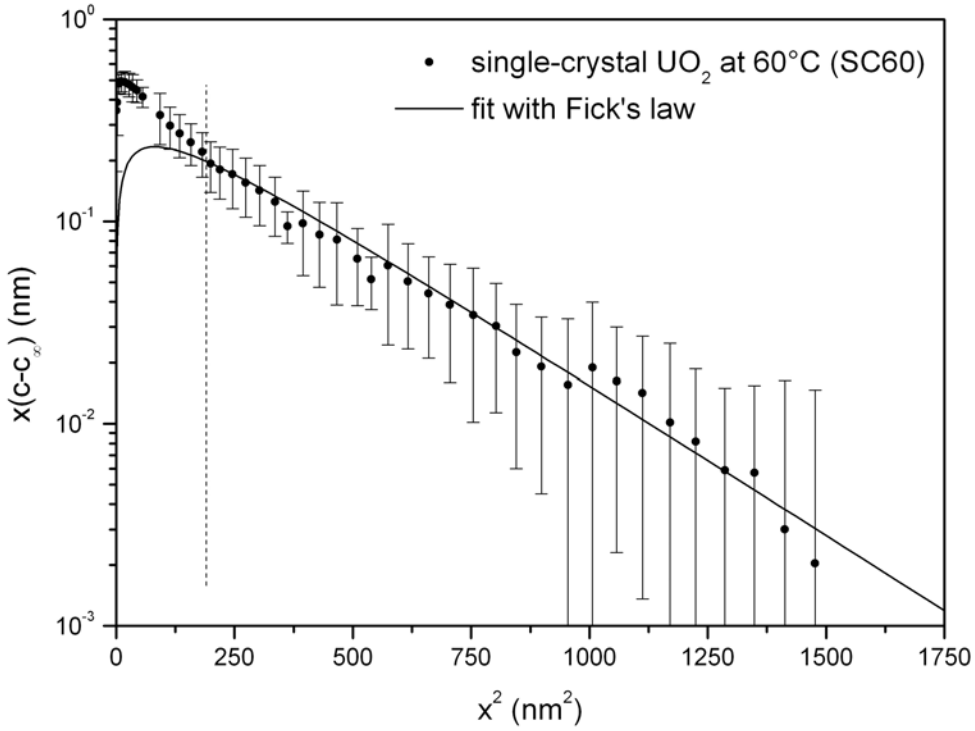

Figure 4.2-4: Diffusion profile acquired on single-crystal UO_2 after 4-month leaching at 60°C. Least-square fit according to Fick's law (Equation 3.5.3-1).

The change in slope marked by the dashed line in Figure 4.2-4 indicates the presence of an interface. In fact, the presence of a secondary phase was easily recognizable partially covering the sample surface after leaching at 60°C (Figure 4.2-5).

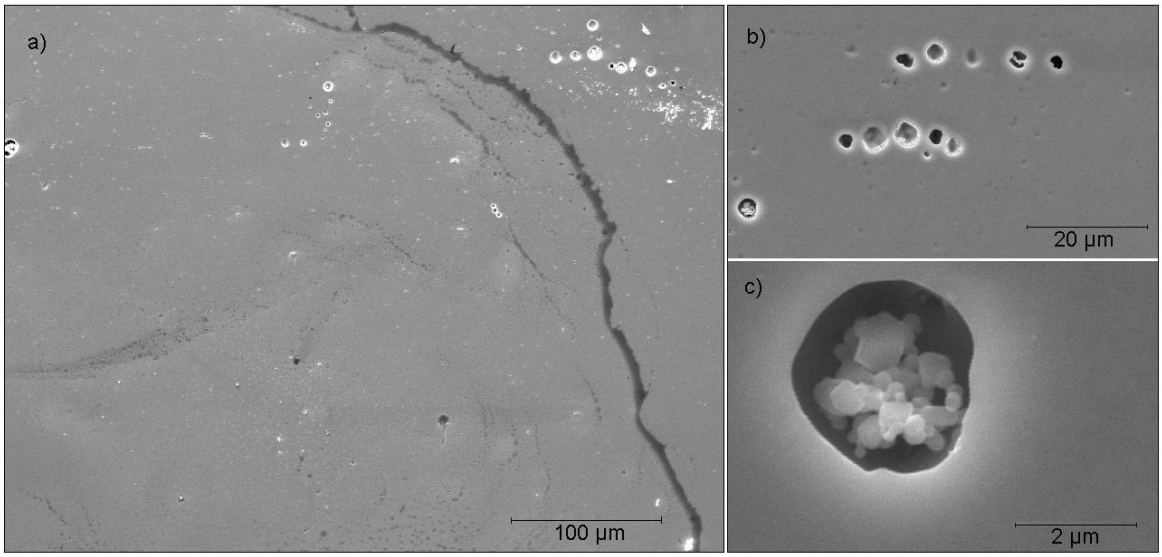

Figure 4.2-5: SEM images over single crystal UO_2 after 4 months leaching in ^{18}O-water at 60°C (SC60). A) Partial coverage by a secondary phase; b-c) enlarged pores where secondary phases are deposited.

SIMS ion mapping showed that the secondary phase was rich in Si and O, and has a higher $^{18}O/^{16}O$ than the rest of the surface (Figure 4.2-6). At the same time, it cannot be excluded, then, that the superficial part of the profile in Figure 4.2-4 is due to the same silicate phase, only much thinner than on the visible areas. The depth of such layer cannot be deduced from Figure 4.2-4 as the sputtering rate used for the calibration of the depth scale is only valid for UO_{2+x} phases: presumably, the silicate layer should be much thinner than 15 nm.

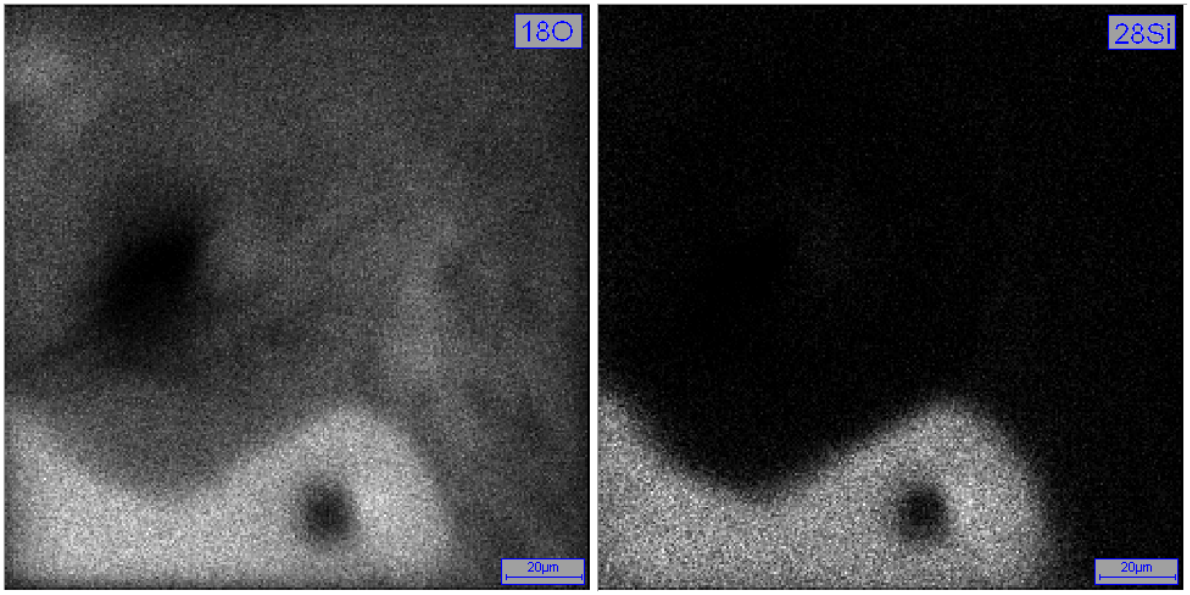

Figure 4.2-6: SIMS oxygen ion maps of UO_2 single-crystal after 4 months leaching at 60°C (SC60). A portion of the surface showing partial coverage by a secondary phase particularly rich in ^{18}O and Si.

ICP-MS analysis showed presence of Si (≈ 10^{-7} M) in the leachate, which originates from the pyrex-glass vial used for the experiment. It is likely that oxidised UO_2^{2+} at the surface was complexed by silicic acid, H_4SiO_4, through the reaction [75]:

$$UO_2^{2+} + SiO(OH)_3^- \rightarrow UO_2SiO(OH)_3^+ \qquad \log \beta_0 = 8$$

In the uranium(VI)-silicate mineral group, $(UO_2)_2SiO_4 \cdot 2H_2O$ (cr), soddyite, is the only compound reported [75]. Soddyite has a relatively low solubility (log K_{SP} = 6.43) and at pH = 7 can maintain the U concentration below 10^{-6} M [109].

The area covered by the visible, thicker, Si-bearing secondary phase had initially been excluded from the depth profiling analysis of the $^{18}O/^{16}O$ ratio since it would not have been representative of a diffusive process in UO_2. However, a profile acquired in this part of sample is shown in Figure 4.2-7. Two sequential regimes are distinguishable even in the simple representation of the $^{18}O/^{16}O$ ratio vs. the sputtered depth. The most superficial part of the profile, which is influenced by the incorporation of ^{18}O in the secondary phase layer, was not considered for fitting. The oxygen diffusion coefficient in UO_{2+x} can be evaluated by fitting the deeper part of the profile. The value of D_L obtained from the fit is $D_L = (1.7 \pm 0.2) \cdot 10^{-22}$ m^2/s.

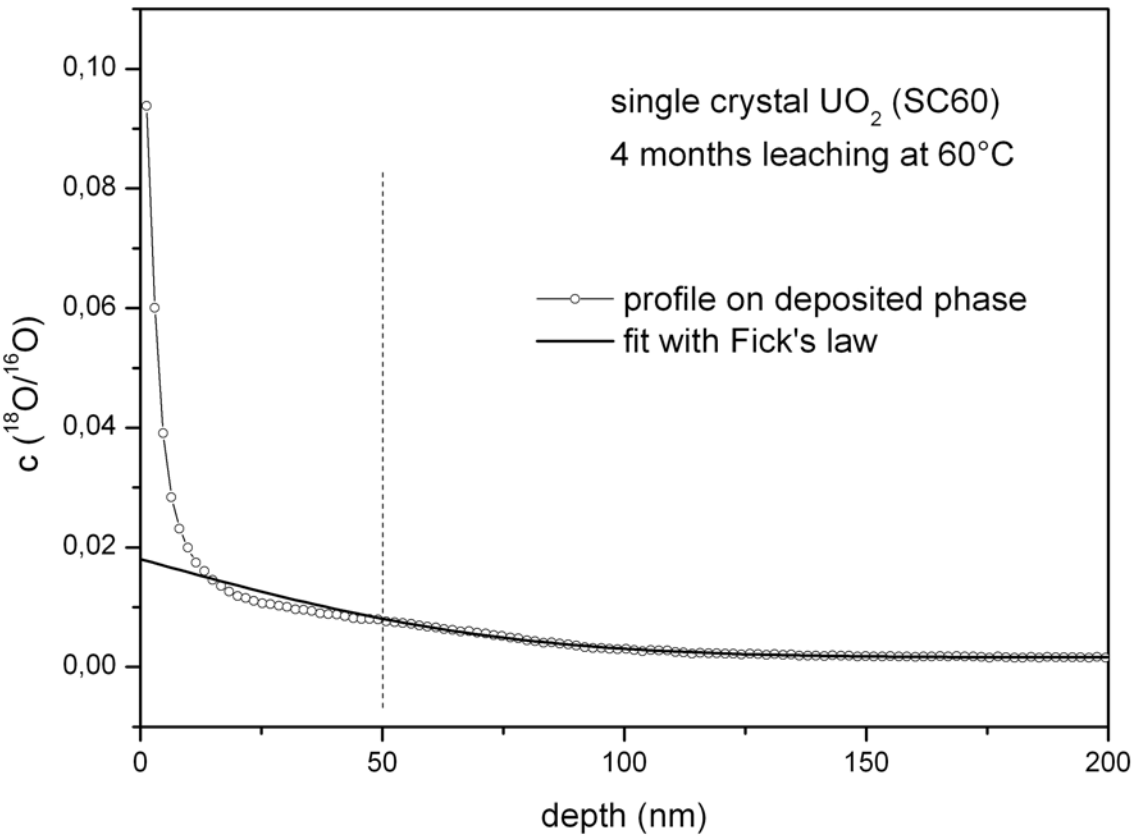

Figure 4.2-7: SIMS depth profile on single-crystal covered by a Si-bearing secondary phase (sample SC60). The depth scale used comes from the sputtering rate in UO_2 and therefore cannot be considered valid for the deposited phase, but the tail of the profile (after the dashed line) could be fitted by means of Fick's law to obtain the oxygen diffusion coefficient $D_L=(1.7 \pm 0.2)\cdot 10^{-22}$ m^2/s.

This diffusion coefficient is different from what was obtained from profiles acquired on areas free from Si-containing secondary phases (Figure 4.2-3). This can be explained by the presence of phases with different stoichiometry, as the oxygen diffusion coefficient in UO_{2+x} depends on x.

4.2.2 Polycrystalline UO_2

Several experiments were carried out on polycrystalline UO_2 in oxidising conditions, as summarized in Table 4.2-2.

Table 4.2-2: Corrosion experiments on polycrystalline UO_2 under oxidising conditions.

Sample	*UO_2 matrix*	*Vial*	*Leachant*	*Temp.*	*Contact-time (months)*	*$[^{238}U]$ (M)*
PC1	Polycrystalline UO_2	PE	$H_2\,^{18}O$ (98%)	≈ 25	3	$(4.39 \pm 0.08)\cdot 10^{-7}$
PC2					3	$(2.10 \pm 0.04)\cdot 10^{-7}$
PC3					9	Not determined
PC5					4	$(1.95 \pm 0.60)\cdot 10^{-7}$

As shown in Figure 4.1-9.b SIMS $^{18}O^-$ ion maps acquired on the surface did not show a distribution pattern of the tracer suggesting that surface oxidation preferentially occurs along the grain boundaries. Evidence of grain boundary diffusion is instead found in the analysis of SIMS depth profiles.

As mentioned earlier (Paragraph 3.5.1) two typologies of depth profiles have been acquired by means of SIMS: short and long-range profiles, according to the intensity of the primary ion beam and, as a consequence, to the nominal depth resolution of the measurement. Short-range profiles are used to probe the near-surface area of the sample, while long-range profiles are long lasting acquisition probing the sample down to depths of several μm.

Thanks to these two modalities, in some of the polycrystalline pellets leached under oxidising conditions (Table 4.2-2) it was possible to identify two different diffusion regimes. In Figure 4.2-8 an example of this double regime is visible, as a short and long-range profile acquired sequentially on the same spot of sample PC2 have been shown together on a log-log scale. In this representation, it is immediate to note how several orders of magnitude are involved, both from the point of view of depth and concentration.

The first part of the profile, in the most superficial area of the sample, is acquired with a less intense primary ion beam (2 nA), so that the first tens nm beneath the sample surface could be analysed with a higher depth resolution (0.1 nm in this case). As mentioned earlier, the nominal depth resolution is determined only by the sampling rate (the product of the time between two consecutive points of the profile and the sputtering rate of the material) while the actual depth resolution is larger and can be estimated thanks to the acquisition of the zero-time profile. The zero-time profile provide with an indication of the actual depth resolution (≈ 5 nm) of the measurement that includes the effect of the SIMS-induced roughening of the surface due to the different sputter-rate of the grains. Depth profiles acquired at higher primary beam intensity (typically 20 nA) and several hours of continuous sputtering, showed a

deviation up to a depth of at least 22 µm from the natural $^{18}O/^{16}O$ isotopic ratio measured on the non-leached pellet ($c_\infty = 2.0 \cdot 10^{-3}$). This reveals a long-range, low-concentration (in the order of a few permille, surface-averaged) "water" diffusion regime, and suggests that the grain boundaries, behaving as high diffusivity paths, are responsible for the penetration of the leaching solution up to such depths. As visible in Figure 4.2-8, a transition between the two regimes is recognisable as a sort of plateau.

As also reported by other authors, the near-surface region of the sample can be considered the result of fickian volume diffusion in the grains and therefore fitted by means of Fick's law, considering the value at the plateau virtually constant [57]. As visible in Figure 4.2-8, this short-range profile shows a steep decrease in concentration, in the order of 10% within less than 20 nm.

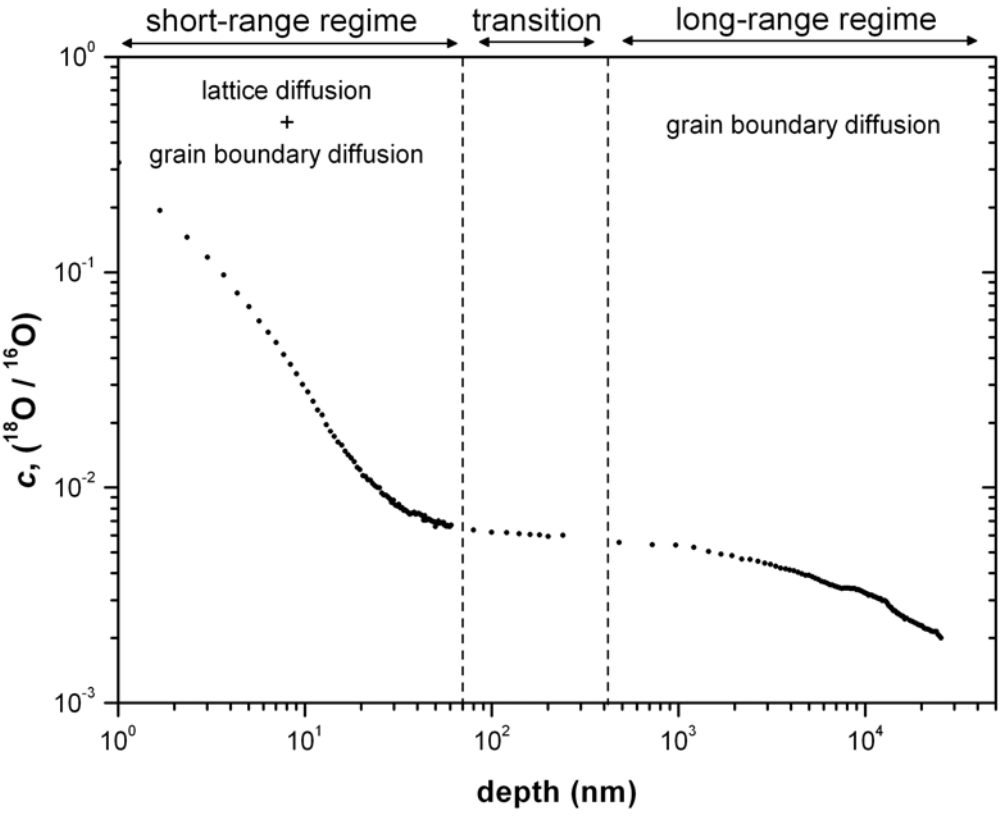

Figure 4.2-8: SIMS depth profile on polycrystalline UO_2 leached in ^{18}O-labelled water. The different diffusion regimes are visible (log-log scale).

While in the case of the single-crystal UO_2 sample, the fickian diffusion profile reached a plateau value corresponding to the natural isotopic ratio $^{18}O/^{16}O$ ($c_\infty = 2.0 \cdot 10^{-3}$), for a polycrystalline sample the plateau value indicates the transition between two diffusive regimes and the plateau value, that can be defined as c_b is therefore higher. In Figure 4.2-9 the short-range profile is represented by plotting the difference $c - c_b$, with $c_b = 3.2 \cdot 10^{-3}$. The difference $c_b - c_\infty$ can be considered, in absolute terms, due to the grain boundary contribution.

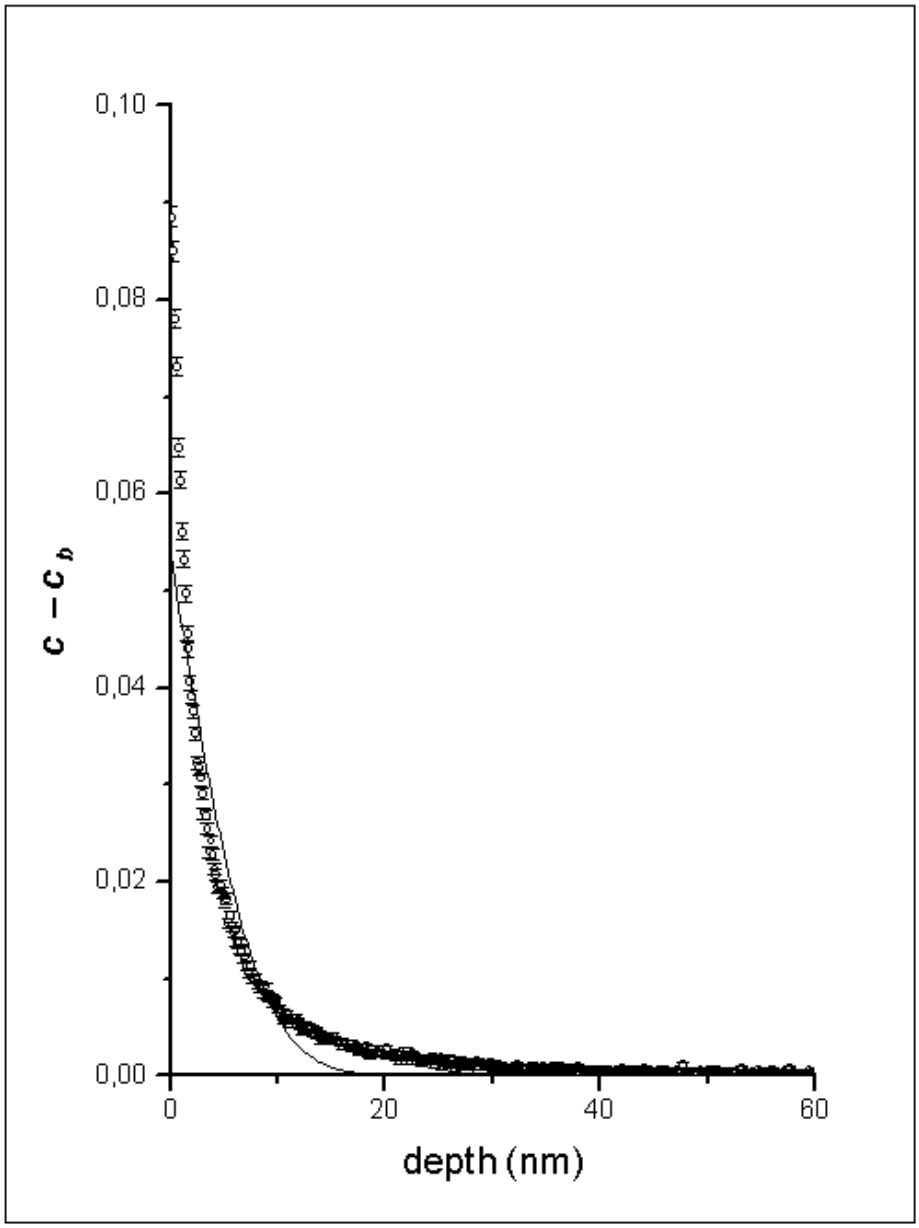

Figure 4.2-9: SIMS short-range depth profile on polycrystalline UO_2 in oxidising conditions (PC2). Least-square fit with Fick's second law (Equation 3.5.3-1).

The fit does not agree very well with the very first points of the profile. Nevertheless the value that can be calculated from the diffusion length given by the fit of the average profile is $D_L(\approx 25°C) = (2.5 \pm 0.1)\cdot 10^{-24}$ m^2/s, which is lower than that found for the single crystal at the same temperature and in better agreement with literature data.

The second part of the profile instead is shown in Figure 4.2-10, where the averaged profile is plotted in terms of the normalised isotopic ratio, $r(x) \equiv (c(x) - c_\infty)/(c_s - c_\infty)$, where x is the penetration depth, $c_\infty = 2.0\cdot 10^{-3}$ is the ^{18}O natural isotopic ratio and c_s is the ^{18}O concentration at the surface (*i.e.*, $c_s = c(0)$).

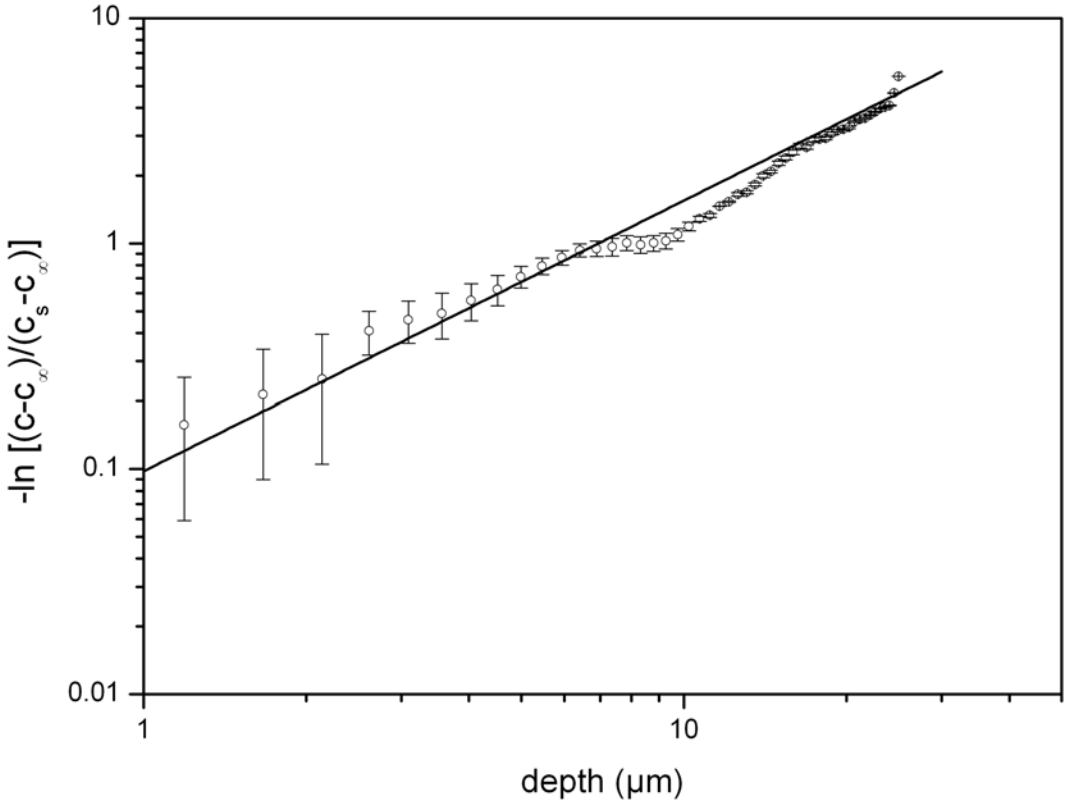

Figure 4.2-10: SIMS long-range depth profile on polycrystalline UO_2 (PC2) on log-log scale. Least-square fit with Levine-MacCallum's model (Equation 3.5.3-2).

Data fitting shows that the experimental curve is in good agreement with the behaviour foreseen by the Levine-MacCallum's model. In the log-log plot – *ln(I)* vs. *x* in Figure 4.2-10, the fitting curve (according to equation 3.5.3-2) is represented by a straight line of slope 6/5 and intercept α.

The quantity δD_B, product of the grain boundary diffusion coefficient and the inter-granular spacing can then be calculated, through the equation 2.2.5-12, using the value of α obtained from the fit ($\alpha = (2.000 \pm 0.002)\cdot 10^{-5}$ nm$^{-6/5}$) and the diffusion coefficient of the tracer in the lattice, D_L.
D_L can be obtained from extrapolation of literature data, and in this way the quantity $\delta D_B = (2.2 \pm 0.3)\cdot 10^{-24}$ m^3 s^{-1} can be calculated. A value of D_L was also obtained from the fitting of the first part of the profile: using this experimental value, the quantity $\delta D_B = (7.5 \pm 0.3)\cdot 10^{-24}$ m^3 s^{-1} can instead be calculated.
Taking grain boundary width $\delta = 1$ nm as mentioned earlier, the grain boundary diffusivity would be in the order of $D_B \approx 10^{-15}$ m^2/s.

Reproducibility of experiments

Not all experiments on polycrystalline UO_2 in oxidising conditions showed the same results, expecially as far as grain boundary diffusivity was concerned. The values of D_B obtained from the fit of the long-range profiles from different experiments were found to differ much more than the value of D_L obtained from the fitting of the short-

range profiles. Furthermore, in some cases the long-range profiles did not show any clear evidence of grain boundary diffusivity.

An example of this unexpected divergence from the trend observed in the other experiments is given by the sample named PC5. The short-range profiles acquired for this sample (Figure 4.2-11) showed a very uniform surface concentration, as the first points of the profile are characterised by a smaller uncertainty than in other cases. Furthermore, the fit by means of Fick's law provided a measure of the diffusion coefficient $D_L = (2.9 \pm 0.1) \cdot 10^{-24}$ m^2/s, in good agreement with the other experiments on similar matrices.

Nevertheless, both surface concentration and background concentration at the plateau (c_b) are much lower than the one found for previous experiments.

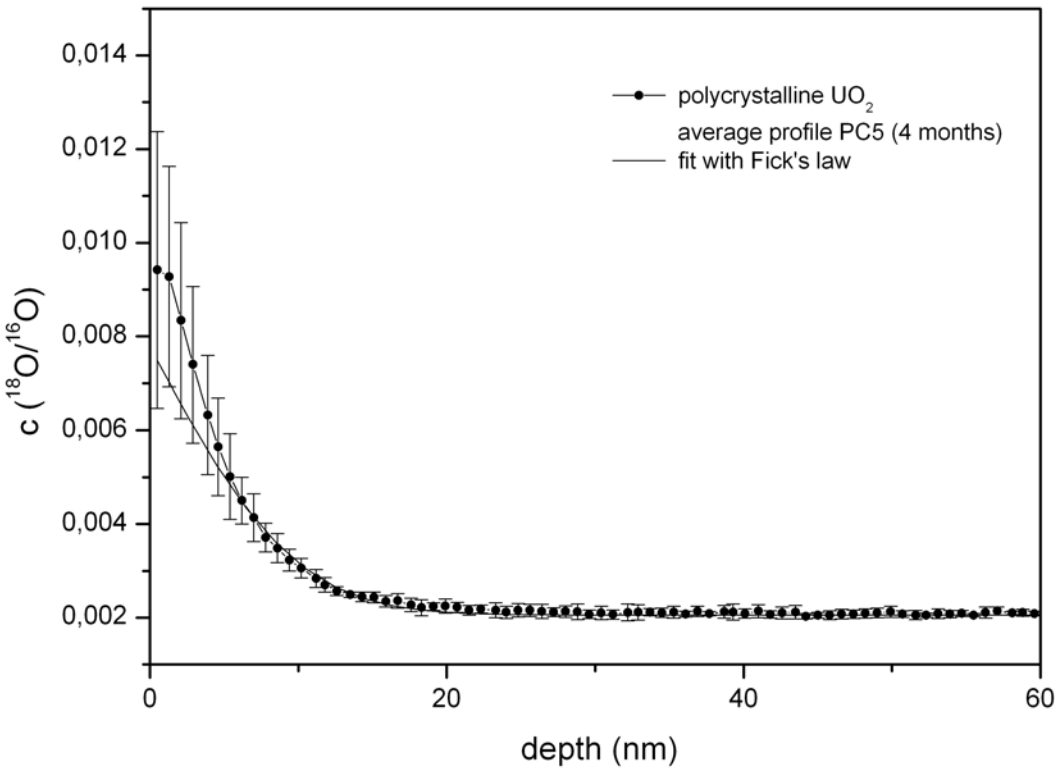

Figure 4.2-11: SIMS short-range profile on polycrystalline UO_2 after 4 months leaching in ^{18}O-labelled water. From fit with Fick's law a value $D_L = (2.9 \pm 0.1) \cdot 10^{-24}$ m^2/s is obtained.

In fact, the long-range profiles acquired on different points of the sample surface show that the tracer concentration decreases sharply within a few nm depth. As visible in Figure 4.2-12, a scale of less than 100 nm would be sufficient in this case to show the profile from the surface to the background represented by the natural abundance of ^{18}O in the sample.

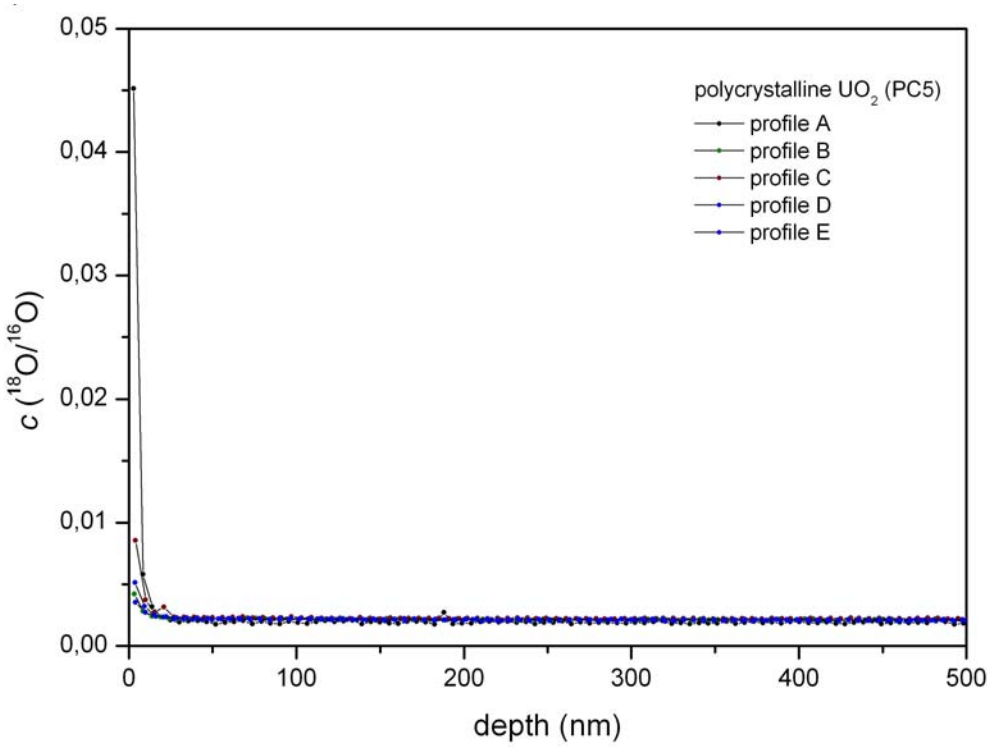

Figure 4.2-12: Different experimental profiles on polycrystalline UO_2 (PC5). Several profiles acquired in different points of the sample: the concentration drops fast and reaches a constant value within the first tens nm.

When the average long-range profile is shown, as in Figure 4.2-13, on a log-log scale in the form $-ln\ r$ vs. x, it becomes visible that the experimental points do not lie on the typical 6/5 slope line that can be considered the fingerprint of grain-boundary diffusion in the Levine-MacCallum's model. Only the very first part of the profile, roughly the first 100 nm, seems to agree with the model, but a mathematical fit of such a limited part of the profile would not be meaningful.

In Table 4.2-3, the diffusion coefficients determined from the profiles acquired on all polycrystalline samples are summarized. The value of D_L are consistently found in the range $D_L(25°C) = (2.0 \pm 1.0)\cdot10^{-24}$ m^2/s. Instead, the values of D_B obtained from the long-range profiles were found to differ significantly. As the quantity δD_B depends on D_L, in order to make the comparison more direct the D_B values in Table 4.2-3 have been calculated for the same value, $D_L = 2\cdot10^{-24}$ m^2/s.

Table 4.2-3: Diffusion coefficients obtained from experiments on polycrystalline UO_2

Sample	*Exp. Conditions*	*Contact-time (months)*	D_L *(m^2/s)*	*α (from fit)*	δD_B *(m^3/s)*	D_B *(m^2/s) (δ=1nm)*
PC1	Oxidising, ≈ 25; $H_2{}^{18}O$;	3	$(1.4 \pm 0.3)\cdot10^{-24}$	$8.41\cdot10^{-6}$	$1.5\cdot10^{-23}$	$1.5\cdot10^{-14}$
PC2		3	$(2.5 \pm 0.1)\cdot10^{-24}$	$2.00\cdot10^{-5}$	$2.2\cdot10^{-24}$	$2.2\cdot10^{-15}$
PC3		9	$(3.0 \pm 0.2)\cdot10^{-24}$	$2.70\cdot10^{-3}$	$3.2\cdot10^{-26}$	$3.2\cdot10^{-17}$
PC5		4	$(2.9 \pm 0.1)\cdot10^{-24}$	n.d.	n.d.	n.d.

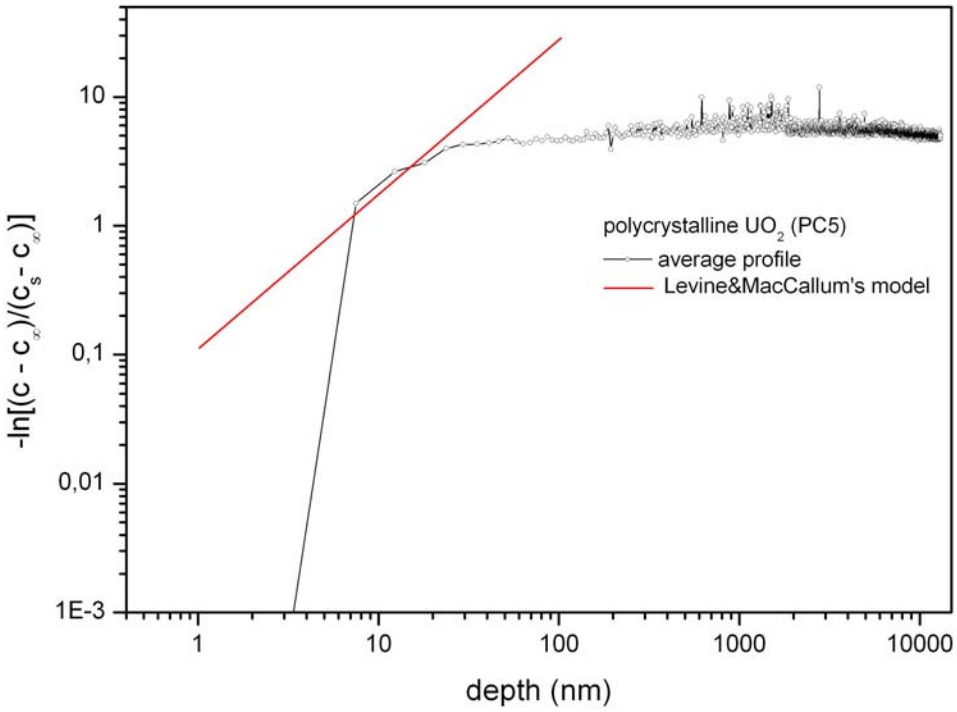

Figure 4.2-13: Average long-range profile on polycrystalline UO_2 (PC5). On a log-log scale, the points diverge evidently from the Levine-MacCallum's model (here represented by the 6/5 slope fitting curve), showing no clear evidence of grain boundary diffusivity.

Even if the experiments summarized in Table 4.2-3 were carried out in the same experimental conditions (except for the duration of the experiment), the different findings about grain boundary diffusivity might depend on aspects that were not under control and indeed affected the reactivity of the different samples. For example, it is to be noted that the oxygen partial pressure was not constant and could not be controlled, even though it has been reported that in air environment UO_2 oxidation kinetics depends little on oxygen partial pressure [45]. Other possible differences lie on the surface preparation, since the result of the polishing is not reproducible on a nm-to-µm scale. The most important aspect to keep in mind, though, is the stoichiometry of the surface. Even if after annealing the stoichiometry of the pellet was confirmed by TGA, the state of the surface might be an entirely different matter. For the first experiments (PC1 to PC3) the pellet was transferred into the solution several hours after annealing while for PC5 this time was reduced to a few minutes. This might have significantly reduced the pre-oxidation of the surface (and the grain boundaries) and might be the reason why the uptake of tracer is for this sample so much lower than for the previous ones. In fact, the concentration on the surface alone decreased from 0.1 - 0.2 of the first samples to 0.04 - 0.01 of PC5.

4.2.3 SIMFUEL

SIMS analysis of SIMFUEL showed large spot-to-spot differences, both in terms of surface concentration and profile shape (Figure 4.2-14). In general, the ^{18}O

concentration in this matrix reached the natural abundance at a much shallower depth than in the case of polycrystalline UO_2 (Figure 4.2-10), notwithstanding the leaching time was twice as long.

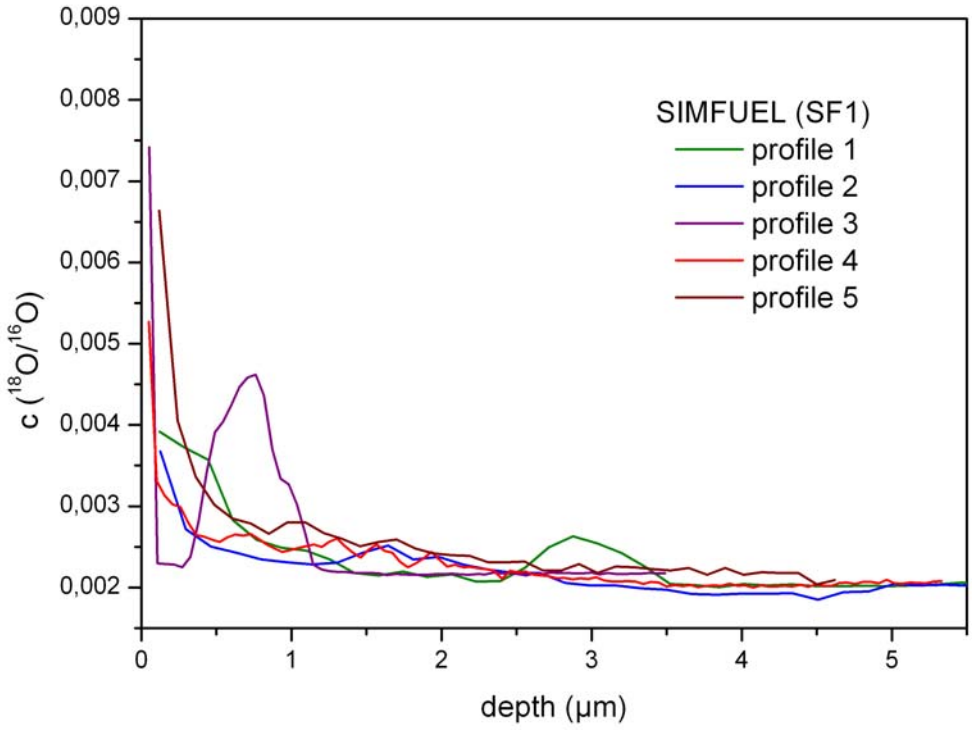

Figure 4.2-14: SIMS long-range profiles acquired on different spots of a sample of SIMFUEL 8% after 6 months leaching in ^{18}O-labelled water.

Many of the profiles presented ripples that seem to be the result of local perturbations of the diffusion phenomenon. For this reason, as the profiles could not be fitted by means of the Levine-MacCallum's model or by any other available diffusion model, an evaluation of the diffusion coefficient in this case could not be obtained. These ripples and the fact that profiles acquired on different areas of the same surface present a large variability, cannot be reasonably due to the presence of the analogues of fission products contained in the SIMFUEL matrix. In fact, these compounds are homogeneously distributed in the UO_2 matrix on a µm scale. Each SIMS crater sample an area of 150 x 150 µm^2 and several µm in depths, thus ensuring that statistically each profile would be affected by a similar amount of added metal particles and oxides.

Another aspect to be considered in this respect is represented by matrix effects, which can significantly affect the quantification of an element by SIMS. Matrix effects have indeed been reported for SIMFUEL [110]. Nevertheless, as far as the oxygen isotopic ratio is concerned, the analysis of blank samples showed that the ^{18}O/^{16}O ratio was stable in depth and reproducible in different spots of the surface. For this reason, it does not seem possible that the presence of ripples in the profiles could be due to a matrix effect.

In principle, the reduced tracer penetration could be related to the observed role of Mo particles along the grain boundaries in spent fuel [92], where the oxidation potential is controlled by the oxidation of Mo to MoO_2 [111]. However, as these intragranular precipitates are supposed to be uniformly distributed on the µm-scale, this hardly explains the spot-to-spot variability.

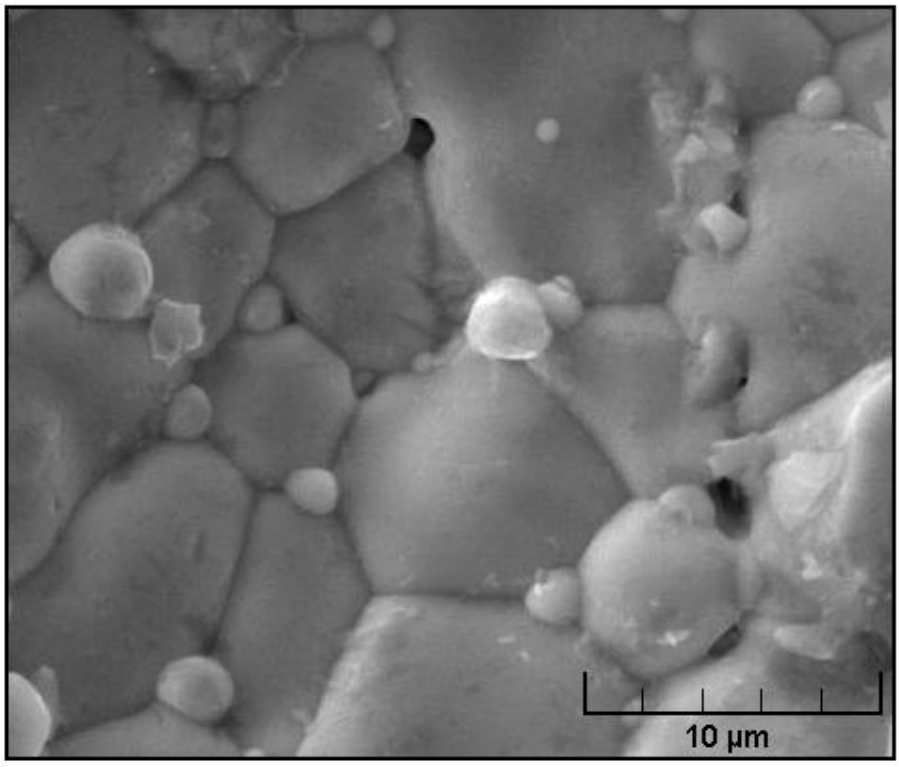

Figure 4.2-15: SEM image of a SIMFUEL 8% slice. The metallic particles added to the UO_2 matrix are visible at the grain-boundaries.

The characterisation by means of Scanning Electron Microscopy and Energy-dispersive X-ray detector (SEM-EDX) of a non-leached slice of the same SIMFUEL batch used for SIMS experiment showed an unexpected presence of Fe particles precipitated along the grain boundaries, typically together with Pd particles (Figure 4.2-16). These Fe particles appeared to be concentrated mostly in a part of the sample, as visible in Figure 4.2-17. This could explain the ripples, as Fe particles would be preferentially oxidised than the nearby matrix. Their origin could be in the production process of SIMFUEL. The total Fe content in the SIMFUEL matrix that can be determined by ICP-MS analysis was probably not considered like a significant contamination [92], but each particle can determine a significant perturbation, locally. SIMS ion maps (Figure 4.2-17) were used to compare the distribution of Fe with the other grain boundary precipitates, namely Pd and Ba. These ion maps show that, while perovskite-type crystals (represented by Ba) are uniformly distributed, the Fe contamination presents a hot spot, which is accompanied by a locally higher abundance of Pd.

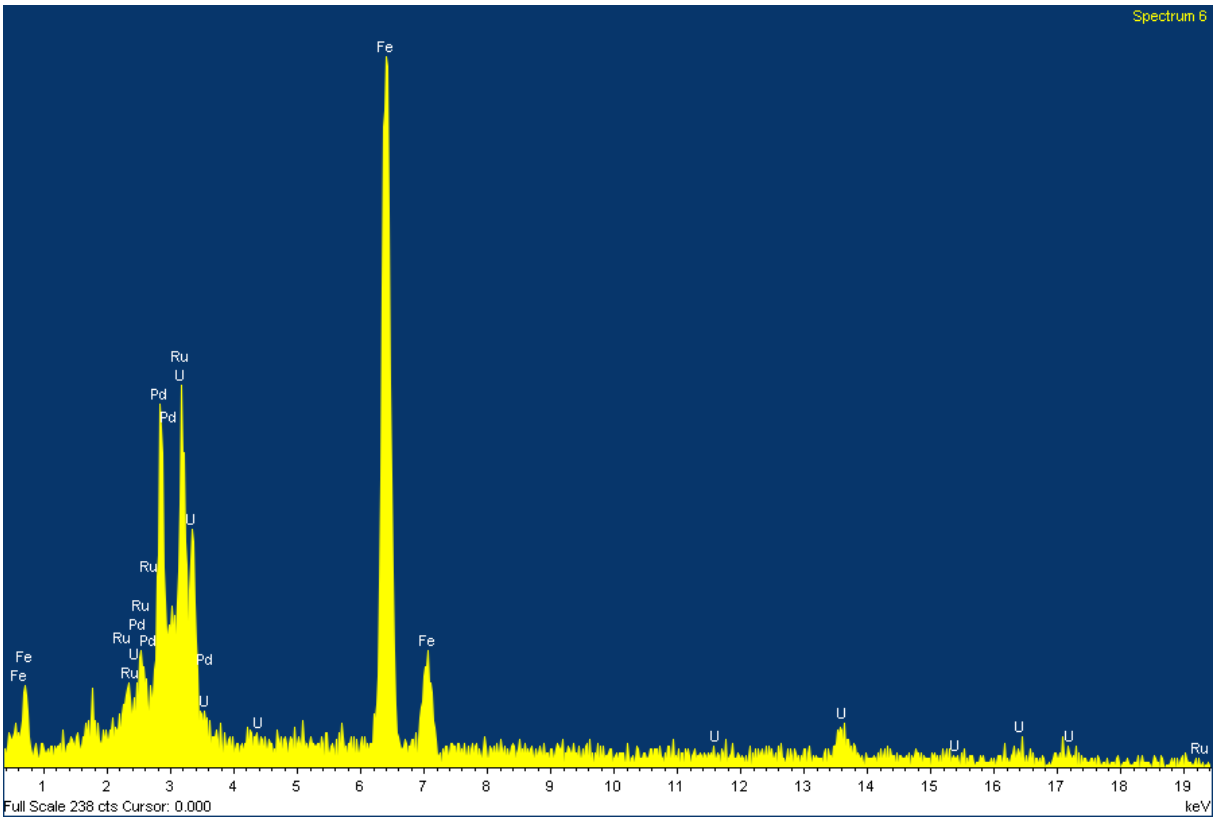

Figure 4.2-16: EDX spectrum acquired on one of the metallic particles visible on the surface of a SIMFUEL 8% sample, like shown in Figure 4.2-15

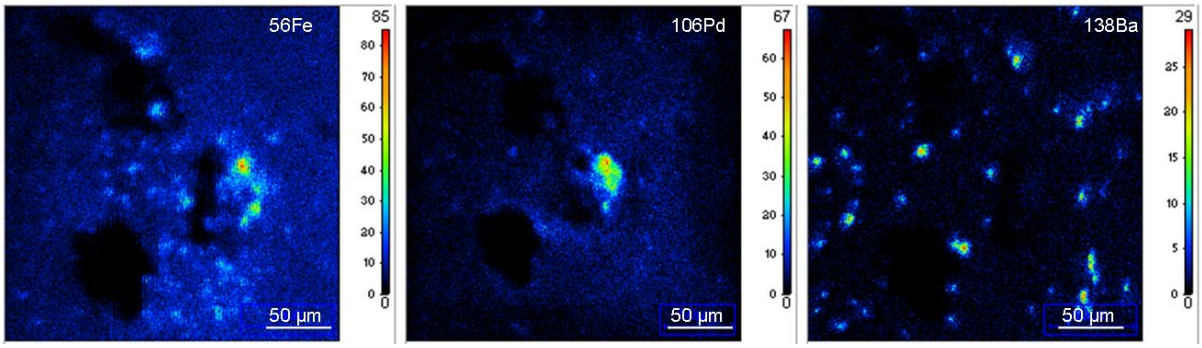

Figure 4.2-17: SIMS ion mapping showing distribution of Fe, Pd and Ba on the surface of a SIMFUEL 8% sample.

For the same reason also the evaluation of the lattice diffusion coefficient from the short-range profiles could not be considered reliable. However, a few spots on the surface provided profiles more similar to the classical fickian diffusion profile. Fitting such profiles by means of Fick's law provided a value of diffusion coefficient slightly higher than what found on the polycrystalline UO_2 pellets leached in similar conditions (see previous paragraph). In Figure 4.2-18 one of these profiles is shown, from which the value $D_L = (6.8 \pm 0.1) \cdot 10^{-24}$ m^2/s could be obtained.

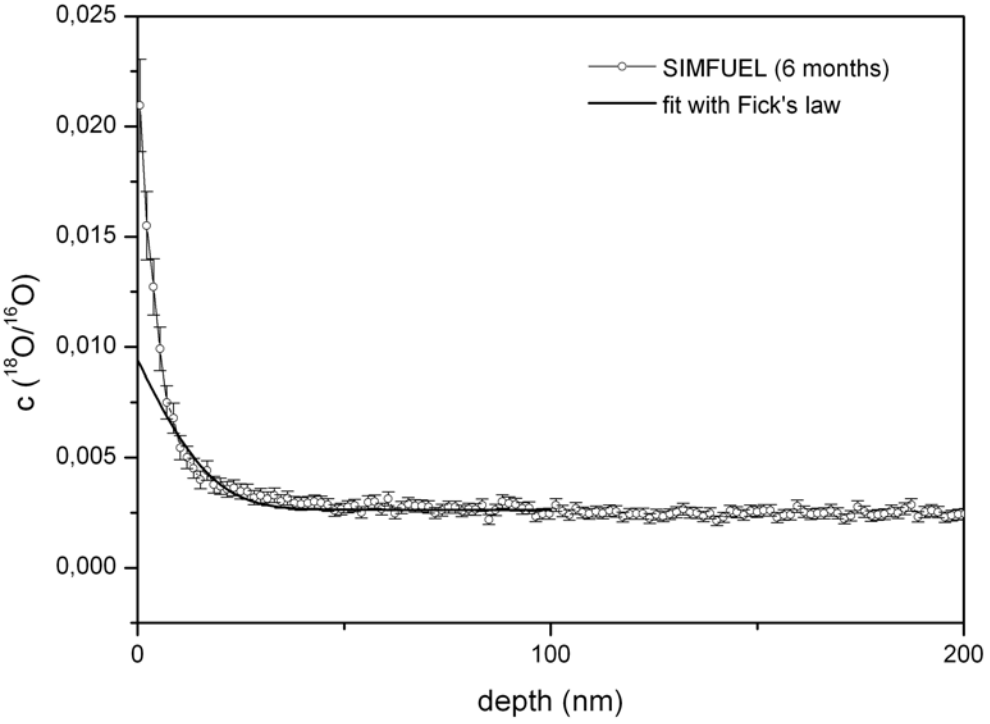

Figure 4.2-18: Short-range diffusion profile obtained on a spot of the surface of the SIMFUEL 8% sample (SF1). Fit with Fick's law yielding a value of $D_L = (6.8 \pm 0.1)\cdot10^{-24}$ m^2/s.

4.2.4 Experiments in carbonated water

Corrosion experiments in ^{18}O-labelled water containing carbonate, under oxidative conditions, were carried out to study the influence of the UO_2^{2+} carbonate complexation on the ^{18}O/^{16}O profiles. This set of experiments, as summarised in Table 4.2-4, involved the three UO_2 matrices: single-crystal UO_2, polycrystalline UO_2 and SIMFUEL.

Table 4.2-4: summary of the most significant corrosion experiments carried out in oxidising conditions carried out for the present study.

Sample	*UO_2 matrix*	*Vial*	*Leachant*	*Temp.*	*Contact-time (months)*	*[^{238}U] (M)*
PC5	Polycrystalline	PE	H_2 ^{18}O (98%)	≈ 25	4	$(1.9 \pm 0.6)\cdot10^{-7}$
PCCO3			H_2 ^{18o} (98%) 2mM $NaHCO_3$ 10mM NaCl			$(1.2 \pm 0.3)\cdot10^{-5}$
SFCO3	SIMFUEL 8%					$(4.3 \pm 0.1)\cdot10^{-8}$
SCCO3	Single-crystal					$(9.7 \pm 0.2)\cdot10^{-7}$

These experiments were carried out under the same conditions. The only difference is the absence of carbonate for one of the polycrystalline UO_2 samples (PC5). ICP-MS analysis of the leachate showed, as expected, that dissolution of UO_2 in presence of carbonate increases. A comparison of the two polycrystalline UO_2 samples leached in absence or presence of carbonate, shows that the uranium concentration differ of roughly two orders of magnitude. Polycrystalline UO_2 corrodes faster than single-crystal UO_2 in presence of carbonates, while SIMFUEL shows the slowest corrosion rate.

Depth profiles of the ^{12}C- and ^{18}O-isotopes were acquired for each sample and are shown in the following figures (PC5 in Figure 4.2-19, PCCO3 in Figure 4.2-20, SFCO3 in Figure 4.2-21 and SCCO3 in Figure 4.2-22). The ^{12}C and ^{18}O signals were normalized, point by point, to the ^{16}O signal. These normalized values are not quantitative, as the absolute concentration of ^{18}O and ^{12}C in the matrix can be measured by SIMS only determining the relative sensitivity factors with a proper calibration (see Sect. 3.5.1). Nevertheless, it is possible to compare qualitatively curves of different elements once normalised vs. the signal of the same matrix component and it is possible to compare directly curves of the same element in different samples if they are measured under identical conditions, as in this case.

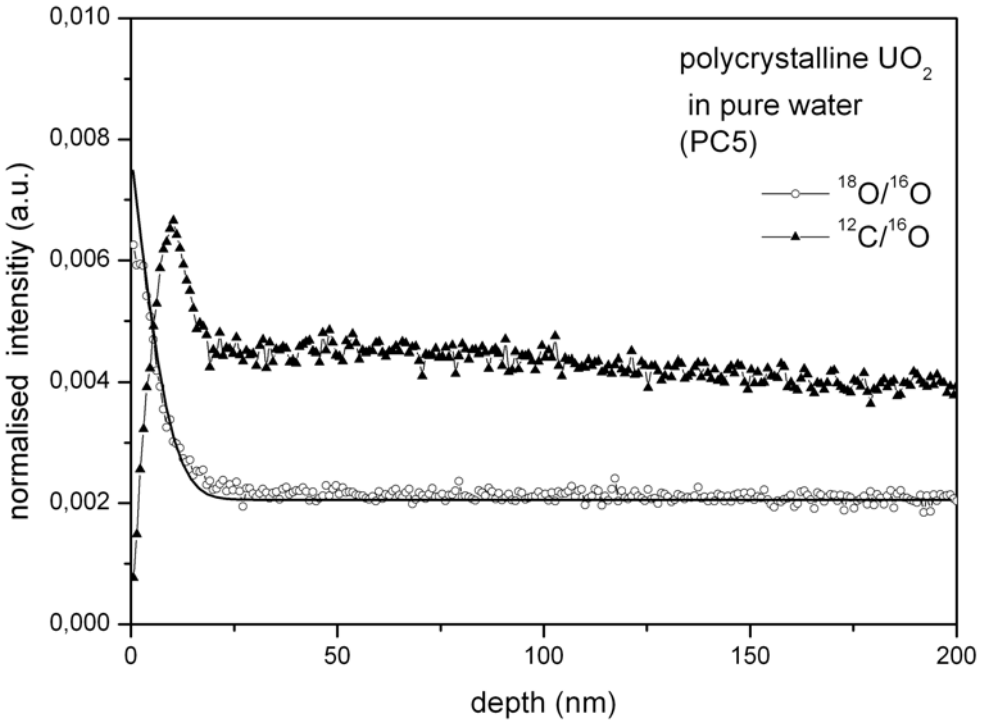

Figure 4.2-19: Polycrystalline UO_2 in pure water (PC5). A diffusion coefficient $D_L = (3.1 \pm 0.1)\cdot 10^{-24}$ m^2/s was obtained from this fit.

It is possible to observe that carbon is much more abundant, as expected, on the surface of the pellet exposed to carbonate water (Figure 4.2-20) but it is however present on the other surface as well (Figure 4.2-19). In fact carbon is present as a contaminant of the UO_2 sample itself and of the solution, which has an estimated

CO_3^{2-} content of 10^{-8} M due to atmospheric CO_2 dissolution. Furthermore, carbon is an unavoidable contamination of the surface of any solid sample analysed by SIMS or other ultra-high vacuum technique: hydrocarbons resulting from the presence of oils are in fact present in the sample chamber.

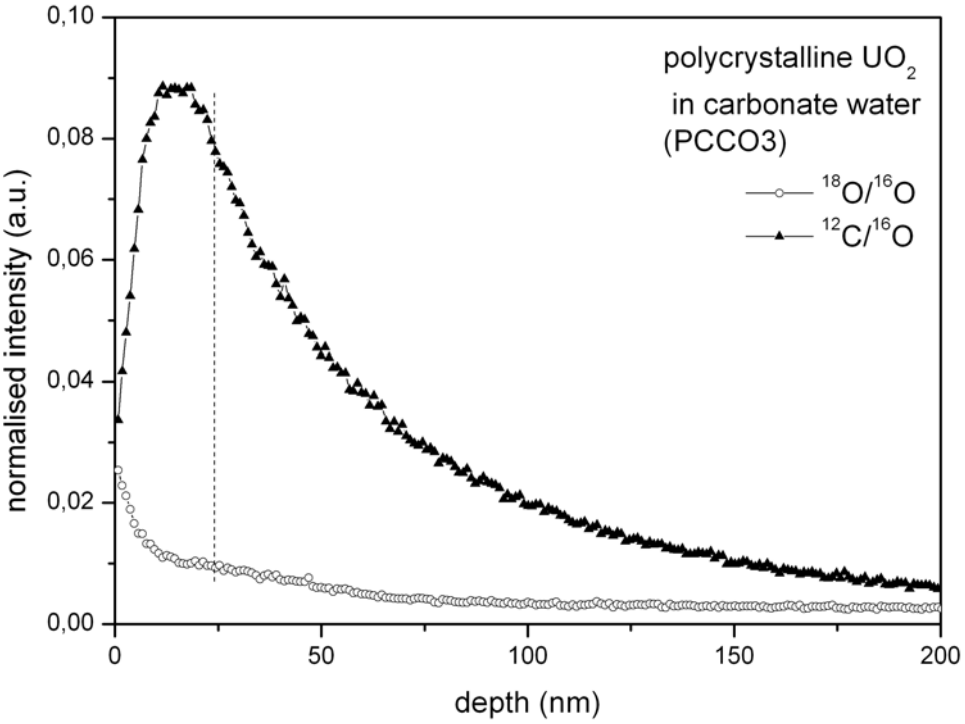

Figure 4.2-20: Polycrystalline UO_2 in carbonate water (PCCO3). A carbonate phase is deposited on the surface. Larger dissolution of UO_2 by comparison with the no carbonate case is confirmed by ICP-MS: an estimated 20 nm-thick layer was dissolved.

The $^{18}O/^{16}O$ profile obtained in absence of carbonate in the leachant (Figure 4.2-19) was fitted by means of Fick's law and a diffusion coefficient of $D_L = (3.1 \pm 0.1)\cdot 10^{-24}$ m^2/s. In carbonate containing solution, the $^{18}O/^{16}O$ profile exhibited a composite shape, indicating two different diffusion curves, as shown in (Figure 4.2-20). As emphasised by the dashed vertical line in Figure 4.2-20, the transition between the two curves matches the onset of the decreasing part of the $^{12}C/^{16}O$ profiles. This indicates the presence of a carbon-rich phase on the surface and the UO_2 bulk that is compatible with a carbonate phase. In fact, XPS analysis has confirmed the presence of a thin carbonate phase, probably chemisorbed (no more than one atomic layer) on all samples that had been exposed to carbonate solution. Fitting only the second part of the profile, the diffusion coefficient $D_L = (1.9 \pm 0.2)\cdot 10^{-23}$ m^2/s can be determined. This value matches what found for single-crystal in the room temperature experiment (SC1).

It is also important to mention that the sputter rate used to convert the time to depth scale has been determined specifically for UO_2 and might differ from the sputter rate of phases with a different composition. In order to determine the sputter rate in this surface phase, a calibration would need to be performed on a sample of identical

composition. Furthermore, one should keep in mind that the two experiments have reached different depths from the original surface of the sample. Considering ICP-MS data (see Table 4.2-4), the geometry of the sample and the volume of the solution, we can consider that in the case of the carbonate solution the thickness of the dissolved layer was ≈ 20 nm, while in the case in which no carbonate was added it was ≈ 2 nm.

The experiment on single-crystal UO_2 (SCCO3) produced a UO_2 surface mostly covered by a visible layer, similarly to single-crystal samples exposed to solutions containing virtually no carbonate but higher in silicate concentration (SC60 and SC1). The $^{18}O/^{16}O$ profiles acquired in the areas that resulted covered showed a "two-step" shape like already observed for other samples. SIMS ion maps showed a distribution of the ^{12}C intensity that matched perfectly the contour of the covered area and verified that a carbonate phase was present, but not as homogeneously distributed as in the case of polycrystalline UO_2 (PCCO3). SIMS depth profiles acquired in the areas of the samples that appeared covered by the carbonate phase showed a larger value of diffusion coefficient, $D_L = (1.06 \pm 0.02)\cdot10^{-23}$ m^2/s. The profiles acquired on the areas of the surface that appear to be free from the carbonate layer show a normal fickian ^{18}O-diffusion profile. The fit of this kind of profile, as shown in Figure 4.2-21, provides the diffusion coefficient $D_L = (1.1 \pm 0.1)\cdot10^{-24}$ m^2/s.

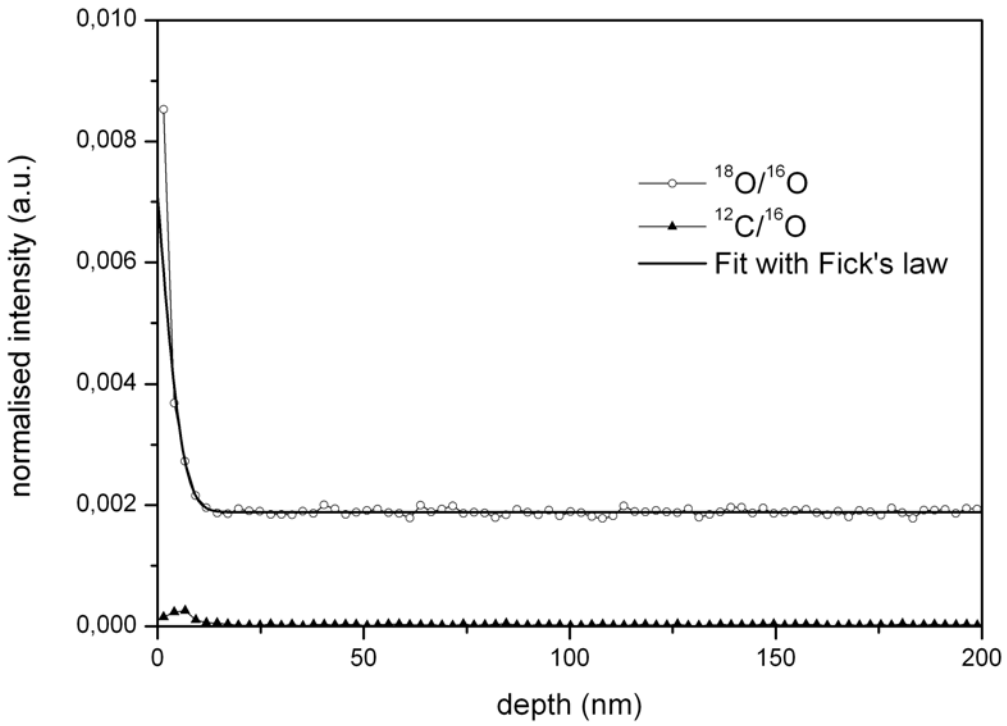

Figure 4.2-21: Single-crystal in carbonate water (SCCO3). Profile acquired on the part of the surface free from carbonated deposited phase. The diffusion coefficient $D_L = (1.1 \pm 0.1)\cdot10^{-24}$ m^2/s was obtained from the fit.

SIMS depth profiling of SIMFUEL did not show the same features than in the case of leaching in water without carbonate, but again no clear sign of grain boundary

diffusivity could be found. The analysis of the short-range profiles showed only one-step profiles that could be fitted by means of the solution of Fick's law giving an average value of $D_L = (6.7 \pm 0.3) \cdot 10^{-24}$ m^2/s. This value is very similar to what obtained from the SIMFUEL sample leached in absence of carbonate (SF1).

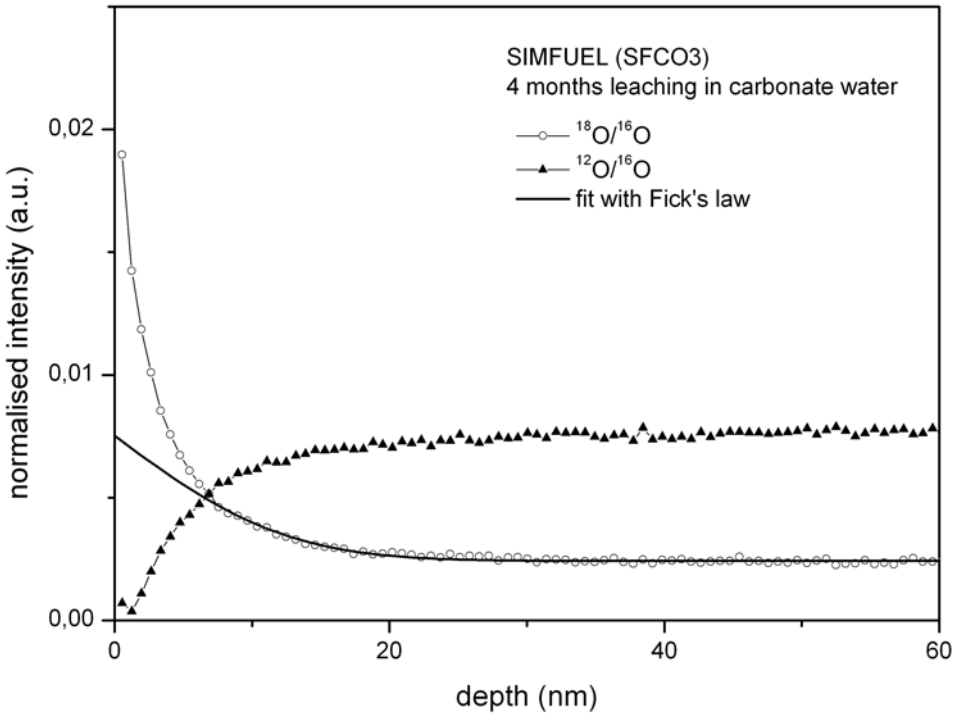

Figure 4.2-22: SIMFUEL in carbonate water (SFCO3). From the fit of the oxygen profile $D_L = (6.7 \pm 0.3) \cdot 10^{-24}$ m^2/s is obtained. The ^{12}C profile shows simply the background concentration of this material.

It is also important to note that for SFCO3 the "two-step" shape seen for PCCO3 was not visible. The $^{12}C/^{16}O$ profile is also different from PCCO3 where a clear decrease was seen within the same nominal depth.

4.3 Experiments in autoclave (reducing conditions)

4.3.1 Dissolution

The autoclave set-up was aimed at obtaining reducing conditions in four different vessels for simultaneous experiments on different UO_2 matrices. As described in the experimental section, only the top vessel was disposed for regular samplings (roughly every 2 months), and for this reason this vessel could host a larger volume of solution. ICP-MS analysis of the sampled leachates showed that the concentration of uranium in solution decreased during the six months of the experiments and more significantly during the first two months, indicating that reduction of dissolved U(VI) was taking place (Table 4.3-1).

Table 4.3-1: Summary of ICP-MS results from sampling of the top vessel solution.

Sample	*UO_2 matrix*	*Leachant*	*Contact-time (months)*	*P (atm)*	*$[^{238}U]$ (M)*
PCA	Polycrystalline	H_2 ^{18}o (98%) 2mM $NaHCO_3$ 10mM NaCl	0*	10.2	$(5.53 \pm 0.34)\cdot10^{-9}$
			2	10	$(1.29 \pm 0.39)\cdot10^{-9}$
			4	9.8	$(2.19 \pm 0.65)\cdot10^{-9}$
			6	9.2	$(9.65 \pm 0.27)\cdot10^{-10}$

*The leachate was sampled after 1 hour from the pressurisation of the autoclave.

At the end of the experiment, after six months, the solutions contained in all four vessels were sampled and ICP-MS analysis showed much higher uranium concentrations for the experiments carried out in the three smaller vessels (see Table 4.3-2).

Table 4.3-2: Summary of ICP-MS analysis of the four final solutions, after 6 months leaching in autoclave.

Sample	*UO_2 matrix*	*Vol. (mL)*	*Leachant*	*Temp.*	*Contact-time (months)*	*$[^{238}U]$ (M)*
PCA	Polycrystalline	15	H_2 ^{18}o (98%) 2mM $NaHCO_3$ 10mM NaCl	≈ 25	6	$(9.65 \pm 0.27)\cdot10^{-10}$
PCB		5				$(1.63 \pm 0.03)\cdot10^{-6}$
SCC	Single-crystal	5				$(2.72 \pm 0.08)\cdot10^{-7}$
SFD	SIMFUEL 8%	5				$(4.42 \pm 0.06)\cdot10^{-10}$

This difference cannot be explained simply by the different reactivity of different matrices because the two identical polycrystalline UO_2 slices showed the most striking difference between them: the slice placed in the top vessel and one in a lower one had a difference of four orders of magnitude, confirmed by several independent analyses. Also the possible presence of particles or fragments in solution, that could

have been dissolved once the solution was acidified for ICP-MS analysis, was excluded by the fact that three different filtration were applied to the solution before ICP-MS analysis, yielding the same result. The most likely explanation is that, at the start of the experiment, the lower vessels contained some trapped oxygen, both dissolved in the leachant and in the empty volume above the liquid. In fact, only the solution in the top vessel, the only one reached by the dip-tube, could be purged with H_2, thus eliminating dissolved O_2. Furthermore, during the purging of the autoclave and before pressurisation to 10 bar, the oxygen-containing atmosphere trapped in the lower vessels might not have been efficiently exchanged with the H_2 gas through the small ventilation openings in the peek vessels and the thin gap between the vessels and the internal wall of the autoclave.

4.3.2 Single-crystal

In the case of the single-crystal UO_2 (denominated SCC) the presence of a secondary phase covering part of the surface was visible, with remarkable similarity with what was observed for all the other single-crystal UO_2 samples leached in presence of carbonate or silicate. Depth profiles acquired within or outside this secondary phase covering area showed clearly different shapes and Figure 4.3-1 shows four of these profiles.

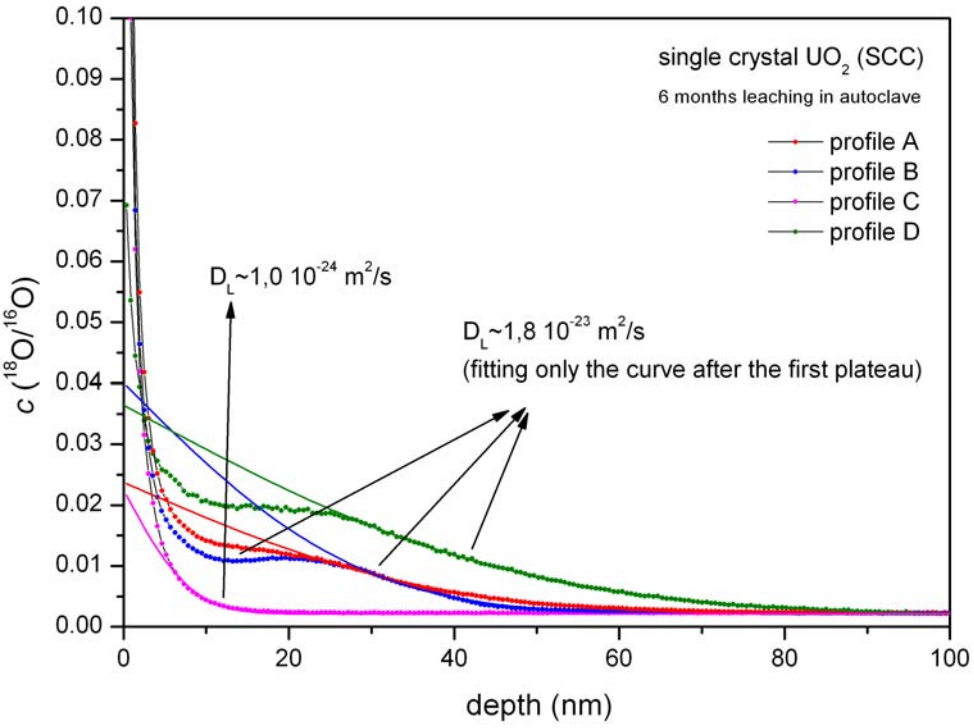

Figure 4.3-1: examples of profiles acquired on single crystal UO_2 after 6 months leaching in autoclave in ^{18}O-labelled carbonate water (SCC). Three of the profiles (A, B and D) present a "two-step" feature: the fit of the second part of these profiles gives an average value of D_L one order of magnitude higher than the D_L obtained from the fitting of the one-step profile.

Three of these profiles (acquired within the "covered" area of the sample) showed the "two-step" profile and the fit of the deeper curve made it possible to estimate an average D_L = 1.8·10^{-23} m^2/s. This D_L value is similar to what was measured under oxidising conditions on areas that resulted covered by a secondary phase. From the fit of profile acquired on the "clear" surface I a diffusion coefficient roughly one order of magnitude lower, D_L = 1.0·10^{-24} m^2/s was found, also in agreement with previous experiments performed under oxidising conditions in absence of complexing agents.
On the basis of these findings and the ICP-MS analysis results, the conditions under which the single-crystal slice SCC was leached can be considered to have been oxidising despite the presence of H_2.

4.3.3 Polycrystalline UO_2

The two polycrystalline samples corroded in autoclave under 10 bar H_2 at room temperature (denominated PCA and PCB) that have showed different dissolution behaviour, shown also very different diffusion profiles in the near-surface area. The short-range profiles acquired on PCA and PCB, are given Figure 4.3-2 and Figure 4.3-3, respectively. In both cases, the $^{18}O/^{16}O$ and $^{12}C/^{16}O$ profiles are plotted.

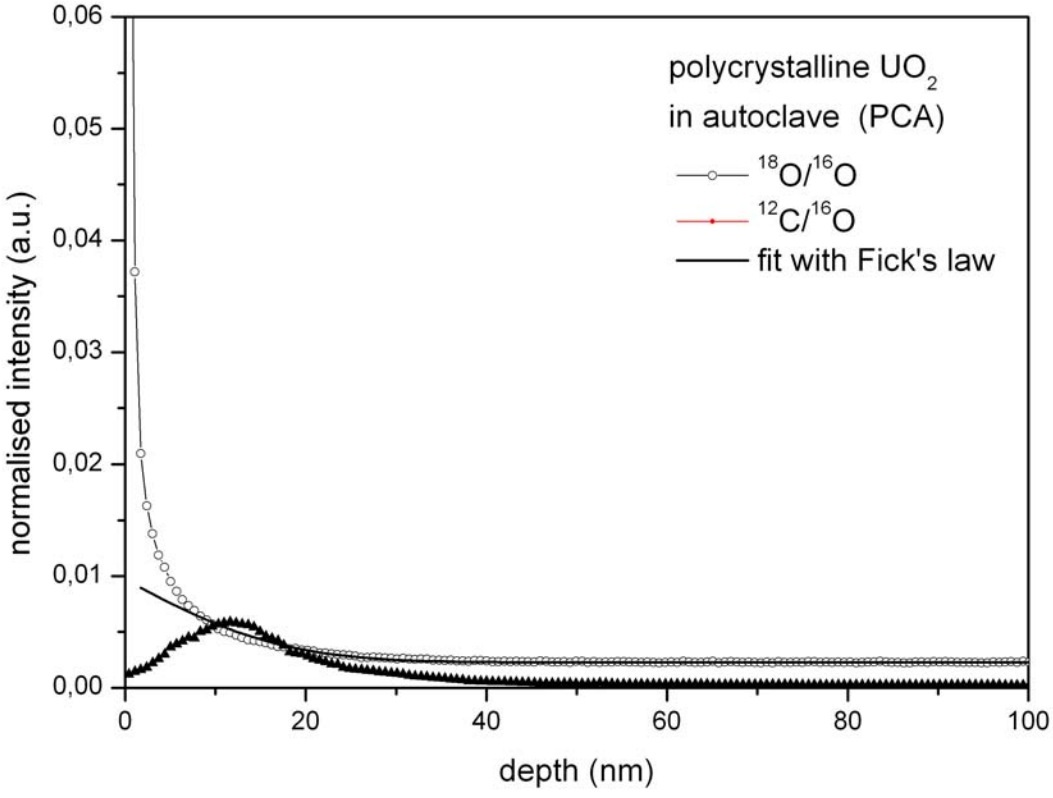

Figure 4.3-2: Polycrystalline UO_2 leached in autoclave (PCA). Average SIMS profiles acquired for ^{18}O and ^{12}C (both normalised vs. ^{16}O intensity). From the fit of the second part of the profile, the diffusion coefficient is determined as D_L = (6.4 ± 0.1)·10^{-24} m^2/s.

The polycrystalline sample that had showed a lower U concentration in the leachate (PCA) is characterised by a high ^{18}O-tracer concentration on the surface. It can be seen that the $^{18}O/^{16}O$ curve exhibits a typical ^{18}O-diffusion profile: only one diffusion curve is visible and the diffusion coefficient $D_L = (6.4 \pm 0.1)\cdot10^{-24}$ m^2/s can be determined from the fit according to Fick's law. This D_L value has no match among the other polycrystalline UO_2 samples, in any experimental conditions, but is very similar to what determined in the case of SIMFUEL samples.

For the short-range profiles acquired on PCB (Figure 4.3-3), instead, a "two-step" feature is recognized in the ^{18}O-profile. The $^{12}C/^{16}O$ profile indicates a larger presence of carbon on the surface than for PCA. The peak of the $^{12}C/^{16}O$ distribution matches the first step of the ^{18}O profile (dashed line), as it had been found for similar samples in carbonate water in oxidising conditions (sample PCCO3). Also the D_L obtained by fitting the second part of the profile by means of the solution of Fick's law is very close to the value obtained for PCCO3: $D_L = (2.21 \pm 0.02)\cdot10^{-23}$ m^2/s.

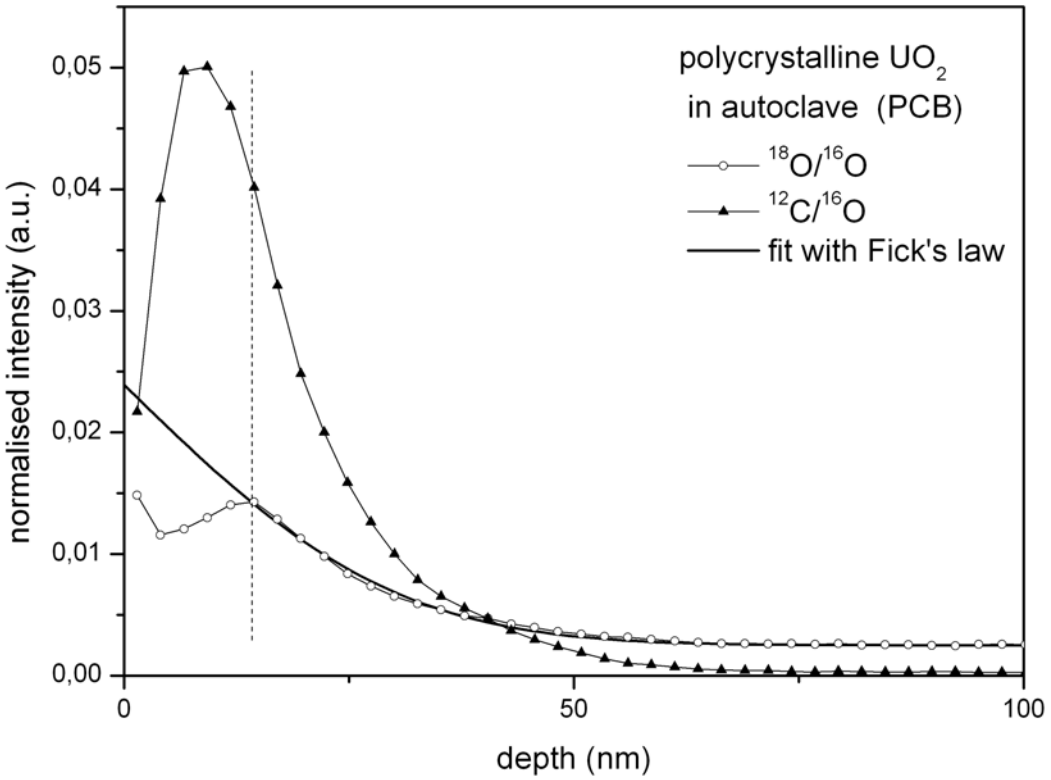

Figure 4.3-3: Polycrystalline UO_2 leached in autoclave (PCB). Average SIMS profiles acquired for ^{18}O and ^{12}C (both intensities normalised vs. ^{16}O) on polycrystalline sample after 6 months leaching in autoclave. The oxygen profile shows the "two-step" shape matching the presence of a carbonate phase on the surface (dashed line). From the fit of the second part of the profile, the diffusion coefficient is determined as $D_L = (2.21 \pm 0.02)\cdot10^{-23}$ m^2/s.

By the comparison of these profiles together with the ICP-MS analysis already discussed it is possible to draw the conclusion that PCA was exposed to reducing conditions while PCB to an oxidising environment. The amount of dissolved U(VI) that initially produced by the surface oxidation of PCA at the beginning of the experiment, might have been reduced to U(IV) by the effect of H_2 and precipitated as

$U(OH)_4$ (aq) → UO_2 (s) + $2H_2O$

In this precipitation reaction, ^{18}O is increasingly introduced in the precipitated layer, but not from a strictly diffusive process: this can explain the higher ^{18}O content of the most superficial points of the profiles, which are not well fitted by the Fick's law equation (Figure 4.3-2). This also explains the lower amount of carbonate on the surface compared to PCB.

Despite the different dissolution and near-surface diffusion behaviour, the two polycrystalline samples PCA and PCB present instead very similar long-range profiles. In both cases no clear indication of grain boundary diffusion is visible. In Figure 4.3-4 the average profiles obtained on both polycrystalline samples are shown on a log-log scale plotting $-\ln[(c(x)-c_\infty)/(c_s-c_\infty)]$ vs. x. Two dashed lines in Figure 4.3-4 do not represent a fitted curve but are used to indicate the trend that the two profiles would have followed if they had been expressing a grain-boundary diffusivity, according to the 6/5 slope indicated by the Levine-MacCallum's model.

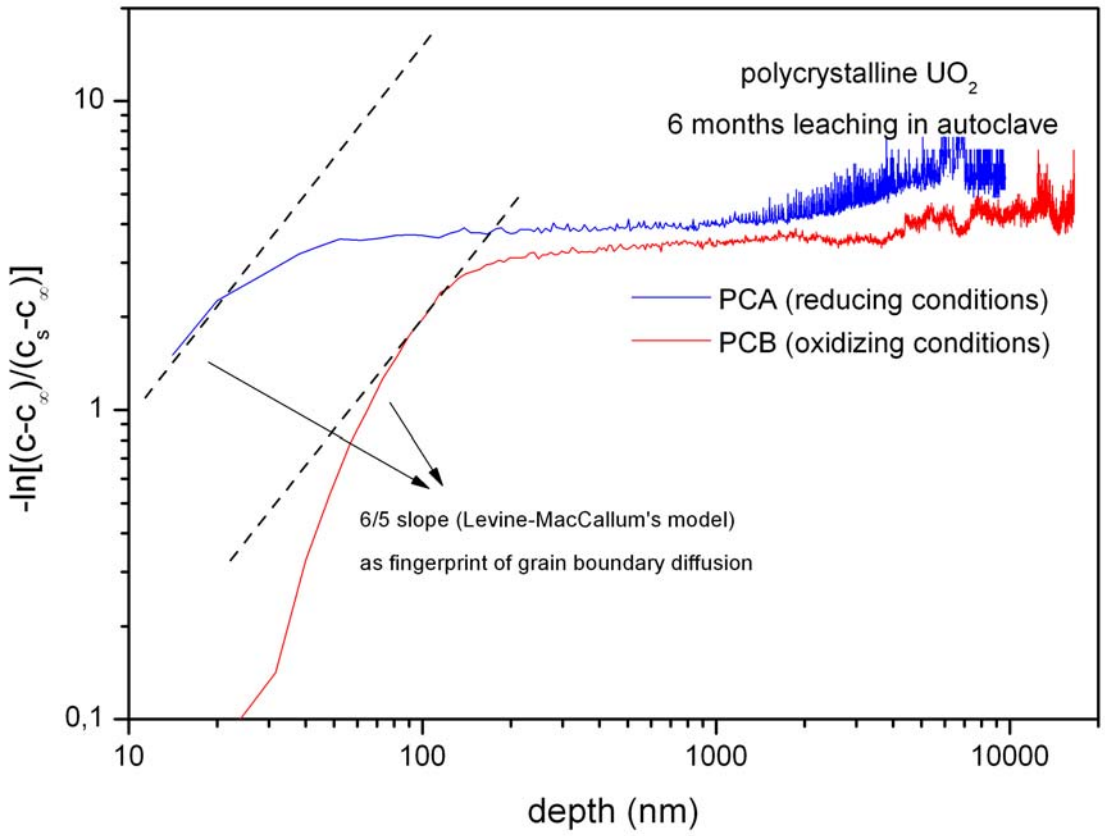

Figure 4.3-4: Profiles of polycrystalline UO_2 samples leached in autoclave (10 bar H_2). The representation on a log-log scale of long-range profiles shows in both cases no agreement with the grain-boundary diffusion model.

4.3.4 SIMFUEL

Short-range depth profiles on SIMFUEL showed the presence of a "two-step" $^{18}O/^{16}O$ profile. The plateau after the first curve matches the peak of the carbon distribution, as visible in Figure 4.3-5. Fitting the second part of the oxygen profile by means of the solution of Fick's second law, a diffusion coefficient of $D_L = (5.42 \pm 0.03) \cdot 10^{-23}$ m^2/s is obtained.

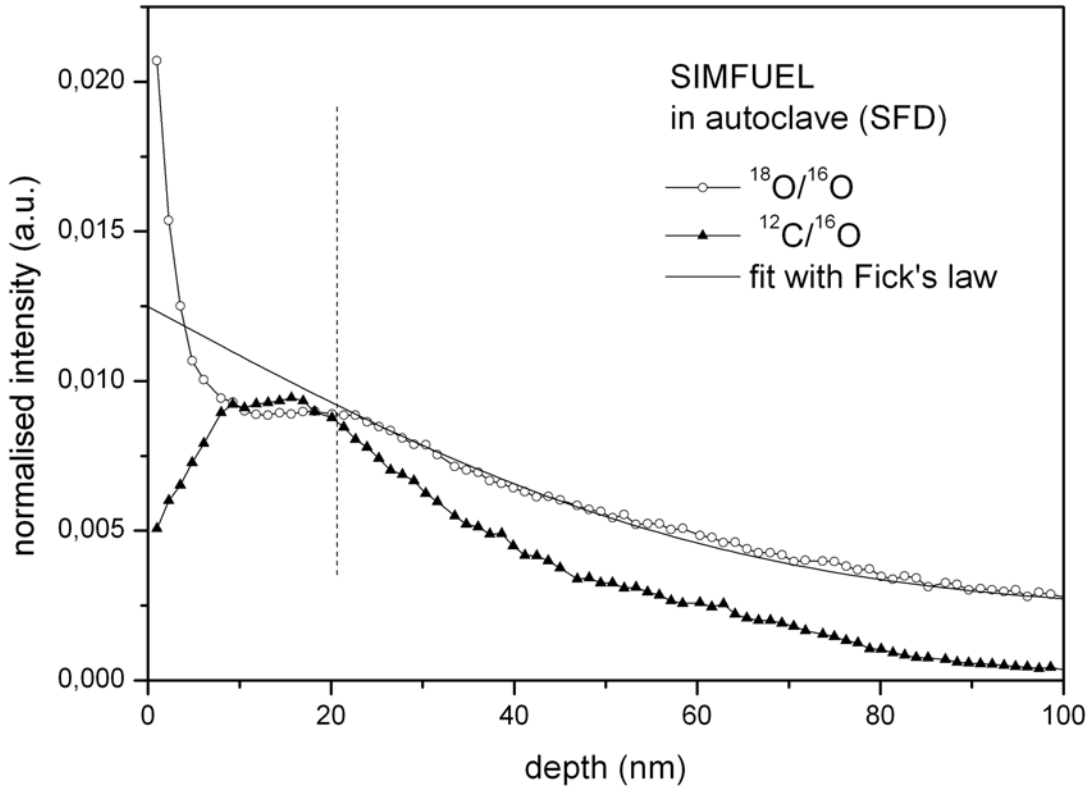

Figure 4.3-5: SIMFUEL sample leached in autoclave (SFD). Average SIMS profiles acquired for ^{18}O and ^{12}C (both intensities normalised vs. ^{16}O). The oxygen profile shows the "two-step" shape matching the presence of a carbonate phase on the surface (dashed line). From the fit of the second part of the profile, the diffusion coefficient $D_L = (5.42 \pm 0.03) \cdot 10^{-23}$ m^2/s is determined.

The long-range profile (Figure 4.3-6) is in general terms similar to the ones of the two polycrystalline UO_2 also corroded in autoclave (PCA and PCB). There is some indication of superficial grain boundary diffusion, within the depth of 0-300 nm, but the penetration depth is so small (0.3 µm) in comparison to the size of an UO_2 grain (9 µm) that the Levine-MacCallum's model cannot be reasonably applied.

However, it is interesting to compare the long-range profile obtained on SIMFUEL (SFD) with the one obtained for polycrystalline UO_2 (PCA), since both samples exhibit a similar final U concentration (Table 4.3-2). The diffusion tracer ^{18}O has penetrated deeper into the SFD, while the surface concentration of ^{18}O is ten times higher for the PCA. This supports the conclusion that the low final U concentration in the case of SFD might have been rather due to hindered oxidation/dissolution

behaviour of SIMFUEL (due to the presence of lanthanides [45]) than to reducing conditions like in the case of PCA.

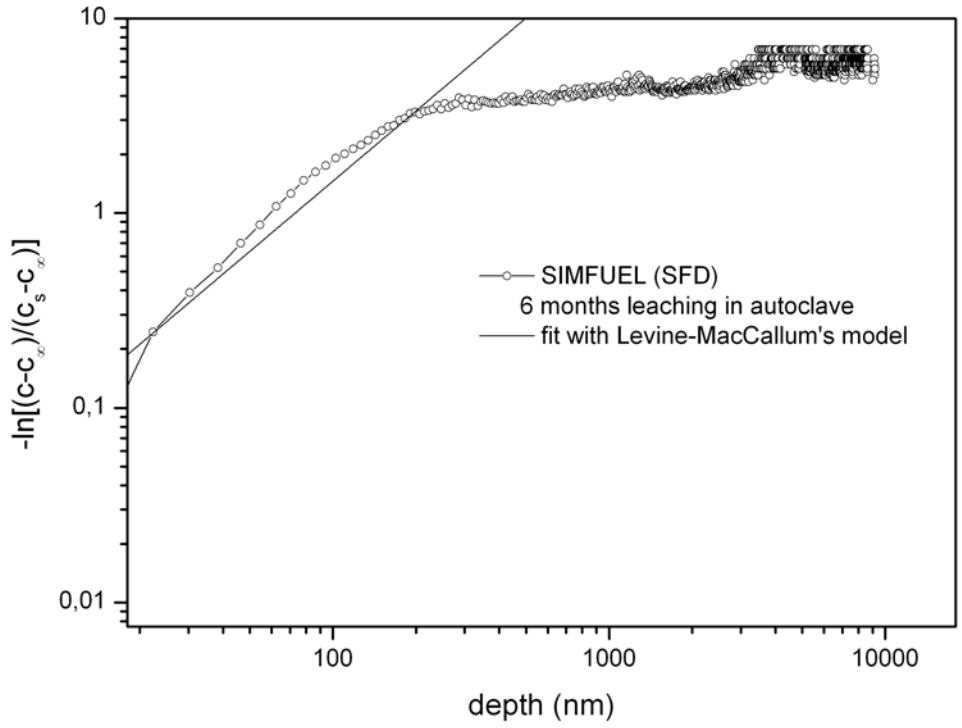

Figure 4.3-6: SIMFUEL in autoclave: profile on log-log scale. The fit with Levine-MacCallum's model is not considered for evaluation of grain boundary diffusion coefficient as only the first 300 nm of the profile seem to agree with the model.

5 Discussion

In this chapter, the experimental findings presented in the different sections of Chapter 4 are compared with each others and globally discussed according to different points of view like the matrix dissolution (sect. 5.1); the validity of the SIMS method for diffusion studies in the light of the possible surface artefacts (Sect. 5.2); the possibility to obtain a single value for D_L, chemical diffusion coefficient of oxygen in UO_2 lattice, from the complete set of experimental data (Sect. 5.3); the determination of grain boundary diffusion coefficients for oxygen in polycrystalline UO_2 (Sect. 5.4 and sub-sections).

5.1 Corrosion of UO_2 matrices

The analysis of the leachates produced by the corrosion experiments has been considered in this study mostly as complementary information to the characterisation of the diffusion profiles. Nevertheless, it was possible to draw some interesting remarks from these data.

Table 5.1-1: Summary of ICP-MS leachate analysis for all experiments carried out in this study.

Sample	*matrix*	*solution*	*Temp. (°C)*	*Time (months)*	*$[^{238}U]$ (M)*
PC1	Polycrystalline UO_2	Pure water	≈ 25	3	$(4.39 \pm 0.08)\cdot10^{-7}$
PC2				3	$(2.10 \pm 0.04)\cdot10^{-7}$
PC5				4	$(1.95 \pm 0.60)\cdot10^{-7}$
PCCO3		carbonate		4	$(1.17 \pm 0.30)\cdot10^{-5}$
PCA*				6	$(9.65 \pm 0.27)\cdot10^{-10}$
PCB*				6	$(1.63 \pm 0.03)\cdot10^{-6}$
SC1	Single crystal	Pure water (silicate)		4	$(1.60 \pm 0.05)\cdot10^{-8}$
SC60			60	4	$(3.98 \pm 0.11)\cdot10^{-8}$
SCCO3		carbonate	≈ 25	4	$(9.71 \pm 0.20)\cdot10^{-7}$
SCC*				6	$(2.72 \pm 0.08)\cdot10^{-7}$
SF1	SIMFUEL 8%	Pure water		6	$(6.02 \pm 0.25)\cdot10^{-7}$
SFCO3		carbonate		4	$(4.29 \pm 0.07)\cdot10^{-8}$
SFD*				6	$(4.42 \pm 0.06)\cdot10^{-10}$

*experiments carried out in autoclave, under 10 bar H_2.

In general terms, the leachate of the so-called single-crystal UO_2 showed a lower U concentration than the leachate of polycrystalline UO_2, considering similar conditions of temperature, contact-time and solution composition (for example the presence of carbonate). For SIMFUEL, in two cases (SFCO3 and SFD), the dissolution rate was considerably lower than for the other matrices (for example, PCCO3 and PCB); in one case (SF1) the dissolution behaviour was similar to polycrystalline UO_2 leached in similar conditions (PC1-2-5), albeit the contact time was longer..

The leachate originated from the experiment carried out at 60°C on a single-crystal sample has a total uranium concentration comparable (only slightly higher) to the similar experiment carried out at room temperature. The fact that some experiment were carried out in air (SC60, PC1) and not in a N_2-glovebox did not produce a substantial difference from the point of view of the dissolution.

The presence of a total carbonate concentration of $2 \cdot 10^{-3}$ M increases as expected the dissolution rate of UO_2. This is most visible comparing the two polycrystalline UO_2 sample leached under identical oxidising conditions with or without the addition of carbonated to the solution (denominated PC5 and PCCO3, respectively): the total uranium concentration in solution increases of two orders of magnitude.

The leachates originated from the autoclave experiment showed that the conditions were not actually the same for all four experiments. The four-order magnitude difference between the two identical experiments on polycrystalline UO_2 in the autoclave (PCA and PCB) can only be explained by the fact that only one of the two vessels had been bubbled by $H_{2(g)}$. The U concentration of the final solution for PCA is comparable to the concentration reported by Carbol *et al.* for similar experiments under reducing conditions [88] but still higher. It must be underlined, however, that the initial uranium concentration of the "blank" solution, the ^{18}O-labelled water added with $2 \cdot 10^{-3}$ M total carbonate, had a U concentration of $(2.49 \pm 0.7) \cdot 10^{-10}$ M. This represent a limitation to the quantification of the U concentration under reducing conditions and especially to the comparison with experiments carried out with different solutions. While the other polycrystalline UO_2 (PCB) and the single-crystal (SCC) both display similar concentration to the other experiments carried out in oxidising conditions (10^{-6} 10^{-7} M), the SIMFUEL sample (SFD), shows U concentration in the order of 10^{-10} M, in spite of the fact that the SIMFUEL solution had not been purged by H_2. In this case, rather than reducing conditions like in the case of PCA, the presence of ε-particles and lanthanides can be the reason for a larger resistance to oxidation/dissolution [45, 79]. This is confirmed by the analysis of SIMS profiles that shows a larger penetration of ^{18}O for SIMFUEL than for all other polycrystalline samples leached in autoclave (see Paragraph 4.3.4)

5.2 SIMS depth profiles: the problem of surface artefacts

Surface roughness is a major issue in SIMS depth profiling, as it contributes to the depth resolution of the measurement and in this way it affects the capability of this analytical tool to provide reliable information about the composition of thin layers of material. According to Barber *et al.* [112], if the surface roughness is comparable to or higher than the characteristic thickness of the near-surface region, a sputtered depth can be defined perpendicular to the normal of a surface element. Thanks to the low values of rugosity and roughness profile average slope of the sample surface, the effect of the variation of the local angle of incidence of the ion beam can be neglected in our case. The local sputtered depth can then be considered homogeneous and topographically congruent all over the field of analysis of the ion beam.

The zero-time profile can provide an indication on the actual depth resolution. The evaluation of the actual depth resolution for SIMS shallow depth profiling is a complex matter, as this quantity is affected by a number of factors (e.g., roughness and other surface effects), and depending on the depth itself. Roughly speaking, for our purposes the nominal depth resolution can be considered as the lower limit of the actual resolution, while the width of the zero-time profile (measured, for example, at 10% of its initial value) can be regarded as the upper limit. We can definitely state, therefore, that our actual depth resolution for the short-range profiles is in the order of 2-3 nm.

AFM analysis showed that during the sputtering of a single-crystal UO_2 surface roughness is not increased by the effect of the ion beam. This is not the case for polycrystalline UO_2, where the different grains have different sputtering yield and therefore result in being eroded with different rate, contributing to an increase of the roughness and a loss of depth resolution. The roughening effect increases with increasing crater depth, meaning that the depth resolution of the measurement is worse for long-range than for short range profiles. It is not straightforward to quantify the contribution of the roughening effect to the total uncertainty on the determination of the diffusion coefficient obtained from the fit of the profiles. In the case of the short-range profiles, the results obtained from polycrystalline and single-crystal samples (where this progressive increase of roughness is less significant) are in good agreement. This indicates that, although the contribution of the roughening effect is important, it becomes negligible compared to the unavoidable scatter of experimental results acquired on different samples, where many other differences stemming from reproducibility of surface preparation can have produced an even larger effect of surface reactivity. For long-range profiles the contribution of the roughening effect to the uncertainty of the determination of diffusion coefficients might be larger. However, the most significant variation in concentration occurs in the near-surface area while at large depths the profiles are constituted by consecutive points displaying minimum variation in intensity: a worse depth resolution in this part of the profile has a smaller repercussion on the determination of the diffusion coefficient obtained from the fit, than it would have had for the superficial part.

5.3 Lattice diffusion

Under oxidizing conditions, the surface of the UO_2 samples necessarily undergoes oxidation before and during water-contact. Therefore, the oxygen diffusion coefficients obtained from SIMS profiles acquired on the near-surface area are *chemical* diffusion coefficients (as an oxygen concentration gradient is present) and should be referred not to stoichiometric UO_2 but to oxidised UO_{2+x}. In the present study, different oxygen diffusion coefficients were obtained from several different UO_2 matrices corroded under different conditions. The experimental values are summarized in Table 5.3-1 and Table 5.3-2.

Table 5.3-1: Oxygen diffusion coefficients obtained in different UO_2 matrices leached under oxidising conditions

Sample	*UO_2 matrix*	*Temp. (°C)*	*Leachant*	*D_L (m^2/s)*	
PC1	Polycrystalline	≈ 25	pure water	$(1.4 \pm 0.3)\cdot10^{-24}$	
PC2				$(2.5 \pm 0.1)\cdot10^{-24}$	
PC3				$(3.0 \pm 0.2)\cdot10^{-24}$	
PC5				$(2.9 \pm 0.1)\cdot10^{-24}$	
PCCO3			carbonate	$(1.9 \pm 0.2)\cdot10^{-23}$	
SC1	Single crystal		(silicate)	$(5.4 \pm 0.3)\cdot10^{-23}$	
SC60		60		$(6.9 \pm 0.7)\cdot10^{-24}$	$(1.7 \pm 0.2)\cdot10^{-22}$
SCCO3		≈ 25	carbonate	$(1.1 \pm 0.1)\cdot10^{-24}$	$(1.16 \pm 0.02)\cdot10^{-23}$
SF1	SIMFUEL 8%		pure water	$(6.8 \pm 0.1)\cdot10^{-24}$	
SFCO3			carbonate	$(6.7 \pm 0.3)\cdot10^{-24}$	

In principle, for an evaluation of lattice diffusion only experiments carried out on single-crystal UO_2 samples should be considered, thus eliminating the potential contribution of grain boundary diffusion. In particular, the profiles acquired at 60°C should be considered more reliable, as the diffusion length is larger. It is possible to notice that the value obtained on single-crystal at 60°C, $D_L = (6.9 \pm 0.7)\cdot10^{-24}$ m^2/s, agrees much better with Lay's extrapolation [60] than the value measured at room temperature (≈ 25°C). Lay's series of experiments were carried out at high temperature (>600°C) and considering the uncertainty on such extrapolation, at 25°C the D_L value spans between $3.3\cdot10^{-29}$ and $1.1\cdot10^{-22}$ m^2/s. As Grambow [32] observed, this extrapolation would rather provide the upper limit of the range in which the chemical diffusion coefficient of oxygen in UO_2 can be expected to be at 25°C: 10^{-23} - 10^{-25} m^2/s. The D_L determined at room temperature on single-crystal UO_2 is certainly compatible with this span.

Table 5.3-2: Oxygen diffusion coefficients obtained in different UO_2 matrices leached in autoclave at a pressure of 10 bar H_2 and a temperature of 25ºC.

Sample	*UO_2 matrix*	*Exp. Conditions in autoclave*	*Leachant*	*D_L (m^2/s)*	
PCA	Polycrystalline	H_2 purging (reducing)		$(6.4 \pm 0.1)\cdot10^{-24}$	
PCB			H_2 ^{18}o (98%)	$(2.21 \pm 0.02)\cdot10^{-23}$	
SCC	Single-crystal	No purging (oxidising)	2mM $NaHCO_3$ + 10mM NaCl	$(1.1 \pm 0.1)\cdot10^{-24}$	$(1.8 \pm 0.2)\cdot10^{-23}$
SFD	SIMFUEL 8%			$(5.42 \pm 0.03)\cdot10^{-24}$	

Furthermore, also the data obtained from the analysis of several polycrystalline samples are in good agreement with this prediction. Also diffusion profiles resulting from different contact times were acquired, confirming the same value of D_L and showing clearly the expected dependence of the diffusion length with the contact-time. All this confirms the reliability of SIMS diffusion profiles even at room temperature with limited contact-time (from 3 to 9 months) and even in a near-surface area no more than a few nm thick, despite the unavoidable problems of surface roughness, porosity and other imperfections (as the so-called single-crystal samples were in fact not grown in controlled conditions).

All experimental D_L determined in the present study are comprised in the span indicated by Grambow's prediction. However, the uncertainty attributed to each D_L values only on the basis of the precision of each experimental point in the averaged profile is much inferior to the difference between coefficients obtained from different samples. This is not surprising, considering that important parameters like temperature and oxygen partial pressure were subject to fluctuations and that even small difference of roughness and porosity between samples might result in large difference of surface reactivity on the scale probed by SIMS analysis.

In this sense, the diffusion coefficients determined in the different experiments, might actually refer to slightly differently oxidised UO_{2+x} surfaces (due to the dependence of the oxygen diffusion coefficient in UO_2 on the stoichiometry, as discussed in Paragraph 2.2.5). This is all the more evident as in the case of single-crystal UO_2 the two different diffusion coefficients are obtained from different areas of the same surface. The fact that polycrystalline UO_2 had a more homogeneous behaviour than single-crystal UO_2 surfaces can be tentatively explained with the different average grain size and, thus, by the different distribution of reactive surface sites such as grain boundaries. Polycrystalline UO_2 has uniform grain dimension (10 µm diameter) while the single-crystal slices are constituted by macro-crystals with varying dimensions of several mm.

In fact, observing all the values of D_L experimentally obtained in this study, it is actually possible to recognize two main ranges of values at ≈ 25°C for UO_2 (both single-crystal and polycrystalline samples) in oxidising conditions. The higher values of D_L are found in areas or samples characterised by the presence of complexants of U(VI), such as carbonate or silicate. The values of D_L are instead determined on

surfaces showing no or negligible presence of carbonate and silicate phases. In order to simplify the comparison, the two ranges can be expressed by the average values: $D_L = (2.1 \pm 0.8)\cdot 10^{-24}$ m^2/s for the lower range and $D_L = (2.8 \pm 1.6)\cdot 10^{-23}$ m^2/s. The difference between the two ranges is roughly one order of magnitude while each D_L range has a span of half an order of magnitude.

These two averaged values offer a possibility for further observation, on the basis of the comparison with literature findings. In Figure 5.3-1 the two ranges, as well as the two single points obtained at 60°C, are plotted along the two Arrhenius-type expression of the diffusion coefficients for U_4O_9 and U_3O_7 indicated by Poulesquen *et al.* [30] :

$$\tilde{D}_L[U_4O_9] = 1.36\cdot 10^{-5}\exp\left(\frac{-57000}{RT}\right)$$

$$\tilde{D}_L[U_3O_7] = 1.16\cdot 10^{-3}\exp\left(\frac{-123000}{RT}\right)$$

As visible in Figure 5.2.1, even when taking into consideration the error in the experimental D_L values determined in this work, all values can be considered compatible with U_3O_7 and the presence of U_4O_9 can be excluded.

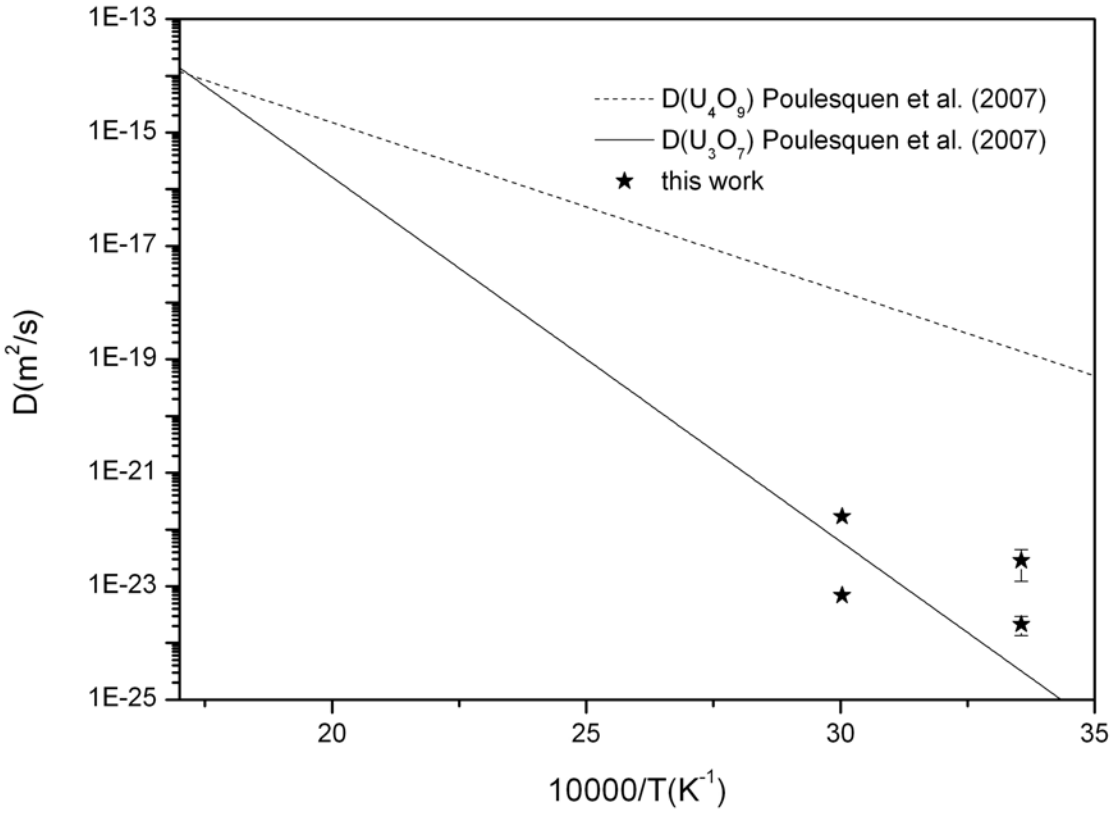

Figure 5.3-1: Comparison of experimental data here obtained with extrapolation given by Poulesquen *et al*. [30]

Comparing our results with those of Fayek and Kyser [58], it is possible to note that the higher diffusion coefficient span well agrees with the extrapolation of the diffusion coefficient associated to the so-called UO_3 phase, as defined by the authors. As for the term uraninite, the stoichiometry of the sample used for the study is not clear but is given by the authors to be comprised in the interval $UO_{2.25}$-$UO_{2.67}$. In fact, the extrapolation of the data given for uraninite by Fayek and Kyser [58] and of those given by Poulesquen *et al.* [30] for U_3O_7 are in good agreement.

$$D^*_L[uraninite] = 1.95 \cdot 10^{-10} \exp\left(\frac{-62000}{RT}\right)$$

$$D^*_L[UO_3] = 1.3 \cdot 10^{-15} \exp\left(\frac{-21197}{RT}\right)$$

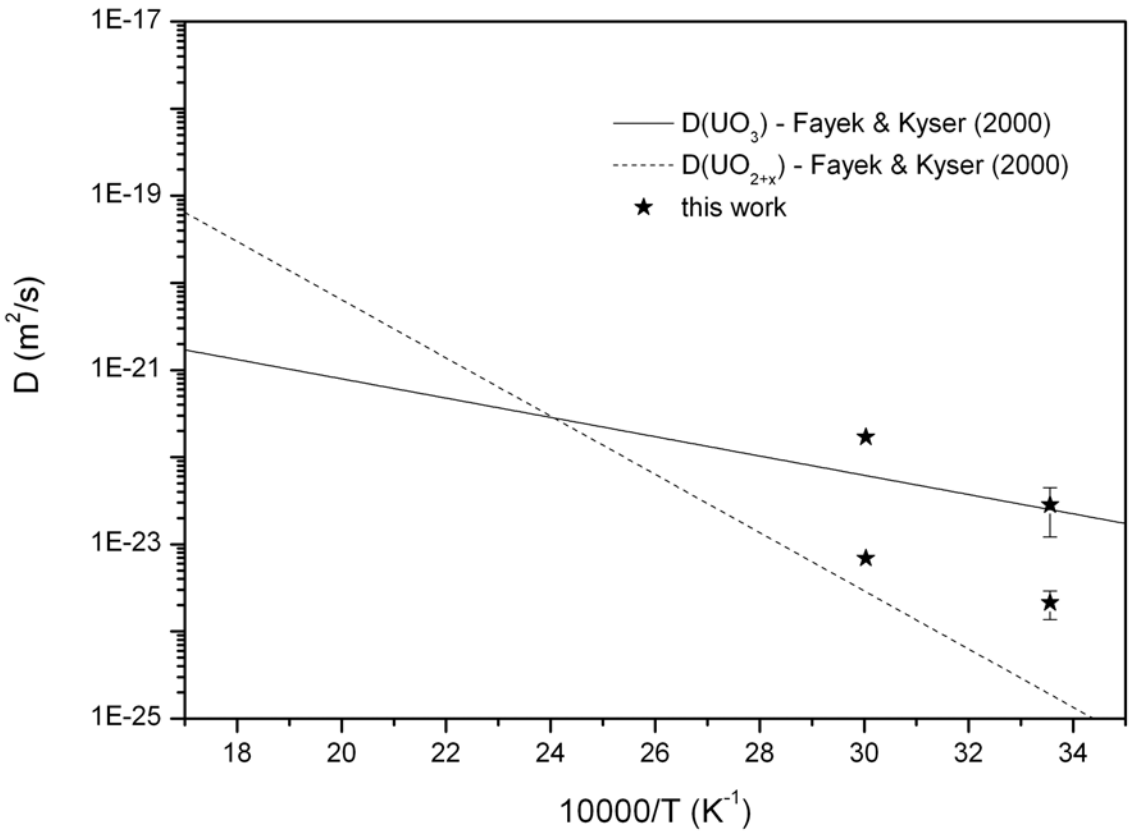

Figure 5.3-2: Comparison of experimental data here obtained with extrapolation given by Fayek & Kyser [57]

The comparison with the extrapolated data of both Poulesquen *et al.* [30] and Fayek & Kyser [58] gives indication that the lower range of D_L values ($D_L = (2.1 \pm 0.8) \cdot 10^{-24}$ m^2/s), determined on surfaces free from carbonate or silicate deposition, might actually describe oxygen diffusion in U_3O_7 ($x \approx 0.33$). The higher range of D_L values might instead indicate the presence of a U(VI)-phase, similar to the so-called UO_3 phase considered by Fayek and Kyser [58]

Finally, a third group of values is recognizable among the experimental results, that can be indicated with the average value $D_L = (6.6 \pm 0.2) \cdot 10^{-24}$ m^2/s, an intermediate range between the two intervals recognized for all other samples. Included in this range are the oxygen diffusion coefficients determined from experiments on SIMFUEL and the diffusion coefficient determined on polycrystalline UO_2 leached under reducing conditions (PCA).

Considering the chemical and physical heterogeneity of the SIMFUEL it is difficult to interpret the results of the different experiments. However, for those samples exhibiting a "two-step" profile (SFD), which matches the presence of a carbonate phase covering the surface, the value $D_L = 5.4 \cdot 10^{-23}$ m^2/s is found, in agreement with the other results for carbonate or silicate deposited samples. In the other cases, as for samples SF1 and SFCO3 where a "one-step" curve was obtained, the value determined was found consistently close to the "intermediate" value determined in reducing conditions.

This is a hint of the fact that the oxidised phase produced on the surface during water contact could be the same for SIMFUEL samples and polycrystalline UO_2 leached under reducing conditions (PCA), more specifically U_4O_9. In fact, oxidation of SIMFUEL is known to be hindered by the presence of lanthanides and, similarly to what observed for spent fuel, SIMFUEL is expected to retain U_4O_9 geometry even for larger O/U than 2.25 thanks to the presence of fission products [45]. Even if it is highly speculative, the SIMFUEL results could be the evidence of the presence of U_4O_9 phase under conditions that in other experiments had lead to the presence of U_3O_7 instead, thus with a smaller diffusion coefficient (as indicated by Poulesquen *et al.* [30], U_4O_9 is characterised by a higher diffusion coefficient than U_3O_7). As far as PCA is concerned, instead, the presence of U_4O_9 might be due to the reducing conditions of the experiment, which hinders oxidation to higher stoichiometries.

Nevertheless, the diffusion coefficients given for U_4O_9 by Poulesquen *et al.* [30] are almost four orders of magnitude higher than the highest experimental value obtained in this study, and on this basis alone the presence of U_4O_9 in the samples investigated in this study should be excluded. However, the presence of U_4O_9 phase has been questioned and discussed over the years and so far the actual stoichiometry of the phase facing the solution has actually not been determined, especially at room temperature.

Matzke [113] indicated the presence of a thin layer between the UO_2 bulk and the growing surface layer of U_3O_7 that could be interpreted as a U_4O_9 phase. The thickness of this intermediate layer was estimated to be 5 nm at ≈ 200°C and therefore it is probable that at room temperature it would be even thinner. The interface between these layers would then be difficult to recognize in the SIMS depth-profiling. In fact, the ion beam might sputter different layers simultaneously, providing only an average (or mixed) information.

For the same reason, the small tracer concentration gradient at the interface between the oxidised matrix and the pristine stoichiometric UO_2 bulk would be difficult to distinguish from the fluctuation of the signal due to lower statistics. This interface, if

visible, would also represent the interface between the part of the sample in which diffusion happens under the driving force of a chemical gradient, and the bulk where only self-diffusion takes place. At room temperature, with relatively short lasting experiments, these different layers become comprehensively more difficult to distinguish.

It is very likely, then, that all the depth profiles acquired in this study involved more than one UO_{2+x} phase, and that the resulting values of diffusion coefficient estimated would then slightly vary from sample to sample and from area to area according to which superficial phase is predominant. The lower range of values plotted in the figure would then characterise the samples in which U_3O_7 was the predominant phase while the intermediate range might be the result of a more significant presence of U_4O_9 phase.

5.4 Grain-boundary diffusion

In this study, evidence of grain boundary diffusion has been found for some of the polycrystalline UO_2 samples in contact with water in oxidising conditions, confirming what has been indicated by other works, reporting dissolution and oxidation behaviour of UO_2 and spent fuel [32]. Nevertheless, the same behaviour was not encountered in all the experiments carried out in the present study. SIMS studies carried out by other authors have also come to diverging conclusions in this regard. In the next paragraphs an attempt will be made to interpret the different oxygen grain boundary diffusion studies in UO_2, from a theoretical as well as experimental point of view.

5.4.1 Physical validity of the applied model

We verified *a posteriori* that the assumptions made when applying the high-diffusivity-paths model are fulfilled, and the values found for the diffusion coefficients are realistic. The applicability of the model essentially depends on the particular kinetic regime of grain boundary diffusion. The solution of the Levine-MacCallum's model used to fit the long-range profiles in this study is valid for polycrystals in the so-called type-B kinetics regime, which, according to Harrison's conditions [63], is defined by the relation:

$$\delta < \sqrt{D_L t} << d \qquad \textbf{5.4.1-1}$$

where d is the mean linear dimension of the grains and δ is the grain boundary width. In our case, as mentioned above, it was found $d \approx 9$ μm and it could be assumed $\delta \approx 1$ nm. Thereby the condition in equation 5.4.1-1 is evidently verified. Secondly, the 6/5-solution of Levine-MacCallum's model is derived under the condition:

$$0.5 < \eta\, \tau^{-1/4} < 8 \qquad \textbf{5.4.1-2}$$

where $\eta \equiv (x/\delta)(6\, D_L / D_B)^{1/2}$, $\tau \equiv 4\, D_L\, t / \delta^2$, and the quantity $\eta\, \tau^{-1/4}$ is referred to as an "effective" penetration depth [67]. For the polycrystalline samples for which the Levine-MacCallum's model was found to fit the long-range profiles, for example, with the values of $D_L = 2 \cdot 10^{-24}$ m^2/s and $D_B = 7.5 \cdot 10^{-15}$ m^2/s we obtained, this conditions is fulfilled for $6.5 < x < 110$ μm. This means that the penetration depth should be roughly equal to, or larger than, the mean diameter of the grains, as physically sound.

5.4.2 Comparison of results with literature data

Previous studies involving SIMS depth profiling had been carried out, at high temperature and under reducing conditions, and had come to the conclusion that

grain boundaries do not behave as high diffusivity paths [54, 74]. The present study has instead showed that, at least in oxidising conditions, oxygen/water diffusion along grain boundaries can be recognized and quantified by means of SIMS depth profiling. Nevertheless, this study has also shown that this behaviour is not always detectable.

Marin and Contamin [114] in their pioneer SIMS study in 1969 concluded that grain boundaries did not appear to play any important role on the basis of two main observations: the fact that SIMS ion maps of ^{18}O did not show any enrichment along grain boundaries and the fact that sintered samples and single crystals yielded the same diffusion coefficient. As for the first point, our study also proves that the fact that the SIMS ion maps show no particular ^{18}O enrichment at the grain boundaries is not necessarily significant. In fact, the lateral resolution of SIMS is at best in the order of 0.5 μm but in most cases, as in this study the diameter of the primary ion beam is in the range of ≈ 1-10 μm. Grain boundaries in polycrystalline UO_2 have an average width expected in the order of 1-2 nm [70]. It is then clear how ion imaging of the sample surface cannot be considered the suitable technique to show evidence of grain-boundary diffusion. As for the second point, the identity of profiles obtained on polycrystalline and single-crystal samples has been also reported by more recent SIMS study, such as the analysis made by Sabioni *et al*. [74] in 2000. Also in this case, the diffusion profiles obtained for single-crystal and polycrystalline UO_2 are found to be very similar, leading to the conclusion that grain boundaries are not preferential paths for oxygen diffusion in UO_2. Nevertheless, some questions arise from the analysis of the data of Sabioni *et al*. [74]. The value of $D_L = 3.61 \cdot 10^{-16}$ m^2/s there reported (for an exposure time of 1860 s at 1000 K) corresponds to a diffusion length of about 1.6 μm, while the study only shows diffusion profiles up to 4 μm. Thus, it is not surprising that the profiles for single-crystal and polycrystalline UO_2 shown in their article do not appreciably diverge. In fact, the depth of 4 μm probed is of the same order as the diffusion length of oxygen in the lattice and smaller than the grain size, 12 μm. The typical tail of grain boundary diffusion – for which moreover we measured an ^{18}O isotopic abundance two order of magnitude smaller than the one on the surface – would have been visible only if greater depths had been investigated and an isotopic sensitivity of the same order of magnitude of the ^{18}O natural abundance had been adopted. Similar doubts about the actual grounds of such conclusions have been also raised by Fayek *et al.* [57] who indeed confirmed the existence of two diffusive processes, one very fast and related to the presence of boundaries.

The value of D_B that was measured in the present study, in the first two corrosion experiments carried out in oxidising conditions on polycrystalline UO_2, was found to be several orders of magnitude larger than the prediction made for spent fuel by Grambow [32] on the basis of the data of Einziger and Woodley [71, 72]. This difference can be attributed to the fact that the evaluation of the activation energy for spent fuel at room temperature was affected by large uncertainty and therefore Grambow's evaluation in itself was highly speculative.

5.4.3 Reproducibility of experiments

Beside the divergence from the conclusions presented by other authors discussed in the previous paragraph, a more significant source of doubts is represented by the reproducibility of the experimental findings. Not all polycrystalline UO_2 samples showed evidence of grain boundary diffusivity, even when leached in the same conditions. While it could be anticipated that grain boundary diffusivity would be hindered in reducing conditions (as it was in the case of the experiments of Contamin *et al*. [61] and Sabioni *et al*. [74]), it is not obvious the reason why polycrystalline UO_2 samples leached in oxidising conditions would show very different behaviour in terms of grain boundary diffusion.

It is unlikely that the agreement with the Levine-MacCallum's model could simply stem from a measurement artefact since the analytical procedure was identical in all cases. There is a chance though that not all the experimental conditions were under control, especially in terms of state of the surface, on a μm-nm scale. In fact, the preparation of the sample surface is not perfectly reproducible: even though porosity was always in the same range, there were differences in surface roughness due to the polishing procedure and possible obstruction of the opening of grain boundaries can have been caused in some samples more than in others by the material removed during the polishing.

Moreover, it was not possible to monitor and control the oxygen partial pressure, even though it is supposed not to have an impact on the oxidation kinetics [45].

Finally, even if all samples were annealed to stoichiometry according to the same procedure, the sample surface might have been quickly oxidised during the time elapsing between the end of the annealing treatment and the beginning of the corrosion experiment, when the sample was transferred into the solution. In the case of the last polycrystalline sample leached in pure water (PC5) and all the following experiments this time was reduced to a few seconds, while in the previous experiments (PC1-3) it had been between one and two days.

A better characterisation of the surface oxidation kinetics in the laboratory atmospheric conditions would be needed but indicatively a more oxidised surface would be subjected to a larger probability of oxygen uptake from the water and to a faster diffusion of oxygen than a stoichiometric surface.

This explanation is supported by the fact that samples transferred into water after a shorter delay showed a much reduced tracer uptake. As grain boundaries are known to oxidise more easily than the surface, it is likely that in a sample presenting higher surface stoichiometry also the grain boundaries would present an increased affinity for ^{18}O-tracer, and consequently a faster transport along them.

It is possible then that grain boundary diffusion takes place without being visible: the concentration span in which the diffusion profile take place becomes so much smaller than the difference in concentration between points at depth larger than a ≈ 100 nm is no longer detectable. A schematic representation of the possible mechanism is proposed in Figure 5.4-1.

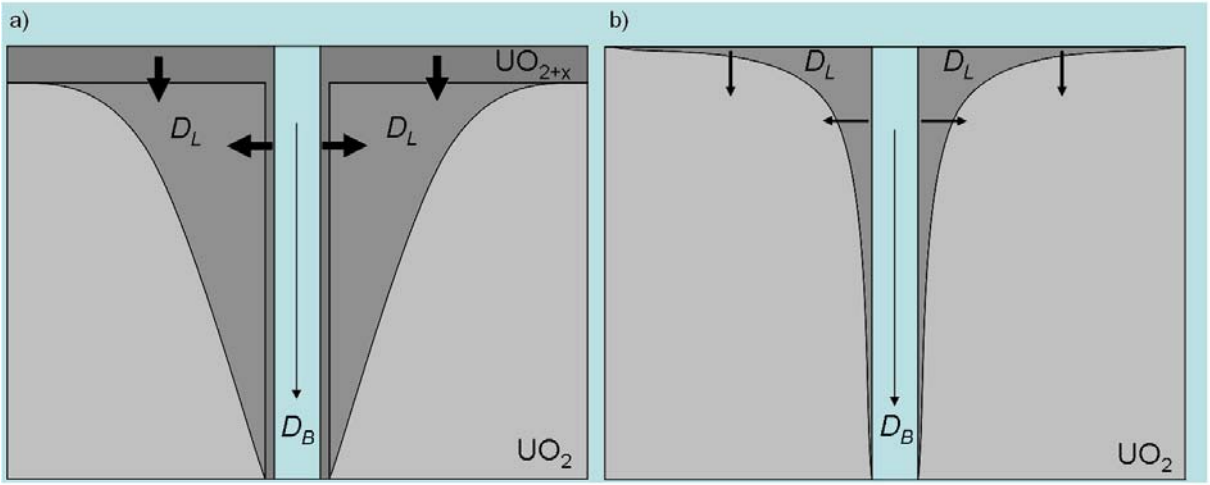

Figure 5.4-1: Effect of pre-oxidised layer on grain boundary diffusion. a) A pre-oxidised UO_{2+x} phase, characterised by a higher diffusion coefficient determines a larger uptake of ^{18}O also along the grain boundary; b) when sample surface is perfectly stoichiometric, the oxygen diffusion coefficient in the lattice is lower and determines a smaller contribution of the tracer also along the boundary.

This observation agrees with the indication given by Grambow [74]: grain boundary diffusion at room temperature was predicted to be so slow that no experiment was considered able to measure it. At the same time, experiments at larger temperature would not show it either, as the bulk diffusion would be fast enough to mask it: this interpretation explains the experimental finding of Sabioni *et al.*[74] and Contamin *et al.* [61] and agrees with the mechanism proposed by Fayek *et al*. [57].

5.4.4 Oxygen or water diffusion

Even if our work did show experimental evidence for grain boundary diffusion in UO_2, little can be said about the chemical form with which our tracer ^{18}O diffuses along them. Nagy *et al*. [103], analysing grain boundary diffusion of oxygen in a feldspar exposed to ^{18}O-labelled water, assigned the diffusion coefficient they measured to oxygen, but underlined how oxygen could actually be transported as OH^-, H_2O or more complex hydrogen-oxygen species. Also in water diffusion studies relying on techniques different from SIMS the concept of "water species" is often chosen [115] to indicate generally water molecules and hydroxyl ions and the diffusion coefficients measured are attributed to invariably one or the other species.

Mechanisms for water diffusion involving dissociation of the water molecules accompanied by interstitial diffusion of the oxygen ion through the crystal conduction plane (0.8 nm) are reported for alumina [116], while diffusion of water in glass has been studied as a reaction-diffusion process with formation of SiOH upon wet oxidation while fast moving molecular water has a concentration too low to be detected [115].

High mass resolution depth profiling of a polycrystalline UO_2 that had been leached in ^{18}O-water showed that ^{18}OH coming from the leaching solution is chemically present

in the matrix up to a depth of 2 μm. This value might indicate the depth of the etched (opened) grain boundary where water has had access, as well as of the presence of a hydroxyl-water compound of the kind of shoepite: $(UO_2)_xO(OH)_y{\bullet}n(H_2O)$. This observation hints at the possibility of a composite mechanism in which both the atmospheric (≈ 99.98% ^{16}O) O_2 dissolved in the leaching solution and the ^{18}O-water are playing a role, with the initial oxidation of UO_2 to UO_{2+x} (U_4O_9 - U_3O_7) followed by interaction with water.

Interaction between water and oxidised UO_{2+x} surfaces has been shown to be assisted by the migration of oxygen vacancy towards the surface as a consequence of migration of oxygen interstitial clusters towards the bulk [42, 117]. Dissociation of water molecules and incorporation of oxygen into the matrix follows [118]. Ideally, the same process would happen along the oxidised boundary and the presence of ^{18}O at large depths would then be the result of the penetration of water even though evidence of water molecules might not be found.

5.4.5 Long-term prediction

With an estimated grain boundary diffusion coefficient $D_L \approx 10^{-20}$ m^2/s, according to Grambow's calculations [32], oxygen would take 800 years to penetrate in the fuel for a distance equal to the grain diameter (25 μm in the case under analysis) and therefore grain boundaries oxidation should be an extremely slow process at room temperature and almost impossible to be observed.

Our measurement of $D_B \approx 10^{-15}$ m^2/s is several orders of magnitude higher, in the cases in which it was possible to quantify it. Using the Levine-MacCallum's model, such a value of D_B can be considered to obtain an estimation of the long-term consequences for the assessment of a geological disposal of spent fuel.

In the graph of Figure 5.4-2, the quantity $\frac{c(x)-c_\infty}{c_s-c_\infty} = \exp\left(-\alpha(t)(R-x)^{6/5}\right)$, where $\alpha(t) = \left[\frac{\delta D_B}{1.946}\left(\frac{D_L}{t}\right)^{1/2}\right]^{-3/5}$, is plotted for different values of time t and considering the radius of a typical fuel pellet R = 4 mm.

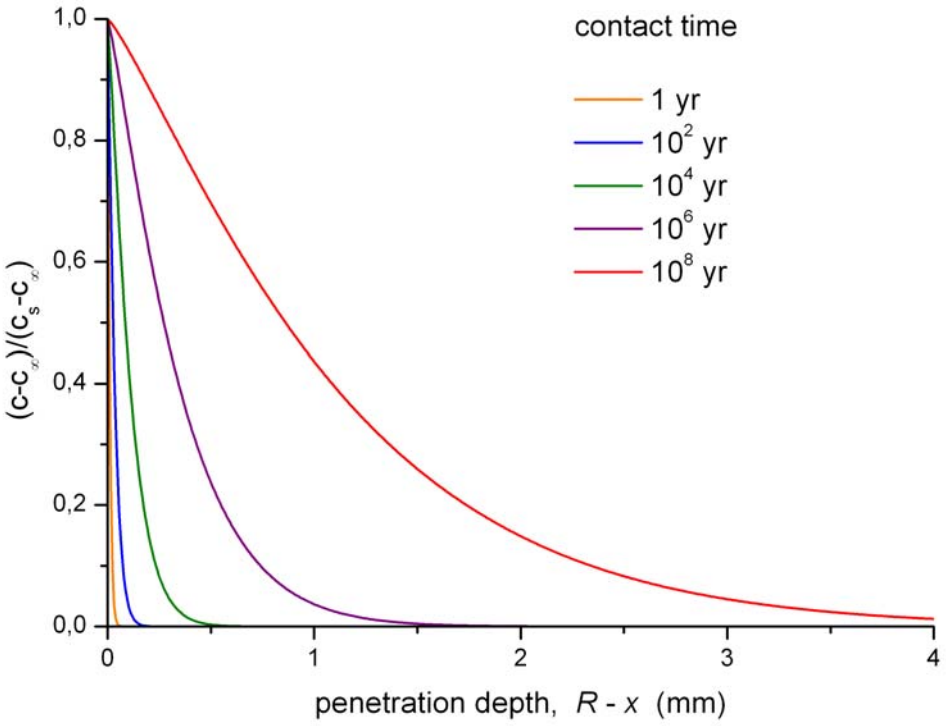

Figure 5.4-2: Estimated evolution of water penetration in time. If no other effects are considered, with the grain boundary diffusion coefficient measured in this study and a typical dimension of the fuel pellet radius (R = 4 mm) water would reach the centre in no less than one hundred million years.

It is possible to see that water/oxygen penetration would ideally reach the centre of a typical fuel pellet in no less than 10^8 years. This is an extreme simplification, as these data can only refer to oxidising conditions such as should not be pertinent to the case of most suggested sites for geological disposal. Furthermore, by oxidation of the fuel matrix, the mechanical stability of the fuel would be affected, with the detachment of oxidised grains, even on a shorter time scale.

6 Conclusions and future work

This study has succeeded to provide for the first time the measurement of oxygen diffusion coefficients in UO_2 matrices at temperature as low as 25°C. In fact, this study has confirmed the reliability of SIMS depth profiling for diffusion studies even at room temperature and with limited time scales (from 3 to 9 months), thus probing a near-surface area no more than a few nanometre deep. Despite the potential source of uncertainties represented by the unavoidable problems of surface roughness, porosity and other imperfections, the experimental results have shown good reproducibility in different UO_2 matrices.

In particular, the experimental values obtained for the chemical diffusion coefficient of oxygen in the lattice at 25°C are in the range 10^{-23}-10^{-24} m^2/s, which improves the predicted data obtained from the extrapolation of high temperature diffusion experiments. This study has also shown that the determination of the diffusion coefficients can provide additional information about the different phases formed by the wet or dry oxidation of UO_2. In fact, even small differences in the oxygen diffusion coefficient resulting from the presence of different UO_{2+x} stoichiometries, have been distinguished and determined via SIMS depth profiling.

The experimental data reported here indicate that the diffusion coefficient of U_3O_7 is in the range $D_L = (2.1\pm0.8)\cdot10^{-24}$ m^2/s while in a more oxidised phase, ideally a U(VI) phase, the diffusion coefficient is found to be roughly one order of magnitude higher, $D_L = (2.8\pm1.6)\cdot10^{-23}$ m^2/s. Corrosion experiments in reducing conditions and on SIMFUEL in oxidising conditions provided an intermediate value of $D_L = (6.6 \pm 0.2)\cdot10^{-24}$ m^2/s, which could be explained by a predominating presence of U_4O_9 in the oxidised surface layer. In fact, in the case of SIMFUEL 8% this can be justified by the presence of lanthanides in the crystal lattice while the reducing conditions can be responsible for hindering surface oxidation of polycrystalline UO_2.

Furthermore, this study has presented, for the first time, evidence of oxygen grain boundary diffusion in polycrystalline UO_2. The widely-used Levine-MacCallum's model for diffusion in polycrystalline material was applied to fit the diffusion profiles and to determine the diffusion coefficient of oxygen or oxygen-bearing water species along the grain boundaries in UO_2. At 25°C, this coefficient was found in the range $D_B \approx 10^{-14}$-10^{-16} m^2/s, considering a grain boundary width of ≈ 1 nm, *i.e.* roughly ten orders of magnitude larger than the oxygen diffusion coefficient in the crystal lattice.

The calculation of the grain boundary diffusion coefficient depends actually on the oxygen diffusion coefficient in the lattice of the grains adjacent to the boundary, and this in turns depends on the stoichiometry, as mentioned above. In fact, this study has shown that grain boundary diffusion in UO_2 at 25°C is mainly observable in UO_2 matrices exposed to oxidising environment before and during water contact. A possible explanation, based on the presence of a pre-oxidised surface layer prior to the diffusion experiments, is suggested. In line with this observation, the possibility to detect grain-boundary diffusivity might be improved by longer water-contact, which can provide higher tracer concentration in the solid, or higher temperature (for

example in the range 50-90°C), which ensures an increase of the penetration depth, thus improving the reliability of the measurement.

This study has then highlighted that, in order to study oxygen grain boundary diffusion in UO_2, a model should take into account the role played by the evolution of surface oxidation. In this sense, the experimental evidence presented in this work, emphasising the difference in terms of diffusion coefficient of the different UO_{2+x} phases, becomes particularly important for the development of a suitable model. Further investigations of the surface evolution during water contact, for example with other techniques like Raman, XPS and grazing-angle XRD, can offer complimentary information to SIMS near-surface depth profiling, and provide the basis for a more complete diffusion model.

The possibility to determine oxygen diffusion coefficients at low temperature is of crucial importance for the characterisation of spent nuclear fuel, with respect to the safety assessment of final disposal. In fact, high-temperature corrosion/diffusion experiments on spent fuel would lead to irreversible changes of the matrix, through mobilisation of volatile elements (such as for example He, Kr, Xe, I and Cs) and compounds (CsI, RuO_4) localised in fuel grains or at inter-granular positions. However, the experiments on SIMFUEL have shown that the diffusion behaviour of a more complex matrix can be quite different and even more significant divergence can be expected when features such as variable grain-size and α-activity are added to the picture. Necessarily, only an investigation on irradiated nuclear fuel would possibly offer a realistic view of the phenomena. For this reason, and thanks to the results presented in this work, experiments are underway to determine the water/oxygen diffusion in spent nuclear fuel.

Bibliography

[1] "Nuclear Safety Review for the Year 2009", *International Atomic Energy Agency*, IAEA/NSR/2009 (2010).

[2] "Nuclear Technology Review 2010", *International Atomic Energy Agency*, IAEA/NTR/2010 (2010).

[3] "Community Policy and Research & Training Activities", *EURADWASTE 08*, 2008, Luxembourg, European Commission.

[4] J. Bruno and R.C. Ewing: "Spent Nuclear Fuel", *Elements*, 2 (2006) pp. 343-349.

[5] G.R. Choppin: "Actinide chemistry: from weapons to remediation to stewardship", *Radiochimica Acta*, 92 (2004) pp. 519-523.

[6] G.R. Choppin, J.-O. Liljenzin and J. Rydberg: "Radiochemistry and Nuclear Chemistry", 3rd ed., Butterworth-Heinemann Ltd., Woburn, MA, USA (2002).

[7] I.R. Birss: "Helium production in reactor materials: Review paper", *Journal of Nuclear Materials*, 34 (1970) pp. 241-259.

[8] Y.-H. Koo, B.-H. Lee, J.-S. Cheon and D.-S. Sohn: "Pore pressure and swelling in the rim region of LWR high burnup UO_2 fuel", *Journal of Nuclear Materials*, 295 (2001) pp. 213-220.

[9] H. Kleykamp: "The chemical state of the fission products in oxide fuels", *Journal of Nuclear Materials*, 131 (1985) pp. 221-246.

[10] H. Kleykamp: "The chemical state of fission products in oxide fuels at different stages of the nuclear fuel cycle", *Nuclear Technology*, 80 (1988) pp. 412-422.

[11] D.W. Shoesmith: "Used fuel and uranium dioxide dissolution studies - a review", *NWMO technical report*, NWMO TR-2007-03 (2007) pp. 1-69.

[12] J. Bruno, D. Bosbach, D. Kulik and A. Navrotsky: "Chemical Thermodynamics Chemical Thermodynamics of Solid Solutions of Interest in Radioactive Waste Management", Vol. 10, OECD Publishing, Paris, France (2007).

[13] L.H. Johnson and D.W. Shoesmith: "Spent Fuel", in "Radioactive waste forms for the future", W. Lutze and R.C. Ewing eds., North-Holland, Amsterdam, The Netherlands (1988)

[14] P. Carbol, D.H. Wegen, T. Wiss and P. Fors: "5.16 - Spent Fuel as Waste Material", in "Comprehensive Nuclear Materials (vol. 5)", R.J.M. Konings eds., Elsevier, Oxford (2012)

[15] D.B. Curtis and A.J. Gancarz: "Radiolysis in nature: evidence from the Oklo natural reactors", *Swedish Nuclear Fuel and Waste Management Co.*, SKB Technical Report TR-83-10 (1983).

[16] "Geological Disposal of Radioactive Waste: Technological Implications for Retrievability", *International Atomic Energy Agency*, IAEA Report NW-T-1.19 (2009).

[17] W.E. Falck and K.-F. Nilsson: "Geological Disposal of Radioactive Waste: Moving Towards Implementation", *European Commission*, EUR 23925 EN (2009).

[18] F. King: "Critical review of the literature on the corrosion of copper by water", *Swedish Nuclear Fuel and Waste Management Co.*, SKB Technical Report TR-10-69 (2010).

[19] G. Hultquist, P. Szakalos, M. Graham, A. Belonoshko and A. Rosengren: "Reply to Lars O. Werme et al.: “Comments on ‘Water Corrodes Copper’"", *Catalysis Letters*, 135 (2010) pp. 167-168.

[20] D.W. Shoesmith and S. Sunder: "The prediction of nuclear fuel (UO_2) dissolution rates under waste disposal conditions", *Journal of Nuclear Materials*, 190 (1992) pp. 20-35.

[21] R. Szwarc: "The defect contribution to the excess enthalpy of uranium dioxide-calculation of the frenkel energy", *Journal of Physics and Chemistry of Solids*, 30 (1969) pp. 705-711.

[22] E. Maugeri: "Helium Behaviour in UO_2 Under Conditions Relevant for Spent Fuel Storage", doctoral dissertation, University of Pavia, Pavia, Italy (2009).

[23] P.G. Shewmon: "Diffusion in Solids", 2nd ed., The Minerals Metals and Materials Society, Warrendale, USA (1989).

[24] C.A. Colmenares: "Oxidation mechanisms and catalytic properties of the actinides", *Progress in Solid State Chemistry*, 15 (1984) pp. 257-364.

[25] B.T.M. Willis: "Crystallographic studies of anion-excess uranium oxides", *Journal of the Chemical Society, Faraday Transactions 2: Molecular and Chemical Physics*, 83 (1987) pp. 1073-1081.

[26] H. Matzke: "Atomic mechanism of mass transport in ceramic nuclear fuel materials", *Journal of the Chemical Society, Faraday Transactions*, 86 (1990) pp. 1243-1256.

[27] C. Ferry, C. Poinssot, V. Broudic, C. Cappelaere, L. Desgranges *et al.*: "Referentiel scientifique sur l'evolution à long terme des combustibles uses", *Commissariat à l'Energie Atomique* CEA Technical Report DPC/SECR 04-032 B (2005).

[28] G. Rousseau, L. Desgranges, F. Charlot, N. Millot, J.C. Nièpce *et al.*: "A detailed study of UO_2 to U_3O_8 oxidation phases and the associated rate-limiting steps", *Journal of Nuclear Materials*, 355 (2006) pp. 10-20.

[29] S. Aronson, J.R.B. Roof and J. Belle: "Kinetic Study of the Oxidation of Uranium Dioxide", *The Journal of Chemical Physics*, 27 (1957) pp. 137-144.

[30] A. Poulesquen, L. Desgranges and C. Ferry: "An improved model to evaluate the oxidation kinetics of uranium dioxide during dry storage", *Journal of Nuclear Materials*, 362 (2007) pp. 402-410.

[31] P.A. Tempest, P.M. Tucker and J.W. Tyler: "Oxidation of UO_2 fuel pellets in air at 503 and 543 K studied using X-ray photoelectron spectroscopy and X-ray diffraction", *Journal of Nuclear Materials*, 151 (1988) pp. 269-274.

[32] B. Grambow: "Spent fuel dissolution and oxidation. An evaluation of literature data.", *Swedish Nuclear Fuel and Waste Management Co.*, SKB Technical Report TR-89-13 (1989).

[33] S. Aronson: "Oxidation and corrosion of uranium dioxide", in "Uranium Dioxide: Properties and Nuclear Applications", J. Belle eds., US Atomic Energy Commission, Washington, D.C., US (1961)

[34] J. Janeczek, R.C. Ewing and L.E. Thomas: "Oxidation of uraninite: does tetragonal U_3O_7 occur in nature?", *Journal of Nuclear Materials*, 207 (1993) pp. 177-191.

[35] R.J. Finch and R.C. Ewing: "The corrosion of uraninite under oxidizing conditions", *Journal of Nuclear Materials*, 190 (1992) pp. 133-156.

[36] I. Casas, E. Cera and J. Bruno: "Kinetic studies of natural uranium minerals for the long-term evolution of spent nuclear fuel under oxidizing conditions", *Materials Research Society Symposium Proceedings*, 294 (1992) pp. 521-525.
[37] S. Sunder, D.W. Shoesmith, M.G. Bailey, F.W. Stanchell and N.S. McIntyre: "Anodic oxidation of UO_2: Part I. Electrochemical and X-ray photoelectron spectroscopic studies in neutral solutions", *Journal of Electroanalytical Chemistry and Interfacial Electrochemistry*, 130 (1981) pp. 163-179.
[38] H. Matzke: "Analysis of the structure of layers on UO_2 leached in H_2O", *Journal of Nuclear Materials*, 238 (1996) pp. 58-63.
[39] M.E. Torrero, E. Baraj, J. de Pablo, J. Giménez and I. Casas: "Kinetics of corrosion and dissolution of uranium dioxide as a function of pH", *International Journal of Chemical Kinetics*, 29 (1997) pp. 261-267.
[40] F.N. Skomurski, J.W. Wang, R.C. Ewing and U. Becker: "Charge distribution and oxygen diffusion in hyperstoichiometric uranium dioxide UO_{2+x} ($x<0.25$)", *Journal of Nuclear Materials*, (2012 (in press)) pp.
[41] F. Gupta, A. Pasturel and G. Brillant: "Diffusion of oxygen in uranium dioxide: a first-principles investigation", *Physical Review B*, 81 (2010) pp. 014110.
[42] S.D. Senanayake and H. Idriss: "Water reactions over stoichiometric and reduced UO_2(1 1 1) single crystal surfaces", *Surface Science*, 563 (2004) pp. 135-144.
[43] R.E. Woodley, R.E. Einziger and H.C. Buchanan: "Measurement of the oxidation of spent fuel between 140°C and 225°C by thermogravimetric analysis", *Westinghouse Hanford Company*, WHC-EP-0107 (1988).
[44] R.J. McEachern: "A review of kinetic data on the rate of U_3O_7 formation on UO_2", *Journal of Nuclear Materials*, 245 (1997) pp. 238-247.
[45] R.J. McEachern and P. Taylor: "A review of the oxidation of uranium dioxide at temperatures below 400°C", *Journal of Nuclear Materials*, 254 (1998) pp. 87-121.
[46] L.E. Thomas and R.E. Einziger: "Grain Boundary Oxidation of Pressurized-Water Reactor Spent Fuel in Air", *Materials Characterization*, 28 (1992) pp. 149-156.
[47] "Deep Repository Performance Assessment Project", *Swedish Nuclear Power Inspectorate* SKI Report 96:36 (1996).
[48] A. Fick: "Über Diffusion", *Annalen der Physik*, 170 (1855) pp. 59-86.
[49] J. Cranck: "The mathematics of diffusion", 2nd ed., Oxford University Press, Oxford, UK (1975).
[50] M. Kizilyalli, J. Corish and R. Metselaar: "Definitions of terms for diffusion in the solid state (IUPAC recommendations 1999)", *Pure and Applied Chemistry*, 71 (1999) pp. 1308-1325.
[51] L.S. Darken: "Diffusion, Mobility and Their Interrelation. Through Free Energy in Binary Metallic Systems", *AIME Transactions*, 175 (1948) pp. 184-195.
[52] J. Belle: "Oxygen and Uranium Diffusion in Uranium Dioxide", *Journal of Nuclear Materials*, 30 (1969) pp. 3-15.
[53] W. Breitung: "Oxygen self and chemical diffusion coefficients in $UO_{2\pm x}$", *Journal of Nuclear Materials*, 74 (1978) pp. 10-18.
[54] J.F. Marin and P. Contamin: "Uranium and Oxygen Self-Diffusion in UO_2", *Journal of Nuclear Materials*, 30 (1969) pp. 16-25.
[55] A.B. Auskern and J. Belle: "Oxygen ion self-diffusion in uranium dioxide", *Journal of Nuclear Materials*, 3 (1961) pp. 267-276.

[56] W. Dornelas and P. Lacombe: "Diffusion sous champ electrique de l'oxygene aux temperatures de 900° à 1000° C dans l'oxyde d'uranium UO_2", *Journal of Nuclear Materials*, 21 (1967) pp. 100-104.

[57] M. Fayek, L.M. Anovitz, D.R. Cole and D.A. Bostick: "O and H diffusion in uraninite: implications for fluid-uraninite interactions, nuclear waste disposal, and nuclear forensics", *Geochimica et Cosmochimica Acta*, 75 (2011) pp. 3677-3686.

[58] M. Fayek and T.K. Kyser: "Low temperature oxygen isotopic fractionation in the uraninite-UO_3-CO_2-H_2O system", *Geochimica et Cosmochimica Acta*, 64 (2000) pp. 2185-2197.

[59] K.C. Kim and D.R. Olander: "Oxygen Diffusion in UO_{2-x}", *Journal of Nuclear Materials*, 102 (1981) pp. 192-199.

[60] K.W. Lay: "Oxygen Chemical Diffusion Coefficient of Uranium Dioxide", *Journal of the American Ceramic Society*, 53 (1970) pp. 369-373.

[61] P. Contamin, J.J. Bacmann and J.F. Marin: "Autodiffusion de l'oxygene dans le dioxyde d'uranium surstoechiometrique", *Journal of Nuclear Materials*, 42 (1972) pp. 54-64.

[62] D.E.Y. Walker: "The oxidation of uranium dioxides", *Journal of Applied Chemistry*, 15 (1965) pp. 128-135.

[63] L.G. Harrison: "Influence of dislocations on diffusion kinetics in solids with particular reference to the alkali halides", *Transactions of the Faraday Society*, 57 (1960) pp. 1191-1199.

[64] R.E. Mistler and R.L. Coble: "Grain-boundary diffusion and boundary widths in metals and ceramics", *Journal of Applied Physics*, 45 (1974) pp. 1507-1509.

[65] J.C. Fisher: "Calculation of Diffusion Penetration Curves for Surface and Grain Boundary Diffusion", *Journal of Applied Physics*, 22 (1951) pp. 74-77.

[66] R.T.P. Whipple: "Concentration contours in grain boundary diffusion", *Philosophical Magazine Series 7*, 45 (1954) pp. 1225 -1236.

[67] H.S. Levine and C.J. MacCallum: "Grain boundary and lattice diffusion in polycrystalline bodies", *Journal of Applied Physics*, 31 (1960) pp. 595-599.

[68] I. Kaur, Y.M. Mishin and W. Gust: "Fundamentals of Grain and Interphase Boundary Diffusion", 3rd ed., Wiley and Sons, Chichester, UK (1995).

[69] J.D. Eshelby, C.W.A. Newey, P.L. Pratt and A.B. Lidiard: "Charged dislocations and the strength of ionic crystals", *Philosophical Magazine*, 3 (1958) pp. 75-89.

[70] T. Kubo, S. Ishimoto and T. Koyama: "Effects of Gadolinium Doping on Electrical Properties of UO_2 Grain Boundaries", *Journal of Nuclear Science and Technology*, 30 (1993) pp. 664-672.

[71] R.E. Einziger and R.E. Woodley: "Low temperature spent fuel oxidation under tuff repository conditions ", *Westinghouse Hanford Company*, HEDL-SA-3271FP (1985).

[72] R.E. Einziger and R.E. Woodley: "Predicting spent fuel oxidationstates in a tuff repository", *Westinghouse Hanford Company*, HEDL-SA-3627 (1987).

[73] D.R. Cole and S. Chakraborty: "Rates and mechanisms of isotopic exchange", *Reviews in Mineralogy and Geochemistry*, 43 (2001) pp. 83-123.

[74] A.C.S. Sabioni, W.B. Ferraz and F. Millot: "Effect of grain-boundaries on uranium and oxygen diffusion in polycrystalline UO_2", *Journal of Nuclear Materials*, 278 (2000) pp. 364-369.

[75] I. Grenthe, J. Fuger, R.J.M. Konings, R.J. Lemire, A.B. Muller *et al.*: "Chemical thermodynamics of uranium", Vol. North-Holland Elsevier Science Publishers B.V., Amsterdam (2004).
[76] V. Neck and J.I. Kim: "Solubility and hydrolysis of tetravalent actinides", *Radiochimica Acta*, 89 (2001) pp. 1-16.
[77] B. Pastina and J.A. LaVerne: "Effect of Molecular Hydrogen on Hydrogen Peroxide in Water Radiolysis", *Journal of Physical Chemistry A*, 105 (2001) pp. 9316-9322.
[78] D.W. Shoesmith: "Fuel corrosion processes under waste disposal conditions", *Journal of Nuclear Materials*, 282 (2000) pp. 1-31.
[79] P. Fors: "The effect of dissolved hydrogen on spent nuclear fuel corrosion", doctoral dissertation, Chalmers University of Technology, Gotebörg, Sweden (2009).
[80] K.-U. Ulrich, E.S. Ilton, H. Veeramani, J.O. Sharp, R. Bernier-Latmani *et al.*: "Comparative dissolution kinetics of biogenic and chemogenic uraninite under oxidizing conditions in the presence of carbonate", *Geochimica et Cosmochimica Acta*, 73 (2009) pp. 6065-6083.
[81] I. Grenthe, D. Ferri, F. Salvatore and G. Riccio: "Studies on metal carbonate equilibria. Part 10: a solubility study of the complex Formation in the uranium(vi)-water-carbon dioxide(g) system at 25°C", *Dalton Transactions*, 11 (1984) pp. 2439-2443.
[82] J. de Pablo, I. Casas, J. Giménez, M. Molera, M. Rovira *et al.*: "The oxidative dissolution mechanism of uranium dioxide. I. The effect of temperature in hydrogen carbonate medium", *Geochimica et Cosmochimica Acta*, 63 (1999) pp. 3097-3103.
[83] A. Ikeda, C. Hennig, S. Tsushima, K. Takao, Y. Ikeda *et al.*: "Comparative Study of Uranyl(VI) and -(V) Carbonato Complexes in an Aqueous Solution", *Inorganic Chemistry*, 46 (2007) pp. 4212-4219.
[84] B.G. Santos, J.J. Noël and D.W. Shoesmith: "The influence of silicate on the development of acidity in corrosion product deposits on SIMFUEL (UO_2)", *Corrosion Science*, 48 (2006) pp. 3852-3868.
[85] B.G. Santos, J.J. Noël and D.W. Shoesmith: "The influence of calcium ions on the development of acidity in corrosion product deposits on SIMFUEL, UO_2", *Journal of Nuclear Materials*, 350 (2006) pp. 320-331.
[86] I. Puigdomenech, J.-P. Ambrosi, L. Eisenlohr, J.-E. Lartigue, S.A. Banwart *et al.*: "O_2 depletion in granitic media", *Swedish Nuclear Fuel and Waste Management Co.*, SKB Technical Report TR-01-05 (2001).
[87] K. Spahiu, L. Werme and U.-B. Eklund: "The influence of near field hydrogen on actinide solubilities and spent fuel leaching", *Radiochimica Acta*, 88 (2000) pp. 507-511.
[88] P. Carbol, P. Fors, T. Gouder and K. Spahiu: "Hydrogen suppresses UO_2 corrosion", *Geochimica et Cosmochimica Acta*, 73 (2009) pp. 4366-4375.
[89] A. Loida, B. Kienzler and H. Geckeis: "Mobilization/Retention of Radionuclides during Corrosion of High Burnup Spent Fuel and Backfill Materials in Salt Brines", *Materials Research Society Symposium - Proceedings*, 2003,
[90] K. Ollila and V.M. Oversby: "Testing of uranium dioxide enriched with ^{233}U under reducing conditions", *Materials Research Society Symposium Proceedings*, 932 (2006) pp. 441.

[91] D. Magallon, H. Schins, R. Zeyen and R. Hohmann: "The FARO experimental programme: quick look on UO_2 melting and BLOKKER I results", *European Commission, Joint Research Centre*, Technical Report TN 1.89.14. (1989).
[92] V.V. Rondinella and H. Matzke: "Leaching of SIMFUEL in simulated granitic water: comparison to results in demineralized water", *Journal of Nuclear Materials*, 238 (1996) pp. 44-57.
[93] P.G. Lucuta, R.A. Verrall, H. Matzke and B.J. Palmer: "Microstructural features of SIMFUEL - Simulated high-burnup UO_2-based nuclear fuel", *Journal of Nuclear Materials*, 178 (1991) pp. 48-60.
[94] D. Manara: "Melting transition measurements in uranium dioxide", doctoral dissertation, University of Warwick, Warwick, UK (2004).
[95] A. Leenaers, L. Sannen, S. Van den Berghe and M. Verwerft: "Oxidation of spent UO_2 fuel stored in moist environment", *Journal of Nuclear Materials*, 317 (2003) pp. 226-233.
[96] P. Carbol, P. Fors, S. Van Winckel and K. Spahiu: "Corrosion of irradiated MOX fuel in presence of dissolved H2", *Journal of Nuclear Materials*, 392 (2009) pp. 45-54.
[97] I. Horcas, R. Fernandez, J.M. Gomez-Rodriguez, J. Colchero, J. Gomez-Herrero *et al.*: "WSXM: A software for scanning probe microscopy and a tool for nanotechnology", *Review of Scientific Instruments*, 78 (2007) pp. 013705.
[98] D. Briggs and M.P. Seah: "Practical Surface Analysis by Auger and X-ray Photoelectron Spectroscopy", Vol. John Wiley & Sons, Chichester, U.K. (1983).
[99] M. Schindler, F.C. Hawthorne, M.S. Freund and P.C. Burns: "XPS spectra of uranyl minerals and synthetic uranyl compounds. II: The O 1s spectrum", *Geochimica et Cosmochimica Acta*, 73 (2009) pp. 2488-2509.
[100] Y. Ranebo: "Physical characterization of actinides particles. A study on novel techniques for radiological and nuclear safeguard investigations.", Lund, Sweden, Lund, Sweden (2009).
[101] L.R. Riciputi, B.A. Paterson and R.L. Ripperdan: "Measurement of light stable isotope ratios by SIMS: Matrix effects for oxygen, carbon, and sulfur isotopes in minerals", *International Journal of Mass Spectrometry*, 178 (1998) pp. 81-112.
[102] I.C.W. Fitzsimons, B. Harte and R.M. Clark: "SIMS stable isotope measurement: counting statistics and analytical precision", *Mineralogical Magazine*, 64 (2000) pp. 59-83.
[103] K.L. Nagy and B.J. Giletti: "Grain boundary diffusion of oxygen in a macroperthitic feldspar", *Geochimica et Cosmochimica Acta*, 50 (1986) pp. 1151-1158.
[104] P. Fielitz, G. Borchardt, M. Schmücker and H. Schneider: "Aluminium grain boundary diffusion in polycrystalline mullite ceramics", *Physics and Chemistry of Minerals*, 34 (2007) pp. 431-436.
[105] L. Desgranges and B. Pasquet: "Measurement of xenon in uranium dioxide (UO_2) with SIMS", *Nuclear Instruments and Methods in Physics Research Section B: Beam Interactions with Materials and Atoms*, 215 (2004) pp. 545-551.
[106] "IUPAC. Compendium of Chemical Terminology (the 'Gold Book')", 2nd ed., Blackwell Scientific Publications, Oxford, UK (1997).

[107] A. Benninghoven, F.G. Rüdenauer and H.W. Werner: "Secondary ion mass spectrometry", Wiley-Interscience, New York, USA (1987).
[108] P. Fielitz, G. Borchardt, M. Schmuecker, H. Schneider, M. Wiedenbeck *et al.*: "Secondary Ion Mass Spectroscopy Study of Oxygen-18 Tracer Diffusion in 2/1-Mullite Single Crystals", *Journal of the American Ceramic Society*, 84 (2001) pp. 2845-2848.
[109] D. Gorman-Lewis, L. Mazeina, J.B. Fein, J.E.S. Szymanowski, P.C. Burns *et al.*: "Thermodynamic properties of soddyite from solubility and calorimetry measurements", *The Journal of Chemical Thermodynamics*, 39 (2007) pp. 568-575.
[110] S. Portier, S. Bremier, R. Hasnaoui, O. Bildstein and C.T. Walker: "Investigation of the relative sensitivity factor for the quantification of ion microprobe results for Nd isotopes in simulated nuclear fuel", *Microchimica Acta*, 161 (2008) pp. 479-483.
[111] C. Ferry, C. Poinssot, C. Cappelaere, L. Desgranges, C. Jegou *et al.*: "Specific outcomes of the research on the spent fuel long-term evolution in interim dry storage and deep geological disposal", *Journal of Nuclear Materials*, 352 (2006) pp. 246-253.
[112] D.J. Barber, F.C. Frank, M. Moss, J.W. Steeds and I.S.T. Tsong: "Prediction of ion-bombarded surface topographies using Frank's kinematic theory of crystal dissolution", *Journal of Materials Science*, 8 (1973) pp. 1030-1040.
[113] H. Matzke and A. Turos: "Mechanisms and kinetics of leaching of UO_2 in water", *Solid State Ionics*, 49 (1991) pp. 189-194.
[114] G.L. Reynolds and B. Burton: "Grain-boundary diffusion in uranium dioxide: the correlation between sintering and creep and a reinterpretation of creep mechanism", *Journal of Nuclear Materials*, 82 (1979) pp. 22-25.
[115] M. Tomozawa: "Water diffusion in silica glass and wet oxidation of Si: an interpretation for the high speed of wet oxidation", *Journal of The Electrochemical Society*, 158 (2011) pp. G115-G118.
[116] N.J. Dudney, J.B. Bates and J.C. Wang: "Diffusion of water in lithium β-alumina", *Physical Review B*, 24 (1981) pp. 6831-6842.
[117] S.D. Senanayake, R. Rousseau, D. Colegrave and H. Idriss: "The reaction of water on polycrystalline UO2: Pathways to surface and bulk oxidation", *Journal of Nuclear Materials*, 342 (2005) pp. 179-187.
[118] M.N. Hedhili, B.V. Yakshinskiy and T.E. Madey: "Interaction of water vapor with UO_2(001)", *Surface Science*, 445 (2000) pp. 512-525.

List of Abbreviations

AFM	Atomic Force Microscopy
a.u.	arbitrary units
BWR	Boiling Water Reactor
cps	counts per second
D_L	diffusion coefficient in the lattice
D_B	grain-boundary diffusion coefficient
D_{eff}	effective diffusion coefficient
D_i *	Self-diffusion of the species *i*
FBR	Fast Breeder Reactor
GCR	Gas Cooled Reactor
GWd/tHM	Giga Watt days per ton of Heavy Metal
HBU	High Burn-up
HWR	Heavy Water Reactor
ICP-MS	Inductively Coupled Plasma Mass Spectrometry
IRF	Instant Release Fraction
LWR	Light Water Reactor
LWGR	Light Water Graphite Moderated Reactor
M	Concentration in mol/L
MOX	Mixed Oxide (UO_2 + PuO_2)
PE	Polyethylene
PEEK	Polyether ether ketone
PWR	Pressurised Water Reactor
PHWR	Pressurised Heavy Water Reactor
RT	Room temperature (25 ± 3 °C)
SEM-EDX	Scanning Electron Microscope coupled with Energy Dispersive X-Ray spectroscopy
SIMS	Secondary Ion Mass spectrometry
SKB	Swedish Nuclear Fuel and Waste Management Company
TG	Thermogravimetry
XRD	X-ray Diffraction
XPS	X-ray Photoelectron Spectroscopy

Eidesstattliche Versicherung gemäß § 8 der Promotionsordnung der Naturwissenschaftlich-Mathematischen Gesamtfakultät der Universität Heidelberg

1. Bei der eingereichten Dissertation zu dem Thema

_____

_____

_____

handelt es sich um meine eigenständig erbrachte Leistung.

2. Ich habe nur die angegebenen Quellen und Hilfsmittel benutzt und mich keiner unzulässigen Hilfe Dritter bedient. Insbesondere habe ich wörtlich oder sinngemäß aus anderen Werken übernommene Inhalte als solche kenntlich gemacht.

3. Die Arbeit oder Teile davon habe ich wie folgt/bislang nicht[1)] an einer Hochschule des In- oder Auslands als Bestandteil einer Prüfungs- oder Qualifikationsleistung vorgelegt.

Titel der Arbeit:_____

_____

Hochschule und Jahr:_____

Art der Prüfungs- oder Qualifikationsleistung:_____

4. Die Richtigkeit der vorstehenden Erklärungen bestätige ich.

5. Die Bedeutung der eidesstattlichen Versicherung und die strafrechtlichen Folgen einer unrichtigen oder unvollständigen eidesstattlichen Versicherung sind mir bekannt.

Ich versichere an Eides statt, dass ich nach bestem Wissen die reine Wahrheit erklärt und nichts verschwiegen habe.

_____ _____

Ort und Datum Unterschrift

[1)] Nicht Zutreffendes streichen. Bei Bejahung sind anzugeben: der Titel der andernorts vorgelegten Arbeit, die Hochschule, das Jahr der Vorlage und die Art der Prüfungs- oder Qualifikationsleistung.